

Studies of manganese based oxides as alternative electrode materials for lithium based energy storage devices

Nagasubramanian, Arun

2016

Nagasubramanian, A. (2016). Studies of manganese based oxides as alternative electrode materials for lithium based energy storage devices. Doctoral thesis, Nanyang Technological University, Singapore.

<https://hdl.handle.net/10356/67015>

<https://doi.org/10.32657/10356/67015>



NANYANG
TECHNOLOGICAL
UNIVERSITY

**STUDIES OF MANGANESE BASED OXIDES AS
ALTERNATIVE ELECTRODE MATERIALS FOR
LITHIUM BASED ENERGY STORAGE DEVICES**

ARUN NAGASUBRAMANIAN

SCHOOL OF MATERIAL SCIENCE AND ENGINEERING

2016

**STUDIES OF MANGANESE BASED OXIDES AS
ALTERNATIVE ELECTRODE MATERIALS FOR
LITHIUM BASED ENERGY STORAGE DEVICES**

ARUN NAGASUBRAMANIAN

School of Materials Science and Engineering

A thesis submitted to the Nanyang Technological University in
partial fulfilment of the requirement for the degree of Doctor of
Philosophy

2016

Acknowledgements

This work would not have been possible without the support and guidance of a number of people and organisations and it is my bounden duty to thank them.

First and foremost I wish to thank my supervisor Assoc. Prof. Madhavi Srinivasan for providing me with an opportunity to pursue a PhD degree at the School of Material Science and Engineering. If not for her constant understanding, guidance, support and encouragement through tough times, this work would not have seen light of the day.

I wish to convey my deepest sense of gratitude to the School of Material Science and Engineering and Nanyang Technological University for the the opportunity to pursue my PhD degree with financial support. The past four and a half years here have been a truly rewarding experience.

I wish to thank TUM CREATE LTD. for providing me an opportunity to work in their lab and supporting me by offering the position of Research Associate during the final phase of my PhD submission. The experiences right from setting up a lab to maintaining equipment and looking after regulatory adherences and learning the techniques of battery research have provided me with a wealth of invaluable knowledge.

I would like to acknowledge the steady support of my co-author and senior researcher at ERIAN Dr. Vanchiappan Aravindan who was instrumental in helping me with the demonstration of full cell devices and getting the results of this work published in high impact factor journals. His guidance and support is deeply appreciated.

Next I wish to thank Prof. Harry Hoster and Prof. Denis Yu who shared their wealth of knowledge and experience in electrochemistry and lithium ion batteries and also helped guide us in setting up of the TUM CREATE Chemical Lab.

I wish to sincerely thank the alumnus of the energy storage group at MSE Dr. Teh Pei Fen and Dr. Cheah Yan Ling who were one of my first mentors who helped me grasp the basics of battery making and equipment operation in wet chemical lab.

Without the support of my colleagues at TUM CREATE, it would not have been possible to keep the lab running smoothly. I take this opportunity to thank Steffen Schlueter, Steffen Hartung, Nicolas Bucher, Jochen Friedl, Jan Geder and Dr. Iulius for their assistance.

Special thanks are due to my friends Dr. Ali Rinaldi, Ms. Oliviya Wijaya, Ms. Teng Yin Ting, Ms. Hanyi Chen and Ms. Heryani Bte Ahmad for the support throughout these 4 years. The thought provoking discussions on wide ranging topics from electrochemistry to religion & USA coupled with sarcasm riddled jabs provided a fantastic atmosphere to perform research.

I also wish to thank my colleagues at the energy storage group at MSE Grace, Chui Ling, Sutanto, Vivek, Rohit, Aravind, Shubha for the nice times in the lab.

Last but not least, I am deeply indebted to my wife, parents and daughter. No amount of words cannot do justice to the sacrifices they have made to enable me realize this dream of mine and I am eternally grateful for that.

Table of contents

Acknowledgements	i
Table of contents	v
Table captions	ix
Figure captions	xi
Abbreviations	xv
Abstract	i
Chapter 1 Introduction	1
1.1 Problem statement	3
1.2 Motivation	4
1.3 Research scope and objectives	5
1.4 Dissertation overview	6
1.5 Findings and outcomes	7
References	7
Chapter 2 Literature review	9
2.1 History and early developments	11
2.2 Operating principles and construction of LIBs & LICs	12
2.3 Spinel LiMn_2O_4 as lithium insertion host	16
2.4 Spinel $\text{Li}_4\text{Mn}_5\text{O}_{12}$ as lithium insertion host	27
2.5 Questions to answers based on literature	30
2.6 PhD in the context of literature	30
References	31
Chapter 3 Experimental methodology	39
3.1 Rationale for selection of methods/materials	41
3.2 Synthesis of active materials	41
3.2.1 Solid state synthesis	42
3.2.2 Co-precipitation synthesis	43

3.2.3	Electrospinning	46
3.3	Characterization	49
3.3.1	Powder diffraction with X-rays	49
3.3.2	Scanning electron microscopy	51
3.3.3	Transmission electron microscopy	52
3.3.4	Thermal analysis techniques	54
3.3.5	Fourier Transform Infrared spectroscopy	55
3.3.6	Electrode preparation and cell assembly	56
3.3.7	Cyclic voltammetry	60
3.3.8	Galvanostatic cycling	61
3.3.9	Electrochemical impedance spectroscopy	61
3.4	Overview of methodologies	62
	References	63
Chapter 4	Effect of elemental substitutions on performance	65
4.1	Introduction	67
4.2	Experimental methods – nickel substitution in LiMn_2O_4	68
4.2.1	Powder X-ray diffraction	68
4.2.2	Scanning electron microscopy	70
4.2.3	Fourier Transform Infrared Spectroscopy	71
4.2.4	Thermal analysis	73
4.2.5	Cyclic Voltammetry	74
4.2.6	Galvanostatic cycling	76
4.2.7	Cyclic voltammetry at different rates	86
4.2.8	Electrochemical Impedance Spectroscopy	89
4.2.9	Ex-situ X-ray diffraction	92
4.3	Experimental methods – titanium substitution in $\text{Li}_4\text{Mn}_5\text{O}_{12}$	95
4.3.1	Powder X-ray diffraction	95

4.3.2	Cyclic voltammetry.....	97
4.3.3	Galvanostatic cycling.....	98
4.3.4	Cyclic voltammetry at different rates.....	99
4.3.5	Ex-situ X-ray diffraction.....	100
4.4	Observations.....	101
4.4.1	Effect of nickel substitution in LiMn_2O_4	101
4.4.2	Effect of titanium substitution in $\text{Li}_4\text{Mn}_5\text{O}_{12}$	102
4.5	Conclusions.....	103
	References.....	104
Chapter 5	Influence of morphology and nano-structuring.....	107
5.1	Introduction.....	109
5.2	Experimental methods – LNM via carbonate co-precipitation.....	110
5.2.1	Powder X-ray diffraction.....	110
5.2.2	Scanning electron microscopy.....	111
5.2.3	Fourier Transform Infrared spectroscopy.....	113
5.2.4	Thermal Analysis.....	114
5.2.5	Cyclic voltammetry and galvanostatic.....	114
5.2.6	Cyclic voltammetry at different rates.....	117
5.3	Experimental methods – LNM via electrospinning and solid state.....	118
5.3.1	Powder X-ray diffraction.....	118
5.3.2	Electron microscopy.....	119
5.3.3	Thermal analysis.....	120
5.3.4	Fourier Transform Infrared spectroscopy.....	121
5.3.5	Cyclic voltammetry and galvanostatic cycling.....	121
5.3.6	Cyclic voltammetry at different rates.....	127
5.3.7	Electrochemical Impedance Spectroscopy	127
5.4	Effect of spherical morphology on performance.....	128

5.5	Effect of nano-structuring on performance	129
5.6	Understanding the capacity fading mechanism	129
5.7	Conclusions	131
	References	132
Chapter 6	Demonstration of full cell devices	133
6.1	Insertion electrode in hybrid supercapacitors	135
6.2	Insertion electrode in lithium ion battery	137
6.3	Conclusions	140
	References	141
Chapter 7	Discussions and future work	143
7.1	Introduction	145
7.2	Evaluation of performance target	147
7.3	Issues to be addressed for commercialization	148
7.4	Future work	149
7.5	Scientific contributions	150
7.6	Technological contributions	151
	References	151

Table captions

Table 3.1	Comparison of different synthesis techniques	49
Table 4.1	Refinement results for LNM and LMO	69
Table 4.2	Initial capacities and retention for spinel LMO & LNM	78
Table 4.3	Amount of lithium cycled and irreversible loss	83
Table 4.4	Lithium diffusion coefficients in spinel LNM	88
Table 4.5	Refinement results for $\text{Li}_4\text{Ti}_x\text{Mn}_{5-x}\text{O}_{12}$ ($0 \leq x \leq 1$)	97
Table 5.1	Initial capacities and retention for spherical LNM	116
Table 5.2	Comparison of lithium diffusion co-efficients	117

Figure captions

Figure 2.1	Schematic of a lithium ion battery.....	12
Figure 2.2	Schematic of a parallel plate capacitor.....	15
Figure 2.3	Crystal structure of LiMn_2O_4	17
Figure 2.4	Schematic of effect of Jahn-Teller distortion.....	22
Figure 2.5	Crystal structure of $\text{Li}_4\text{Mn}_5\text{O}_{12}$ ($\text{Li}_{1.33}\text{Mn}_{1.67}\text{O}_4$).....	28
Figure 3.1	Schematic of electrospinning setup.....	47
Figure 3.2	Process flow for synthesis of 1D nanofibrous oxides	48
Figure 4.1	XRD patterns of (a) spinel LMO (b) spinel LNM.....	68
Figure 4.2	Variation of lattice parameter with calcination condition.....	68
Figure 4.3	SEI of spinel LNM and LMO.....	70
Figure 4.4	FTIR spectra of (a) LNM (b) LMO.....	71
Figure 4.5	TGA of (a) LNM (b) LMO.....	73
Figure 4.6	CV of spinel LMO and LNM.....	74
Figure 4.7	CV of spinels (a) LNM (b) LMO.....	75
Figure 4.8	Galvanostatic performance of spinel LMO and LNM.....	77
Figure 4.9	Efficiency of spinel LNM samples cycled in 5V region.....	77
Figure 4.10	First charge-discharge curves of spinels.....	82
Figure 4.11	Rate capability of spinel (a) LNM (b) LMO.....	84
Figure 4.12	Rate capability of spinel (a) LNM (b) LMO.....	85
Figure 4.13	Peak current density vs scan rate for LMO and LNM.....	87
Figure 4.14	Peak current density vs. scan rate for spinel LNM.....	88
Figure 4.15	Equivalent circuit employed for fitting EIS data.....	89
Figure 4.16	EIS analysis of spinel LNM and LMO.....	90
Figure 4.17	EIS analysis of spinel LNM.....	91
Figure 4.18	Ex-situ XRD before and after cycling, LMO & LNM.....	92
Figure 4.19	Ex-situ XRD of electrodes after cycling.....	93

Figure 4.20	Ex-situ XRD of spinel LMO and LNM after cycling.....	94
Figure 4.21	XRD patterns of $\text{Li}_4\text{Ti}_x\text{Mn}_{5-x}\text{O}_{12}$ ($0 \leq x \leq 1$).....	96
Figure 4.22	CV curves of $\text{Li}_4\text{Ti}_x\text{Mn}_{5-x}\text{O}_{12}$ ($0 \leq x \leq 1$).....	97
Figure 4.23	Electrochemical performance of $\text{Li}_4\text{Ti}_x\text{Mn}_{5-x}\text{O}_{12}$	98
Figure 4.24	Peak current density vs scan rate, $\text{Li}_4\text{Ti}_x\text{Mn}_{5-x}\text{O}_{12}$	99
Figure 4.25	Ex-situ XRD after cycling $\text{Li}_4\text{Ti}_x\text{Mn}_{5-x}\text{O}_{12}$	100
Figure 5.1	XRD patterns (a) precursors (b) LNM spheres.....	110
Figure 5.2	SEI of spherical LNM.....	112
Figure 5.3	FTIR spectra of spherical LNM.....	113
Figure 5.4	TGA curves of spherical LNM.....	114
Figure 5.5	Electrochemical performance of spherical LNM.....	115
Figure 5.6	Electrochemical performance of spherical LNM.....	115
Figure 5.7	Powder XRD patterns of LNM-ES and LNM-SS.....	118
Figure 5.8	Electron micrographs of LNM-ES and LNM-SS.....	119
Figure 5.9	TGA curves of LNM-ES.....	120
Figure 5.10	FTIR spectra of LNM-ES and LNM-SS samples.....	121
Figure 5.11	Electrochemical performance of LNM-SS in 3.5 -5V.....	122
Figure 5.12	Electrochemical performance of LNM-SS in 2.3 -3.3V.....	123
Figure 5.13	Electrochemical performance of LNM-ES in 3.5 -5V.....	124
Figure 5.14	Electrochemical performance of LNM-ES in 2.3 -3.3V.....	125
Figure 5.15	Peak current density vs scan rate, LNM-ES and LNM-SS.....	127
Figure 5.16	EIS analysis for LNM-ES and LNM-SS.....	128
Figure 5.17	Crystal structures of different space groups of LNM.....	130
Figure 6.1	Half-cell performances of LNM-ES and AC.....	135
Figure 6.2	Performance of hybrid supercapacitor.....	136
Figure 6.3	Half-cell performance of LNM-ES, TiO_2	138
Figure 6.4	Performance of rechargeable battery.....	139

Abbreviations

CV	Cyclic Voltammetry
DSC	Differential Scanning Calorimetry
EDX	Energy Dispersive analysis of X-rays
EIS	Electrochemical Impedance Spectroscopy
FTIR	Fourier Transform Infrared spectroscopy
LIB	Lithium Ion Battery
LMO	Spinel lithium manganese oxide
LMN	Spinel Lithium Nickel Manganese oxide
SEI	Secondary Electron Image
SEM	Scanning Electron Microscopy
TEI	Transmission Electron Image
TEM	Transmission Electron Microscopy
TGA	Thermo Gravimetric Analysis
XRD	X-ray Diffraction

Abstract

Lithium ion based energy storage devices have captured a significant share of the market for energy storage devices owing to their high energy and power density. However the cost of raw materials and their availability warrants a search for alternative materials with improved energy densities and rate capabilities. Manganese based oxide materials are attractive as alternative choices for electrode materials. However, they encounter a host of issues which result in poor performance in systems based on the Li^+ ion shuttle. One of the issues is structural degradation. It is well known that spinel LiMn_2O_4 undergoes structural degradation when lithium is inserted into the octahedral voids of the structure owing to the change of average valence of manganese from +3.5 to +3. This leads to a Jahn-Teller distortion induced structural relaxation that leads to the formation of a new tetragonal phase which is responsible for poor capacity retention. However if one can manage to keep the average manganese valence to above +3.5 during lithium insertion, it would be possible to prevent JT distortion and associated structural changes thus making it possible to access the voltage offered by the $\text{Mn}^{3+}/\text{Mn}^{4+}$ redox couple.

This thesis sheds new light on the existing understanding about the effect of substitutions on performance of two well-known spinel compounds LiMn_2O_4 (substitution with nickel) and $\text{Li}_4\text{Mn}_5\text{O}_{12}$ (substitution with titanium). Both substitutions were found to prevent phase transformation during cycling resulting in better capacity retention. Different synthesis methods are employed to prepare samples with different morphologies and the effect of morphology on performance is also investigated. It was found that the performance of the spinel $\text{LiNi}_{0.5}\text{Mn}_{1.5}\text{O}_4$ was affected by the space group of the crystal structure as well as morphology in the voltage range of 2.3 – 3.3V. Nano-structuring was found to play a significant role in improving the performance of spinel $\text{LiNi}_{0.5}\text{Mn}_{1.5}\text{O}_4$. The findings reveal that nickel substitution in $\text{LiNi}_{0.5}\text{Mn}_{1.5}\text{O}_4$ was a more attractive option to pursue. Finally full cell devices were assembled using the best performing material as working electrode to demonstrate the feasibility of manganese based oxide materials as attractive alternative electrode materials for rechargeable energy storage devices based on the lithium ion.

Chapter 1

Introduction

This chapter will present the problem statement, objectives and scope of this work together with the findings or outcomes. It provides the motivation and background for the proposed work. An overview of the dissertation consisting of the different chapters and their contents is also presented.

1.1 Problem statement

Energy demand in the world is rising at a burgeoning pace. Statistics from the International Energy Agency state that the total energy consumption of the world in 2011 was about 8910 Mtoe ($1 \text{ Mtoe} = 1.2444 \times 10^{14} \text{ kWh}$, Mtoe stands for Million tons of oil equivalent or the energy obtained by burning 1 million tons of crude oil)[1]. About 80 % of the energy generated in 2011 was from fossil fuel based sources including coal, natural gas, petroleum and oil shale. The remaining 20 % is generated from other sources including renewable sources such as wind, solar, bio fuels, hydro and nuclear power. However fossil fuel based sources are limited in nature and plagued by non-uniform availability, price rise and local supply disturbances which have a profound effect on world economies.

Amongst non-fossil fuel based sources, nuclear power is an attractive alternative in terms of the scale of output. But it is fraught with risks of catastrophe and the possibility of misuse. Renewable sources such as wind, solar and hydroelectric power provide an alternative albeit with an inherent disadvantage. They are intermittent (especially wind and solar) and require some form of storage in order to make them an uninterrupted source of supply which can be synchronized with existing grid based electrical energy distribution systems. It is increasingly being realized that this problem can be tackled using battery based energy storage systems[2–5]. Batteries which store energy in the chemical form and convert it into electrical form and vice versa offer a host of attractive features such as size, scalability and wide range of energy and power capabilities. A wide range of chemistries such as zinc-manganese oxide, nickel metal hydride, nickel-cadmium, lead acid, vanadium redox flow, sodium – sulphur and lithium ion (LIBs) are available for applications that present varied requirements.

Amongst the different chemistries, LIBs are much sought after owing to their high volumetric energy and power densities which makes them attractive for applications that have space constraints. Currently, LIBs dominate the market for powering a variety of portable applications such as laptops, digital cameras, mobile phones, hand held drilling tools, electric and hybrid electric vehicles. However when it comes to grid scale energy storage applications, cost, toxicity and lifetime remain obstacles to their implementation.

Typically in LIBs, the cathode material consists of a combination of cobalt/nickel/manganese making it expensive and toxic. Recycling and disposal of cobalt containing materials is challenging and costly as well. Fortunately more benign cathode materials are available. For example the manganese based spinel oxide LiMn_2O_4 has been demonstrated to be a suitable alternative cathode with high power capability. Similarly olivine type LiFePO_4 is another cost effective choice. However both these low cost materials have other issues of their own. The spinel LiMn_2O_4 demonstrates poor cycling performance especially at elevated temperatures due to structural instability and manganese dissolution. The LiFePO_4 cathode in spite of having good structural stability, suffers from poor electronic conductivity making carbon coating a necessary step in its processing thus increasing its overall production cost. Finally none of the LIBs available currently demonstrate the long term cycling stability necessary for grid scale energy storage applications.

1.2 Motivation

Ever since the first LIB was commercialized by Sony Corp. in 1991, there have been concerted efforts to develop manganese based materials specifically the layered and orthorhombic LiMnO_2 , LiMn_2O_4 and $\text{Li}_4\text{Mn}_5\text{O}_{12}$ with the aim of commercializing low cost, environmentally friendly materials. However it was soon realized that the number of challenges posed (such as dissolution, structural instability and poor rate performance) by manganese based oxides were simply too huge and required more in-depth research. Also other material combinations which were far more attractive such as the olivine LiFePO_4 , layered NCM and NCA were investigated. This redirected efforts at optimizing such materials rather than focusing on tackling issues in manganese based systems. Recently again manganese based oxides have started gaining importance as the next generation cathode materials such as $x\text{Li}_2\text{MnO}_3 \cdot (1-x)(\text{LiNi}_y\text{Mn}_z\text{Co}_{1-y-z})\text{O}_2$ and $\text{LiNi}_{0.5}\text{Mn}_{1.5}\text{O}_4$.

It is thus the focus of this work to revisit the possibilities of using different manganese based oxide materials in an effort to contribute towards the development of cheaper and more environment friendly rechargeable energy storage systems that could be considered for grid scale applications. For a reliable grid scale energy storage system, the currently available system (sodium-sulphur) provides a lifetime of roughly 4500 cycles with an efficiency of 75%[4]. But this system requires to be continuously

heated and part of the energy stored goes towards maintaining this working temperature. It will hence be the aim of this work to demonstrate a full cell device with a performance similar to this commercial device which can avoid requirements such as continuous heating thus making it both safer and inexpensive to operate.

1.3 Research scope and objectives

The broad objective of this work is to address structural degradation that leads to poor performance in different spinel manganese oxides and explore the possibility of employing them as electrode materials in full cell devices. Specifically the objectives include the following.

➤ **Investigating the effect of elemental substitutions on electrochemical performance.**

In manganese based spinel oxides, it is known that the main redox process utilized for charge storage is $\text{Mn}^{3+} \leftrightarrow \text{Mn}^{4+}$. It is possible to insert Li^+ into both tetrahedral and octahedral void sites in a spinel structure while converting Mn^{4+} to Mn^{3+} . While systems are available that utilize reversible Li^+ insertion into tetrahedral sites (in a voltage range of 4V vs. Li/Li^+), lithium insertion into vacant octahedral sites (in a voltage range of 3V vs. Li/Li^+) has not been sought after primarily due to the problem of structural instability caused by Jahn-Teller distortion that sets in when the average manganese valence decreases below +3.5. It is possible to minimize Jahn-Teller related effects by choosing a compound that has a higher average Mn valence or by adjusting the valence using elemental substitutions. In this regard, the Ni^{2+} substituted compound ($\text{LiNi}_{0.5}\text{Mn}_{1.5}\text{O}_4$) and Ti substituted lithium excess spinel $\text{Li}_4\text{Mn}_5\text{O}_{12}$ are investigated in the potential range of 3V vs. Li/Li^+ . It is shown that both elemental substitutions are helpful in slowing down/preventing structural transformation.

➤ **Study of the effect of morphology and nano-structuring on performance.**

Morphology can have a profound effect on electrochemical performance and it has been demonstrated for a number of materials. To see if the performance in the 3V region is affected by morphology, different synthesis techniques are employed to synthesize spinel LiMn_2O_4 , $\text{Li}_4\text{Mn}_5\text{O}_{12}$ and $\text{LiNi}_{0.5}\text{Mn}_{1.5}\text{O}_4$ with varying morphologies and surface areas. It was observed that the nano-structuring and morphology has a

significant effect on the electrochemical behaviour of spinel LNM. Electropsun $\text{LiNi}_{0.5}\text{Mn}_{1.5}\text{O}_4$ was found to have the best electrochemical performance amongst all the different samples investigated.

➤ **Demonstration of full cell devices**

The technical feasibility of the optimized electropsun $\text{LiNi}_{0.5}\text{Mn}_{1.5}\text{O}_4$ is then validated by testing in full cell configurations for lithium ion batteries and hybrid capacitors. The benefit of nano-structuring is also demonstrated for a rechargeable lithium battery with anode, cathode and separator fabricated via single spinneret electrospinning technique. A hybrid lithium ion capacitor employing the electropsun $\text{LiNi}_{0.5}\text{Mn}_{1.5}\text{O}_4$ as a lithium insertion electrode is also demonstrated. Finally the possibility of a lithium ion full cell utilizing electropsun LNM for both anode and cathode is also explored.

➤ **Fundamental studies to understand improved performance and reasons for fading.**

In order to understand the observed differences in performance, fundamental studies using impedance, cyclic voltammetry and ex-situ XRD are carried out to understand structural changes and the diffusion properties of the various phases.

1.4 Dissertation overview

The dissertation has been organized into several chapters the contents of which are briefly summarized below.

Chapter 1 introduces the motivation for this work and provides the research scope and overview. The aim of the thesis would be to identify the potential for applying manganese based spinel oxides in configurations hitherto unexplored and determine their suitability for grid scale energy storage applications.

Chapter 2 presents in brief the basic principles and construction of lithium ion batteries and hybrid capacitors. It provides a detailed analysis of the spinel oxides under consideration summing up the issues faced so far and solutions that have been proposed to overcome them.

Chapter 3 discusses the detailed procedures for the different synthesis methods employed for preparing the two spinel compounds considered in this work. Structural and electrochemical characterization techniques employed are presented. Protocols

followed for preparing cells for testing are also discussed. Synthesis methods for electrode materials are also discussed in brief to justify their selection in this work

Chapter 4 presents the results of studies that analyse the effect of elemental substitutions on electrochemical performance for both the spinel compounds synthesized via a standard procedure. Fundamental studies involving diffusion coefficient estimation, impedance analysis and ex-situ X-ray diffraction studies are performed.

Chapter 5 analyses the effect of morphology and nano-structuring on performance of the spinel compound chosen for further studies from chapter 4 and identifies the best performing material.

Chapter 6 demonstrates the two full cell devices that were generated from this study and compares its performance with similar configurations reported in literature.

Chapter 7 provides the connection between the various studies carried out, the contributions of this thesis both scientific as well as technological. The achievement of the study is compared with the design target and suggestions for improvement followed by strategies for future work are presented.

1.5 Findings and outcomes

This work led to the following outcomes

1. Establishing a method to study the effect of calcination temperature on performance while fixing particle size.
2. Establishing the effect of space group and its effect on electrochemical performance for nickel substituted spinel lithium manganese oxide.
3. Demonstration of full cell devices by tapping into different voltage ranges of operation offered by the same spinel LNM.

References

- [1] OECD/IEA, Key World Energy STATISTICS, IEA Publ. (2013).
- [2] J.B. Goodenough, K.-S. Park, *J. Am. Chem. Soc.* **2013**, 135, 1167–1176.
- [3] K.C. Divya, J. Østergaard, *Electr. Power Syst. Res.* **2009**, 79, 511–520.

- [4] B. Dunn, H. Kamath, J. Tarascon, *Science*, **2011**, 334, 928.
- [5] Z. Yang, J. Zhang, M.C.W. Kintner-Meyer, X. Lu, D. Choi, J.P. Lemmon, et al., *Chem. Rev.* **2011**, 111, 3577–613.

Chapter 2

Literature Review

This chapter presents the historical development of lithium intercalation into materials, the working principle of lithium ion batteries and hybrid supercapacitors. The development of manganese based oxides as lithium insertion host, the attendant problems and solutions identified to tackle those problems are discussed in detail. Emphasis is also placed on synthesis techniques employed for electrode materials. Finally based on gaps in literature, new ideas that form the basis of this work are summarized.

2.1 History and early developments

The history of ion intercalation into materials can be traced back to the studies of a number of research groups around the early 1970s. Whittingham [1,2], Subba Rao [3], Schollhorn [4] had investigated ion intercalation into layered di-chalcogenides during the early 1970s demonstrating the possibility of inserting ions into these structures electrochemically. Similarly Besenhard and colleagues working at the Technical University of Munich [5–8] found that it is possible to form alkali metal-graphite, alkali metal - metal oxide and alkali metal – metal sulphide compounds under certain conditions and that the formation of these compounds was reflected by a sharp change in potential values of the graphite/oxide and sulphide materials. Their initial studies also pointed to the possibility of co-intercalation of solvent molecules into graphite resulting in a deterioration of the electrolyte. This problem would later be overcome by Rachid Yazami [9] who demonstrated the use of a solid electrolyte thereby eliminating the possibility of solvent co-intercalation. Whittingham would later demonstrate the first working prototype lithium based energy storage cell composed of a lithium anode/titanium di-sulphide cathode [10]. Subsequently, Goodenough and co-workers [11] demonstrated the use of a lithium cobalt oxide as a positive electrode material with a focus on raising the voltage obtainable in order to eliminate the use of lithium metal anodes which had issues of dendrite formation. Thackeray et.al [12] also demonstrated the possibility of using spinel LiMn_2O_4 for lithium insertion. In 1985 the first prototype LIB which utilized lithium ions ‘shuttling’ between a graphite anode and lithium cobalt oxide cathode was demonstrated by Akhira Yoshino of Asahi Chemical [13]. It took five more years until 1991 when Sony released the first commercial version of this prototype into the market. In 1994 Padhi and Goodenough [14] demonstrated the olivine LiFePO_4 which was a major upgrade in terms of safety and stability over LiCoO_2 .

It took roughly about 20 years for realizing the goal of fabricating a lithium ion based energy storage device that combined high energy and power density in a small volume while providing the ability to recharge in an economical manner. Ever since these initial discoveries, research has exploded into what is currently a multi-billion dollar industry. Today the best available cathode materials for rechargeable lithium batteries include the layered transition metal oxides (lithium nickel-cobalt-manganese/aluminium oxides), the spinel LiMn_2O_4 and olivine LiFePO_4 while for

anode, carbonaceous materials with the layered structure offer the most economical choice.

2.2 Operating principles and construction of LIBs & LICs

This section would discuss the basic working principle and construction of two types of lithium ion based energy storage devices. One is a lithium ion battery where charge is stored in two electrodes using a lithium ion that ‘shuttles’ between them. The other is a lithium ion hybrid supercapacitor where again only one of the electrodes operates via an intercalation mechanism to store charge whereas the other electrode stores charge using a capacitive mechanism.

A lithium ion battery consists of 4 main components as depicted in Fig 2.1 – the anode, cathode, separator and electrolyte. The anode and cathode are the host materials into which lithium ions intercalate and de-intercalate thus offering the ability to store charge and discharge when needed. The separator is an electrically insulating, ionically conducting material that prevents direct contact between the 2 electrodes and prevents a short circuit which can discharge the stored charge in a disruptive manner. The electrolyte consists of a lithium salt dissolved in a mixture of organic solvents. The anode and cathode are coated on metallic current collectors (typically Cu for cathode and Al for anode) to facilitate rapid charge transport.

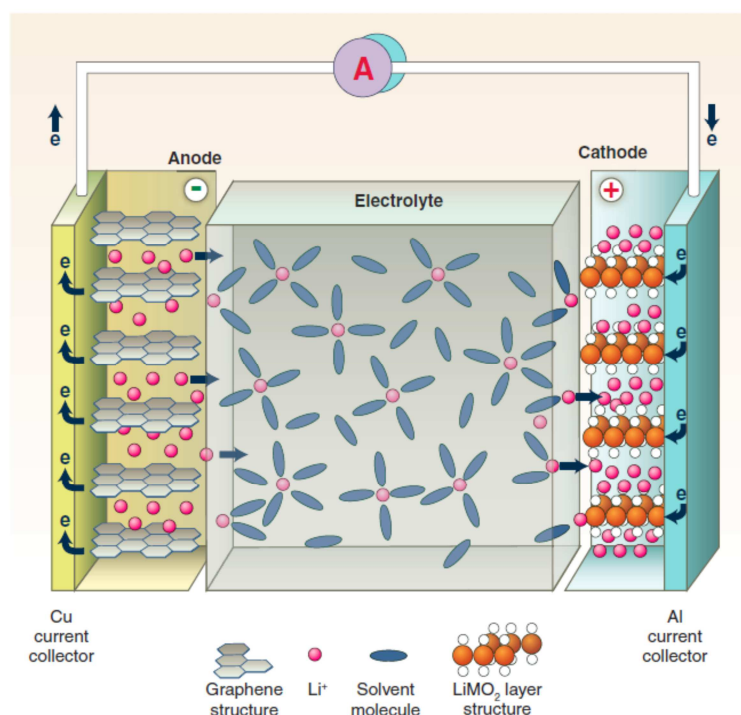


Fig 2.1 Schematic of lithium ion battery [15]

When a lithium ion cell is charged, a thermodynamic driving force is created by raising the one electrode to a different energy level/potential relative to the other electrode. This is achieved by applying a negative potential to the anode which forces out lithium ions from the cathode. Simultaneously a transition metal ion is oxidized in the cathode releasing electrons to compensate the charge loss occurring due to the release of a lithium ion from the structure. The lithium ion is now inserted into the structure of the anode where it combines with the electron released in the cathode and forms a compound (LiC_6 in case of graphite) which is in an unstable state. The moment the driving force creating this energy difference is removed, the system tends to look for ways to minimize the energy difference. Thus when the two electrodes are reconnected through an externally conducting medium (such as a wire for e.g), the unstable compound formed in the anode tends to convert back to lithium ions and the original parent compound releasing electrons in the process. These electrons are transferred through the external medium (wire) and this gives rise to useful electric current which is tapped as electrical energy. The electrons recombine with the transition metal oxide which is reduced back to its original valence state with the simultaneous insertion of lithium into the structure. This process of creating energy difference between two electrodes and allowing them to minimize the energy difference is in other words known as ‘charging’ and ‘discharging’ a lithium ion cell. It is obvious that the lithium ion ‘shuttles’ back and forth between the anode and cathode and for this reason lithium ion cells are often termed as ‘rocking chair’ cells as well. A connection of several lithium ion cells in series or parallel configurations offers the possibility of obtaining higher currents/voltages and such a collection of such cells is known as a battery.

In a commercial lithium ion cell, the cathode is made of a layered transition metal oxide ($\text{LiCoO}_2/\text{LiNi}_x\text{Mn}_y\text{Co}_{1-x-y}\text{O}_2$) or spinel manganese oxide (LiMn_2O_4) or an olivine lithium iron phosphate (LiFePO_4). The anode usually consists of graphite (synthetic/natural) which has layers of hexagonally bonded carbon atoms. Electrolytes employed are usually proprietary mixtures consisting of solvents such as alkyl carbonates such as ethylene/propylene/diethyl carbonates in different ratios together with a lithium salt such as lithium hexafluorophosphate (LiPF_6) or lithium perchlorate (LiClO_4). To enhance performance and stability, additives such as vinylene carbonate, lithium bis-oxalato borate are often added to the electrolytes. The separator is typically

fabricated from a polymer and is porous in order to allow electrolyte to form a continuous and ionically conducting path. It is also possible to modify and improve the lithium ion conductivity of the polymer itself.

In a typical lithium ion cell, the components need to be put together in such a way that energy can be stored and recovered with as little loss as possible. With this in mind, a tremendous amount of engineering research has gone into this leading to a widely accepted set of materials and configurations. Commonly available lithium ion cells come in 3 configurations namely coin cells, pouch/prismatic cells and cylindrical 18650 cells. All these contain the above discussed components assembled in a tightly packed frame that comes in different sizes and shapes.

Coming to the individual components themselves, both anodes and cathodes consist of a mixture of the active material which undergoes lithium insertion/extraction (graphite/layered oxides), a conductive additive (usually a carbon black) which enables fast transport of electrons to and from the active material and a polymeric binder (Teflon/other fluorinated polymers) which holds together the active material, conducting additive to the current collector and buffers volume changes during cycling. This electrode mixture is further coated on a metallic current collector in order to provide structural integrity to the electrode, easy handling and enable good electrical contact. Typically the cathode mixture is coated on aluminium foils while the anode is coated on copper foils. The reason for use of different current collectors for the anode and cathode arises due to the unavailability of a single cheap metal that can stably operate in the wide voltage range encountered in an LIB.

Amongst the many problems encountered in LIBs, reactivity with electrolyte [16–18], loss of active materials [19], thermal issues [20] and structural changes [21–23] present several formidable challenges in the construction of a low cost lithium ion cell with superior long term performance.

Capacitors typically work based on the principle of charge accumulation across a non-conducting interface known as a dielectric. A simple capacitor (Fig. 2.2) also known as a parallel plate capacitor consists of two plates of conducting materials such as steel/aluminium which are separated by a non-conducting medium. This non-conducting medium may simply be air/ a dielectric which offers higher amounts of charge storage capability. When connected to the terminals of a power source, positive and negative charges are accumulated on the respective plates. But since the medium

between the plates is non-conducting, the charges cannot combine and therefore are simply retained on the plates. During discharge, a conducting circuit is provided between the two charged plates resulting in a flow and recombination of charges which is nothing but the current generated from the device.

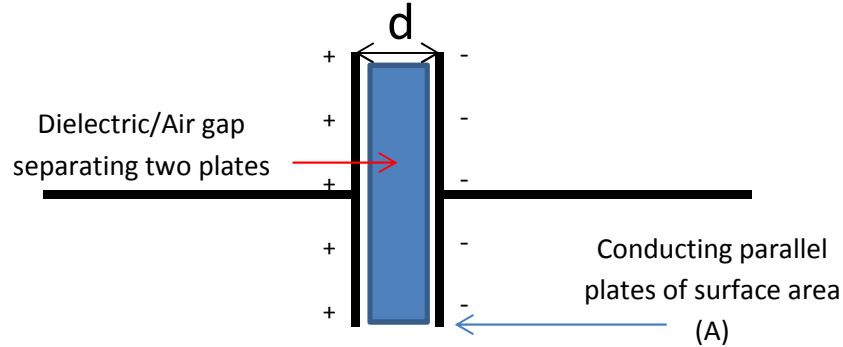


Figure 2.2 Schematic of a parallel plate capacitor.

Capacitance denotes the ability of a device to store charge and is usually calculated from the following equation

$$C = \epsilon_o \epsilon_r \frac{A}{d}$$

ϵ_o and ϵ_r represent the relative permittivity of free space and the dielectric medium between the two plates respectively, A is the surface area of the two plates and d is the distance of separation between the two plates.

This equation reveals that the capacitance is directly proportional to the surface area and inversely proportional to the distance of separation between the two plates. Thus in effect if the two parallel plates had somehow a greater surface area and could be brought as close to each other as possible, then it should be in theory to store larger amounts of charges. This fact is made use of in an electrochemical capacitor. The electrochemical capacitor or electrochemical double layer capacitor (EDLC) makes use of ion adsorption and the presence of a Helmholtz double layer to store charges. The Helmholtz double layer offers a charge separation distance in the range of nanometers thus tremendously increasing the charge storage ability. Moreover a material with rough surface would present a lot of adsorbing sites for the ion thus increasing the effective surface area (A). This again increases the capacitance. Thus supercapacitors can be considered as capacitors which can store many times more charge and can be discharged in about the same time. A typical electrochemical double layer capacitor would use high surface area carbon such as activated carbon which

provides a large number of sites for ion adsorption. Apart from double layer capacitance, there is another form of charge storage mechanism known as pseudocapacitance in which the only the surface of the active material is involved in redox reactions that enable charge storage. Hybrid supercapacitors employ both pseudocapacitance and double layer capacitance to store charge in the electrodes. The construction of a super capacitor would be in principle the same as that of a lithium ion battery. The differences would arise in the electrodes used. One of the electrodes would be activated carbon and the other would be a lithium ion intercalating material such as LiFePO_4 , LiMn_2O_4 etc.

The benefit that a hybrid super capacitor offers relative to battery is enhanced power density without sacrificing much of the energy density. Since charge is stored at the surface only, the redox processes would be faster unlike a battery where the charge is stored throughout the bulk of a material and hence redox processes would be slower leading to lower power densities.

The important thing in both lithium ion batteries and hybrid super capacitors is that both involve insertion of lithium ions in to the structure (although this happens only at the surface in a supercapacitor configuration). Hence for a single material used as both a supercapacitor electrode and lithium ion battery electrode, the degradation mechanisms occurring should be similar.

Hence, the focus of this work is to address structural changes encountered during cycling in spinel based manganese oxide materials. The subsequent sections will introduce the problems faced with manganese based oxides. Importance would be given to the issue of structural changes occurring in different manganese based spinel oxides and strategies employed to tackle them.

2.3 Spinel LiMn_2O_4 as lithium insertion host

Spinel oxides are a class of inorganic compounds with the general structural formula of AB_2O_4 . A is usually a cation with a valence +2 while B is another cation which can have a valence of +3/+4. A and B occupy the tetrahedral and octahedral voids formed in an arrangement of oxygen ions that has cubic close packing (CCP). The LiMn_2O_4 structure can be viewed as a collection of MnO_6 octahedra sharing edges and faces as shown in figure 2.3. Two types of tetrahedral interstitials are available. The 8a sites (yellow tetrahedra in fig 2.3) are found in the 3D channels formed by the various

MnO₆ octahedra while the 8b sites are found in the interstitial sites formed by the 4 MnO₆ octahedra that share edges. The lithium resides in 8a sites normally and when charged and discharged is taken out and re-inserted back into these sites. The manganese resides in the 16c octahedral sites.

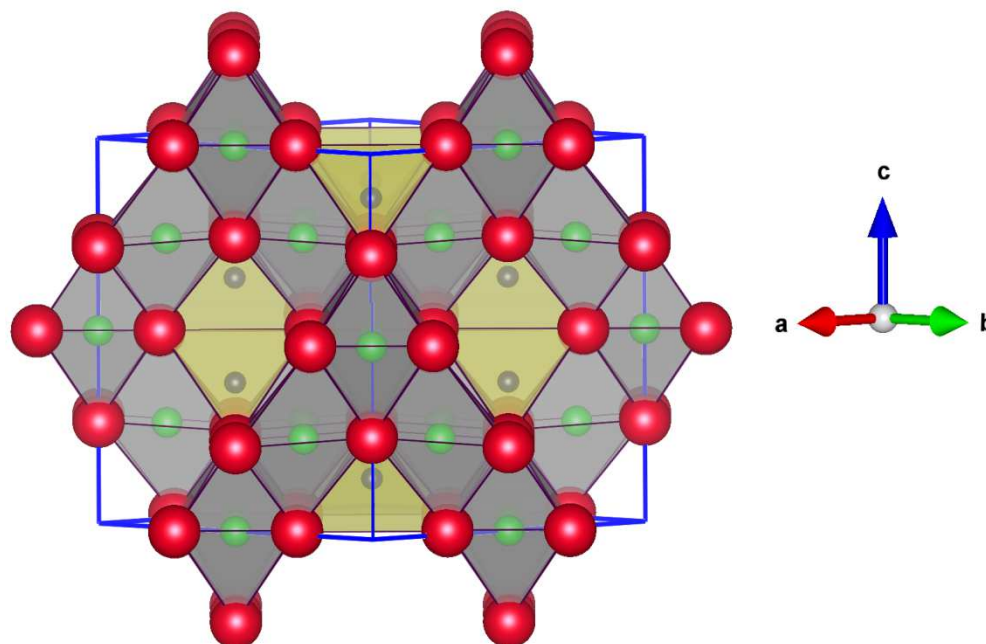


Figure 2.3 Crystal structure of spinel LiMn₂O₄ (generated using Vesta Software), Red spheres – oxygen, Green spheres – manganese and blue spheres (inside yellow tetrahedra) – lithium.

Investigation into the spinel lithium manganese oxides gained momentum rapidly since the commercialization of the first LIB based on lithium cobalt oxide and graphite anode in 1991 by Sony. It was soon realized that cobalt was expensive and toxic and the search was on for an alternative candidate. Spinel LiMn₂O₄ has a structure in which Li⁺ occupy 1/8th of the available tetrahedral voids while Mn³⁺ and Mn⁴⁺ are distributed in half of the available (1/2) octahedral voids. LiMn₂O₄ was first proposed by Thackeray et.al [12] as a prospective host material for Li⁺ insertion in 1983. They investigated electrochemical Li⁺ insertion into LiMn₂O₄ and Mn₃O₄ both of which had the spinel structure with an array of cubic close packed oxygen anions. They reported that the cubic phase LiMn₂O₄ undergoes a transformation to another phase Li₂Mn₂O₄ (with a tetragonal structure). However this phase seemed to co-exist with the cubic spinel phase. The Mn₃O₄ phase remains stable after Li⁺ insertion due to the reduction in the number of Mn³⁺ in the lattice. This first demonstration however presented a redox process occurring at a voltage of approximately 3V versus Li/Li⁺. The results

were further clarified by Ohzuku et.al. [24] who interpreted this transformation from a cubic to tetragonal phase as a change in symmetry which happens due to a 3 % reduction of the a-axis of the unit cell and 12.3 % increase in the c-axis of the cubic unit cell. Hence they theorized that the lattice made up of close packed oxygen anions is not destroyed during this transformation. Tarascon and Guyomard [25–27] were the first to demonstrate a full-cell configuration with a carbonaceous anode material. They successfully inserted 2 mols of Li^+ into $\text{Li}_x\text{Mn}_2\text{O}_4$. They were able to demonstrate an ‘AA’ cell configuration that cycled reasonably stably up to 400 cycles [28,29]. This system rivalled the commercially available LiCoO_2 based lithium ion cell and others such as Ni-Cd, Ni-MH in similar configurations. Ever since then a vast number of studies have been undertaken to understand the reasons for capacity fading and resulted in improvement of the room and elevated temperature cycling performance. Today spinel is employed in applications demanding high power for example portable drilling equipment.

It became apparent that the spinel electrodes operating in the 4V region are ideal choices for high voltage cathodes. Hence the focus quickly turned to understanding and eliminating the reasons for capacity fading. A number of studies were directed towards understanding the reasons. The major reasons could be categorized into the following: (i) electrolyte decomposition, (ii) oxygen non-stoichiometry (iii) manganese dissolution from active material, and (iii) Structural degradation due to Jahn-Teller effect. The following sections briefly discuss each of these mechanisms and the attempts that have been under taken to solve them.

Electrolyte degradation was a severe problem initially as the operating voltage of spinel (4.1V) was on the upper limit of electrolyte stability window of the existing electrolytes at that time (e.g: $\text{LiClO}_4/\text{LiBF}_4/\text{LiAsF}_6$ in mixtures of propylene carbonate/dimethoxyethane etc.). The more stable carbonate based electrolytes such as EC/DEC/DMC were not yet available. Tarascon et.al.[27,30,31] demonstrated the use of a stable electrolyte that overcame the issues related to decomposition. They used a proprietary electrolyte combination which was stable upto 4.8V vs Li/Li^+ to circumvent this issue. Later on the carbonate based electrolytes with higher stability would completely eliminate this problem. However it was observed that spinels would still undergo fading in spite of using stable electrolytes. It would become apparent that

the salt employed for generating the ions would become the problem as discussed in the subsequent sections.

The potential for application of spinel as a high voltage electrode became more intriguing with the report by Tarascon et.al [32] who claimed that cation mixing between Li and Mn on the 8a tetrahedral sites led to the emergence of a new plateau at 4.5V in spinels of the formula $\text{Li}_{1+x}\text{Mn}_{2-x}\text{O}_4$. It was later established by Gao and Dahn [33] that this peak (and another peak at 3.3V) was present because of oxygen non-stoichiometry. They later suggested that the oxygen stoichiometry is increased when the spinel is charged to progressively higher voltages and the 3.3 V peak could be used as a qualitative indicator of this effect [34]. More studies were performed signifying the effect of oxygen non-stoichiometry as an important factor affecting performance [35,36]. However with the advent of more stable electrolytes (and restricting the upper voltage limit during cycling) and carefully controlled synthesis parameters (temperature and cooling rate) this problem could be eliminated.

Thackeray et.al. [37] first discussed about the possibility of disproportionation of Mn^{3+} into Mn^{2+} and Mn^{4+} in the context of structural transformation observed from LiMn_2O_4 to a $\lambda\text{-MnO}_2$ phase. Jang et.al. [19,38] demonstrated that electrolyte decomposition could lead to generation of radical species that promote dissolution of manganese with the spinel acting as a catalytic surface for such reactions. They however tested with ether based electrolytes mainly (already pointed out in the earlier section as being unstable) and also indicate that carbonates are less susceptible to oxidation. Amatucci et.al. [39–43] showed that HF induced dissolution in the discharged state can also cause severe manganese dissolution and this effect is aided by increased surface area/reduced particle size. This mechanism exists even in carbonate based electrolytes which are considerably resistant to electrolyte decomposition unlike ether based solvents employed by Jang et.al. Trace amounts of moisture that can react with LiPF_6 and form HF is believed to be the major reason. They further demonstrate that an electrochemically inactive phase of protonated $\lambda\text{-MnO}_2$ is also present. This observation is also consistent with increased polarization reported by Jang et.al.[19].

Manganese dissolution has significant negative effects on the electrochemical performance of the cell. Not only does it result in loss of active material on the cathode side, it also results in manganese deposition on the anode [40] (graphite in case of LIBs) interfering with the formed SEI layer and ultimately the charge-discharge

processes. The exact mechanism behind this dissolution and deposition behaviour is still unclear. Ochida et.al.[44] have suggested that manganese is initially dissolved as Mn^{2+} in the electrolyte and migrates towards the anode where it is reduced to manganese metal and re-oxidized to Mn^{2+} in the SEI layer on graphite. Xiao et.al.[45] have conducted in-depth studies using HRTEM and XPS under controlled atmospheric conditions and determined that apart from metallic manganese clusters (which catalyse SEI formation on graphite), compounds such as LiF and MnF_2 were also present and these were responsible for cell polarization leading to a drop in performance. On the other hand, Zhan and co-workers [46] used XANES and XPS to identify the manganese valence state and claim that the deposited manganese has a valence state of +2 rather than being metallic as claimed by the others. They showed that Mn^{2+} was present in the SEI layer of different anodes well above the deposition potential of Mn (1.87 V vs. Li/Li^+) and proposed an ion exchange reaction with SEI layer that is leading to deposition of manganese. It would be appropriate to conclude that more work is necessary before a consensus could be reached on the nature and mechanism behind manganese deposition on anodes.

Being such a critical issue, plenty of efforts have been directed at solving the problem of manganese dissolution. Amatucci and co-workers proposed a surface coating technique [39] to create a physical barrier between the electrolyte and the active material surface that does not hinder Li^+ movement. Since this finding a number of coatings have been proposed to tackle capacity fading at elevated temperatures such as LTO [47], perovskite $\text{La}_{0.7}\text{Sr}_{0.3}\text{Mn}_{0.7}\text{O}_3$ [48], TiO_2 [49–51], ZrO_2 [50,52], Al_2O_3 [53,54], ZnO [55] and fluorides [56,57]. The coatings are proposed to act in a variety of ways including forming a physical barrier between the electrolyte and active material, scavenging traces of HF present in the electrolyte etc. Other ways of tackling such manganese dissolution have also been proposed. For example, Choi and Manthiram [58] suggested cationic and anionic substitutions can reduce manganese dissolution by forming stronger ionic bonds. The extent of manganese dissolution is also affected by the structural changes occurring. However surface coatings seem to be the most sought after method to tackle this problem since the formation of Mn^{3+} at the surface is necessary to have a redox reaction. There is still interest in understanding manganese dissolution better and tackling it via surface coatings [51,59]. However the major issue with coatings is there is no effective method to obtain a homogenous

coating. Moreover from an industrial perspective, the fabrication of coatings needs to be economical as it will be an additional processing step.

Apart from manganese dissolution, the other major issue was with structural degradation during cycling. It was clear that subjecting the spinel LiMn_2O_4 to insertion of more than 1 mol of Li^+ resulted in a structural change from a cubic to tetragonal phase. The reason behind such a transformation was attributed to the presence of a large concentration of the high spin Mn^{3+} ion. Octahedral complexes formed with high spin ions such as Mn^{3+} which have unevenly filled e_g orbitals have a tendency to undergo distortion in order to minimize the energy of the overall complex. This effect was proved by Hermann Arthur Jahn and Edward Teller and hence known as the Jahn-Teller effect. The spinel LiMn_2O_4 be visualized as a collection of octahedra of MnO_6 (a complex) that share edges/faces in which lithium ions occupy different voids available in the structure. Under such a condition, the octahedra formed by an Mn^{3+} ion would be distorted compared to an octahedra formed by Mn^{4+} (which is not a high spin ion) as shown in figure 2.4. In a stoichiometric spinel, the number of Mn^{3+} and Mn^{4+} is equal and they would be distributed homogenously in the structure in order to have the least distortion or energy. The cubic symmetry is maintained this way. However this delicate balance can be offset if the number of Mn^{3+} is larger than the number of Mn^{4+} . This is what happens on lithium insertion. The number of Mn^{3+} (and consequently the number of distorted MnO_6 octahedra) increases. Thus when all the MnO_6 octahedra ‘co-operatively’ distort along one axis (the c-axis), it is impossible to maintain the cubic symmetry anymore resulting in a tetragonal symmetry. Yamada et.al also show that it is possible for Jahn-Teller distortion to set in even at around room temperatures [60,61] in a stoichiometric spinel. They demonstrated that substitution of 0.035 mols of lithium for manganese in the octahedral sites is sufficient to alter the manganese valence to a value where the effect of Jahn-Teller distortion could be eliminated around room temperature.

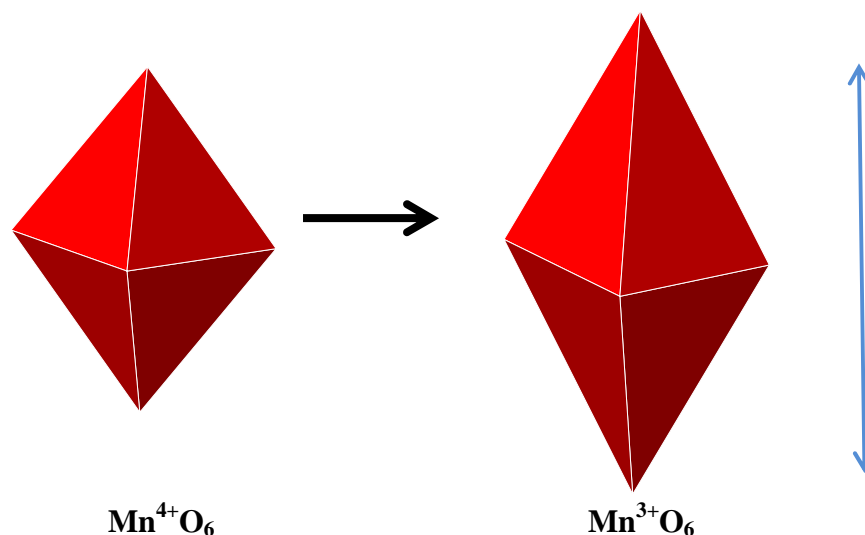


Figure 2.4 Schematic of effect of Jahn-Teller distortion

Initially it was believed that the co-operative Jahn-Teller distortion occurs only when the Li^+ concentration exceeds 1 mole in LiMn_2O_4 (while cycling over the 2.8 - 3V region) in the bulk of the material. Later it was realised that the effect could set in even at around 3.3 – 3.5 V vs. Li/Li^+ at the surface of spinel particles under non-equilibrium conditions (e.g high rates of discharge) [21]. Then the surface of the particles would encounter more lithium than the bulk/interior during lithium insertion. Proof for such a mechanism was presented by Thackeray et.al.[62] through transmission electron microscopy studies of electrodes cycled to 3.5V. Cho and Thackeray [63] later demonstrated that the tetragonal spinel phase at the surface transforms to Li_2MnO_3 through the formation of soluble MnO and this is responsible for part of the observed capacity fading. Initially it was proposed that the Jahn-Teller distortion results in a change of the c-axis of the cubic spinel leading to the formation of the tetragonal spinel. The accompanying volume change would be too large for a particle to sustain and it would disintegrate with repeated cycling. This can lead to a loss of electrical contact eventually resulting in inaccessible lost capacity [64]. However through a series of studies, Goodenough and co-workers [65–67] pointed out that this may not be the exact mechanism. They demonstrated this by separating capacities obtained from the 3V and 4V plateaus when a cell containing LiMn_2O_4 was cycled in a wide voltage range from 2.4 – 4.4 V. They observed that capacity loss was occurring only from the 3V plateau. If electrical contact is lost, capacity should be inaccessible while cycling on the 4V plateau as well which did not seem to be the case. Hence they proposed an intra-particle mechanism to explain this behaviour. They

theorized that during cycling in the 3V region, there is an interphase layer between the tetragonal $\text{Li}_2\text{Mn}_2\text{O}_4$ and cubic LiMn_2O_4 that is formed on the surface of the particles. This interphase moves towards the centre of the particle as the amount of lithium inserted increases. Since this is an interphase between two different structures (cubic and tetragonal), dislocations would need to be created in this layer in order to minimize strains and maintain continuity. They proposed it might be possible that the lithium ions in the more mobile octahedral 16d sites could move to these dislocations and lock up the dislocations. This would then immobilize the interphase and would inhibit further lithiation. Such a mechanism would not occur in the 4V region as there is no cubic/tetragonal interphase formed. Hence there is no capacity loss observed while cycling in the 4V region.

Irrespective of the differences in interpreting the exact mechanism for capacity loss due to Jahn-Teller distortion, it could be seen that the structural change arising due to Jahn-Teller distortion was problematic. Hence it was necessary to tackle the structural changes. It can be intuitively understood that modifying the electronic environment around the manganese ions should result in a different and potentially improved behaviour. The easiest way to achieve such a modification would be via elemental substitutions in the spinel. A number of studies have focused on employing different substitutions – both for the cations ($\text{Li}^+/\text{Mn}^{4+}$) and anions (O^{2-}). In the following section, an attempt is made to discuss such studies. The studies have been categorized into those which focus on improving the performance in the 4V region and those that focus on the 3V region.

It was evident that an oxide that can reversibly intercalate lithium at 4V would give rise to a system with higher energy density. Hence a large number of studies with substitutions were performed in this regard to address the issue of structural degradation and improve capacity retention during cycling.

Tarascon et.al. [25] had already attempted substitution of a host of elements such as Ti, Ge, Fe, Zn and Ni for Mn in the spinel LiMn_2O_4 . But their stated aim was not to tackle the problem of structural change. Rather they were interested in eliminating the sudden voltage drop step of 1V which posed a problem while considering an application for the material. They attempted to smooth out this voltage step by employing substitutions but realized that none of the substitutions could eliminate this voltage drop. Also the substitutions resulted in a decreased capacity in case of

$\text{Ni}^{2+}/\text{Zn}^{2+}/\text{Fe}^{3+}$ since these required charge compensation by conversion of some of the active Mn^{3+} to Mn^{4+} . Finally they reported no change in cycling stability with the various substitutions.

Gummow et.al. [68] were the first to present elemental substitution as a strategy to combat the problem of Jahn - Teller distortion. Their rationale was to adjust the average manganese valence to >3.5 since it was observed that the critical manganese valence for the Jahn-Teller effect to set in below 3.5. They achieved this by substituting Li^+ with cations such as Mg^{2+} , Zn^{2+} or Li^+ for Mn^{3+} resulting in increased manganese valence for charge compensation (basically increasing the number of Mn^{4+} in the structure). They reported that while all the methods enhance cycling stability at room temperature in the 4V region, it results in a reduced capacity owing to the reduction in the number of active Mn^{3+} ions. They also demonstrate that the spinels containing excess lithium (i.e substitution of manganese with more lithium) displayed good performance when cycled all the way to 2.5V vs. Li/Li^+ . Amatucci et.al. [69] observed that as long as the lattice parameter is below 8.23 Å in the discharged state of the spinel, capacity fading could be minimized at both room and elevated temperatures. Hence they suggested co-substitution of both manganese and oxygen with aluminium and fluorine in the spinel to reduce the lattice parameter and thereby alleviate capacity fading in the 4V region. Their results are interesting considering that the average manganese valence in the Al- & F- co-substituted spinel is 3.3 (Jahn-Teller distortion is expected to set in below an average valence of 3.5) and still they were able to demonstrate a significantly enhanced performance. They proposed an explanation for their observation based on the nature of bonds (i.e ionic/covalent) and the smaller size of manganese octahedra formed. Bittihn et.al. [70] demonstrated the possibility of using a small amount of cobalt substitution to enhance the performance of the spinel in the 4V region although they do not clarify the reasons for such an improvement. A number of other groups have also attempted cobalt substitution with some success [71,72]. Wakihara and co-workers [73] demonstrated the effect of Co, Cr and Ni substitution on the performance and attribute the improved cycling stability in the 4V region to the increased M-O bond strength for Cr/Co and Ni compared to Mn. They suggested that the stronger M-O bonds prevent structural transformation. Subsequently they demonstrate much improved performance in the 4V region for an Al-Cr/Co co-substituted spinel and explain the improvement in performance based on

a stronger Al-O bonding which in turn results in an increased Li^+ diffusion co-efficient as well as reduced Jahn-Teller distortion [74]. They demonstrate the absence of Jahn-Teller distortion through a DSC study where a signature peak is observable for the tetragonal spinel phase which is based on the earlier studies by Yamada and Tanaka [60,61]. Li et.al.[75] adopt an approach in which they modified the surface of LiMn_2O_4 with a layer of $\text{LiNi}_x\text{Mn}_{2-x}\text{O}_4$. They report a significantly enhanced cycling stability in the 4V region for the spinel containing nickel and attribute it to the absence of Jahn-Teller distortion. Zhao et.al. report co-substitution with Mg^{2+} and Si^{4+} [76] and claim that the equimolar co-substitution minimizes Jahn-Teller distortion thereby improving performance in the 4V region. Wen [77] reported the effect of co-substitution of Mg^{2+} and F^- and demonstrate very good cycling stability in the 4V region at 1C rate for over 400 cycles at both room temperature and 55 °C. They show that the transformation to tetragonal phase is suppressed from ex-situ XRD analysis. Substitution with a host of other elements have also been attempted such as Fe [78], Cu [79], Ga [80], B [81], Ti [82,83], rare earth elements [84,85]. For the sake of brevity a detailed discussion on these studies is not presented. It would suffice to say that all the studies with substitutions reported performance improvement to different extents in the 4V region for the spinels. Reasonably good performance has been established at room temperature although elevated temperature performance continues to pose a challenge.

In comparison to the number of studies that focus on improving the performance in the 4V region, the number of studies focussing on the 3V region has been rather limited. This is understandable since the energy density obtained in the 3V region would be obviously lower compared to the 4V region.

Strobel and co-workers [86] studied the evolution of the 3V behaviour of spinels substituted with Al and Mg in the hope of reducing Jahn-Teller related effects with the substitutions. However they chose fixed compositions LiAlMnO_4 and $\text{LiMg}_{0.5}\text{Mn}_{1.5}\text{O}_4$ respectively as allowed by the charge balancing calculations. They reported difficulties in obtaining a pure phase LiAlMnO_4 while they were able to accomplish magnesium substitution without impurity phases. However both materials had very low capacities and cycled rather poorly and were still susceptible to Jahn-Teller distortion. Yoshio and co-workers [87,88] later showed that Al substitution may in fact have a negative effect on performance in the 3V region. They proposed that Al^{3+} stabilizes the cubic

structure and prevents its transformation to a tetragonal structure during Li^+ insertion. This inability to transform to the tetragonal structure in turn results in poor cycling performance in the 3V region. Pistoia et.al. [89] had reported the effect of Cr doping on the 3V performance of spinels. However under the synthesis conditions employed they formed an oxygen rich spinel of the form $\text{LiCr}_x\text{Mn}_{2-x}\text{O}_{4.35}$ which displayed stable capacities up to 50 cycles. Baochen et.al.[90] studied the effect of Cr^{3+} substitution for Mn^{3+} in the octahedral sites of spinel and report improvement over 5 cycles. Sun and Jeon [91] investigated the effect of anion substitution in spinel LiMn_2O_4 by replacing a small amount of oxygen with sulphur. Their results indicate that during cycling in the voltage range of 2.4 – 3.5V, the spinel displays reasonable capacity retention over 20 cycles with no evidence of transformation to tetragonal phase from ex-situ XRD. They also studied compounds with $\text{Cr}^{3+}/\text{Al}^{3+}$ and S^{2-} substituting Mn^{3+} and O^{2-} respectively which display improved performance while cycling over both 3V and 4V plateaus for 50 cycles [92,93]. However Goodenough et.al. suggested it is possible that sulphur may not be able to substitute oxygen in the lattice owing to its significantly larger ionic radius and presumably stays on the surface and somehow improves performance. They demonstrate this by performing an experiment with a chloride ion which does not substitute into the structure but still improves cyclability in the 3V region [66]. However it should be noted that they were unable to detect chlorine during the characterization tests and only postulate a chlorine modified surface to explain their results. Kang et.al. [65] also report improved performance in the 3V region for ball milled spinel LiMn_2O_4 and attribute this to a combination of the presence of strains from ball milling, nanograins and a higher manganese valence state. Amine et.al [94,95] investigated the effect of substitution of 0.5/1 mol of manganese in LiMn_2O_4 with either Ni/Fe. They claimed that the presence of Ni stabilizes the structure against transformation during cycling in the 3V region. However the presence of Fe does not prevent the cubic – tetragonal transformation from occurring. They were able to demonstrate an initial capacity of 160 mAh.g^{-1} which decreases to 150 mAh.g^{-1} after 10 cycles. They proposed that Jahn-Teller distortion does not occur in the Ni substituted material and hence the performance is improved compared to the Fe substituted material. In order to demonstrate this point, they inserted 1 mol of Li^+ chemically into $\text{LiNi}_{0.5}\text{Mn}_{1.5}\text{O}_4$ and showed that the structure of the resulting $\text{Li}_2\text{Ni}_{0.5}\text{Mn}_{1.5}\text{O}_4$ phase is also cubic. However, Park et.al. [96] later demonstrated that a

cubic spinel with $Fd\bar{3}m$ symmetry (a disordered structure with Ni and Mn randomly distributed over the 16d octahedral sites) converts to a tetragonal structure with $I4_1/amd$ symmetry. They also show that a cubic spinel with the $P4_332$ symmetry (an ordered structure in which the Ni and Mn are uniformly distributed in the 16d octahedral sites) undergoes a reversible transformation to tetragonal spinel during lithium insertion. Finally the capacity demonstrated was about $60 - 70 \text{ mAh.g}^{-1}$ after 50 cycles. It is quite possible that Amine et.al. prepared the $P4_332$ form of the spinel via the low temperature sol-gel process (not discussed in their report) since it is now known that at synthesis temperatures $< 600^\circ\text{C}$, the ordered form of the nickel substituted spinel is more stable. Sun and co-workers [97] also demonstrated that nickel and sulphur substitutions produce a spinel with modified surface texture and particle size. Their data however does not show any noticeable difference in stability between the substituted and un-substituted. Rather they were able to demonstrate a marginally increased capacity obtainable from the sulphur containing spinels. They also state that the location of the sulphur (i.e whether in the lattice/on the surface) is not clear.

2.4 Spinel $\text{Li}_4\text{Mn}_5\text{O}_{12}$ as lithium insertion host

Spinel $\text{Li}_4\text{Mn}_5\text{O}_{12}$ is another of the cubic class of spinels which gained interest together with the investigation of the LiMn_2O_4 . The spinel $\text{Li}_4\text{Mn}_5\text{O}_{12}$ can be expressed in the form $\text{Li}_{1.33}\text{Mn}_{1.67}\text{O}_4$ or $\text{Li}[\text{Li}_{0.33}\text{Mn}_{1.67}]\text{O}_4$ to make the site occupancy clear. This expression makes it easy to understand that a portion of the Mn in the 16d octahedral sites of a normal $\text{Li}[\text{Mn}_2]\text{O}_4$ are occupied with Li. Basically it has the same cubic close packed lattice of oxygen (see figure 2.5) in which the voids are occupied in a different manner. In order to have charge balance, all the manganese will be in the +4 state which would then make lithium extraction from the structure impossible at 4V vs. Li/Li^+ as in the case of stoichiometric spinel LiMn_2O_4 . However insertion of Li^+ into the structure is possible at 3V vs. Li/Li^+ with a theoretical capacity of 163 mAh.g^{-1} for insertion of 3 mol of Li^+ . The most attractive feature of this compound though was the possibility of avoiding J-T distortion related effects during cycling since the average manganese valence after insertion of 3 mol of Li^+ would be 3.4 which is only slightly lesser than the critical value of 3.5 observed in a stoichiometric LiMn_2O_4 .

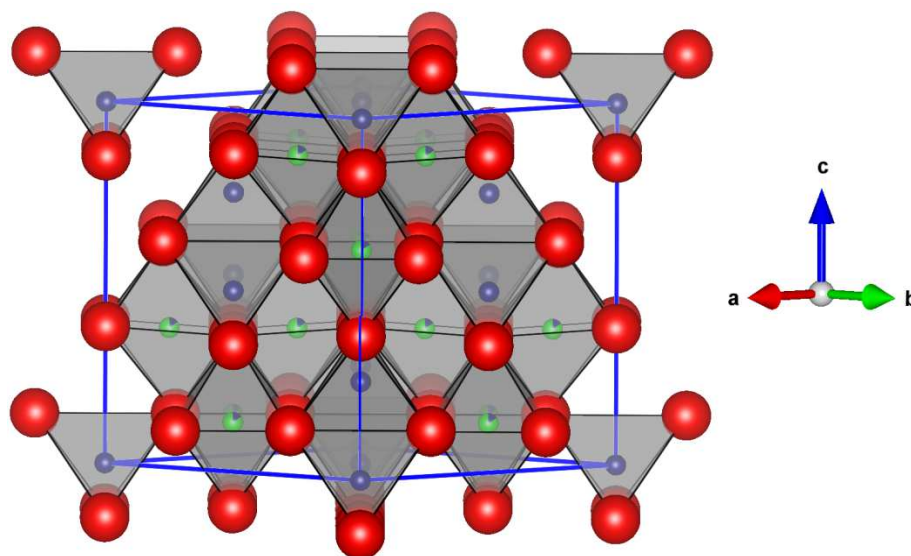


Figure 2.5 Crystal structure of $\text{Li}_4\text{Mn}_5\text{O}_{12}$ ($\text{Li}_{1.33}\text{Mn}_{1.67}\text{O}_4$), Red spheres – oxygen, Green spheres – Manganese, Blue spheres – Lithium.

.Thackeray et.al. [98] reported on the synthesis and characterization of two spinel phases - $\text{Li}_2\text{Mn}_4\text{O}_9$ and $\text{Li}_4\text{Mn}_5\text{O}_{12}$ and compared its performance to the stoichiometric LiMn_2O_4 phase in the 3V region. They proposed that of the 3 spinel samples investigated, $\text{Li}_4\text{Mn}_5\text{O}_{12}$ had the best combination of capacity obtainable and stability. Richard et.al. [99] attempted to extract lithium from $\text{Li}_4\text{Mn}_5\text{O}_{12}$ by introducing oxygen deficiency so as to convert some of the manganese to from +4 to +3 state. They reduced the synthesised material with ammonia and successfully removed oxygen to yield a compound of the form $\text{Li}[\text{Li}_{0.33}\text{Mn}_{1.67}]\text{O}_{4-\delta}$. However neither of the reports presented data on long term performance. Further the capacity was lesser than the theoretically calculated value of 163 mAh.g^{-1} . Ferg et.al. [100] demonstrated the possibility of coupling $\text{Li}_4\text{Mn}_5\text{O}_{12}$ with a spinel LiMn_2O_4 to form a full cell with an average voltage of 1.15 V vs. Li/Li^+ . However coupling with $\text{Li}_4\text{Ti}_5\text{O}_{12}$ produced a cell with an average voltage that is higher by 1.3V roughly making the manganese containing spinel unattractive. Robertson et.al. [101] demonstrated doping $\text{Li}_4\text{Mn}_5\text{O}_{12}$ with Co. They demonstrate improved cycling stability in the voltage range 2.4 – 4.8V. They attribute this to an improved stability to oxygen loss which occurs while charging $\text{Li}_4\text{Mn}_5\text{O}_{12}$ to a higher voltage. While these initial reports did not focus much on the synthesis technique/conditions, it was soon realised that synthesizing a stoichiometric lithium rich spinel was very challenging. Thackeray et.al [102] discovered that the lithium rich spinel $\text{Li}_4\text{Mn}_5\text{O}_{12}$ decomposes to

Mn₃O₄ and Li₂O on heating in the range 420 - 930 °C. Heating at temperatures > 930 °C resulted in the formation of phases like LiMnO₂ and LiMn₂O₄. Takada et.al. [103–107] conducted a series of studies to understand the effect of various synthesis conditions and observed that spinel Li₄Mn₅O₁₂ decomposes at higher temperatures to LiMn₂O₄, Li₂MnO₃ and LiMnO₂. The temperatures for such decomposition is also affected by the gases employed. Inert atmospheres were shown to decrease the critical temperature for decomposition. They observed that a reversible decomposition of spinel Li₄Mn₅O₁₂ occurs on heating in oxygen atmospheres from around 400 – 700 °C which is in line with the observation of Thackeray earlier. Choi and Manthiram [108] suggested partial substitution of oxygen with fluorine to eliminate the problem of second phase formation during synthesis at temperatures above 500 °C. It was soon realised that the use of low temperatures presented two problems. Firstly there was not enough energy to drive diffusion related processes which resulted in incomplete reactions. Secondly, the crystallinity of the obtained materials was not good enough to offer stable cycling performances. The less than theoretical capacities demonstrated are further evidence of this problem. Thus different synthesis methods have been investigated to prepare spinel Li₄Mn₅O₁₂ ranging from hydrothermal [109], spray drying assisted solid state [110], sol-gel [111] and molten salt routes [112]. While these methods were able to provide for high purity materials, the cost factor and/or the marginal increase in performance possibly was not attractive enough to pursue further these methods.

Structurally, Li₄Mn₅O₁₂ is expected to be stable during insertion of up to 2.5 mols of lithium. It was already mentioned that to obtain the theoretical capacity of 163 mah.g⁻¹, the average valence of the manganese would have to reduce to 3.4 which is below the critical valence of 3.5 for Jahn-Teller distortion to set in (in spinel LiMn₂O₄). Hence one cannot possibly rule out J-T distortion from occurring although structurally, the lithium excess spinel is different from its stoichiometric counterpart LiMn₂O₄ in that the lattice parameter 'a' for LiMn₂O₄ spinel is about 8.251 Å compared to the 8.159 Å for Li₄Mn₅O₁₂. Julien et.al. [113,114] also demonstrated the change from cubic to tetragonal symmetry on lithium insertion into Li₄Mn₅O₁₂ via ex-situ Raman analysis. Choi and Manthiram [108] also pointed out in their work that un-substituted spinel Li₄Mn₅O₁₂ transforms to Li₂MnO₃ during cycling. Hence structural transformation is not completely prevented in the Li₄Mn₅O₁₂. As in the case of spinels,

it could then be theorized that substitutions could probably alter this behaviour. As pointed out earlier Robertson et.al. had investigated Co substitution. Le et.al.[115] investigated a series of solid solutions of Ti and Mn in $\text{Li}_4\text{Ti}_x\text{Mn}_{5-x}\text{O}_{12}$ ($0 < x < 5$) but however do not describe long term performance. They demonstrated that Ti substitution leads to a progressively larger unit cell with increasing Ti due to the bigger size of the Ti^{4+} ion. Apart from these studies, there have been no other investigations of substitutions.

Another approach to improve structural stability involves developing composite Li_2MnO_3 - $\text{Li}_4\text{Mn}_5\text{O}_{12}$ materials [116–118] in which the $\text{Li}_4\text{Mn}_5\text{O}_{12}$ is embedded in a matrix of Li_2MnO_3 . By virtue of the nano-sized domains of the two different materials, effects associated with J-T distortion such as lattice expansion could be suppressed effectively. Recently Ivanova et.al. [118,119] showed that it is possible to have a non-uniform distribution of manganese in these alternating nano-domains of $\text{Li}_4\text{Mn}_5\text{O}_{12}$ and layered Li_2MnO_3 thus resulting in poor performance.

2.5 Questions to answers based on literature

The above review of literature identifies gaps which can be summarized in to the following questions.

- Has there been a systematic investigation into the electrochemical performance in the 3V region for spinel based manganese oxides?
- Has the effect of substitutions on electrochemical performance in the 3V region been investigated in a systematic manner?
- Recent advances in nanotechnology have opened up new avenues for investigation due to the novel properties offered. Can this be tapped to tackle problems in spinel based manganese oxides together with elemental substitutions? Has the effect of nanostructuring or morphology on electrochemical performance been investigated for the spinel based manganese oxides?
- Finally can such investigations lead to the fabrication of full cell devices that demonstrates long term cycling performance, good rate capability?

2.6 PhD in context of literature

This work will address the questions posed in the preceding section. Elemental substitutions (Nickel substitution in spinel LiMn_2O_4 and Ti substitution in $\text{Li}_4\text{Mn}_5\text{O}_{12}$) are investigated and their role in improving the electrochemical performance in the 3V

region will be studied. The effect of morphology and nano-structuring will be investigated. Finally full cell devices based on the best available material from these studies will be demonstrated.

References

- [1] M.S. Whittingham, *J. Chem. Soc. Chem. Commun.* (1974) 328 – 329.
- [2] M.S. Whittingham, *Mater. Res. Bull.* 9 (1974) 1681–1690.
- [3] G.V.S. Rao, *Mater. Res. Bull.* 9 (1974) 921 – 926.
- [4] R. Schöllhorn, H. Meyer, *Mater. Res. Bull.* 9 (1974) 1237–1246.
- [5] A.L. R.Schollhorn, E.Sick, *Mater. Res. Bull.* 10 (1976) 1005–1012.
- [6] J.O. Besenhard, H.P. Fritz, *J. Electroanal. Chem. Interfacial Electrochem.* 53 (1974) 329–333.
- [7] J.O. Besenhard, *Carbon N. Y.* 14 (1976) 111–115.
- [8] R. Schöllhorn, R. Kuhlmann, J.O. Besenhard, *Mater. Res. Bull.* 11 (1976) 83–90.
- [9] R. Yazami, P. Touzain, *J. Power Sources.* 9 (1983) 365–371.
- [10] M.S. Whittingham, *Science (80-.).* 192 (1976) 1126–1127.
- [11] K. Mizushima, P. Jones, P. Wiseman, J. Goodenough, *Mater. Res. Bull.* 15 (1981) 783–789.
- [12] M. Thackeray, W. David, P.G. Bruce, J.B. Goodenough, *Mater. Res. Bull.* 18 (1983) 461–472..
- [13] M. Sugimoto, *IEEE Ann. Hist. Comput.* 35 (2013) 82–85.
- [14] A.K. Padhi, K.S. Nanjundaswamy, J.B. Goodenough, *J. Electrochem. Soc.* 144 (1997) 1188 – 1193.
- [15] B. Dunn, H. Kamath, J. Tarascon, *Science (80-.).* 334 (2011) 928–935.
- [16] D. Aurbach, *J. Electrochem. Soc.* 142 (1995) 2882–2890.
- [17] K. Edström, T. Gustafsson, J.O. Thomas, *Electrochim. Acta.* 50 (2004) 397–403.
- [18] C. Wang, A.J. Appleby, F.E. Little, *J. Electroanal. Chem.* 519 (2002) 9–17.

- [19] Dong H, Jang, Y.J. Shin, S.M. Oh, *J. Electrochem. Soc.* 143 (1996) 2204–2211.
- [20] T.M. Bandhauer, S. Garimella, T.F. Fuller, *J. Electrochem. Soc.* 158 (2011) R1–R25.
- [21] M.M. Thackeray, *J. Electrochem. Soc.* 142 (1995) 2558–2563.
- [22] H. Wang, Y.-I. Jang, B. Huang, D. Sadoway, Y.-M. Chiang, *J. Electrochem. Soc.* 146 (1999) 473–480.
- [23] R. Hausbrand, G. Cherkashinin, H. Ehrenberg, M. Gröting, K. Albe, C. Hess, et al., *Mater. Sci. Eng. B.* 192 (2014) 1–22.
- [24] T. Ohzuku, M. Kitagawa, T. Hirai, *J. Electrochem. Soc.* 137 (1990) 769 – 775.
- [25] J.M. Tarascon, W. E. S. F.K., W.R. McKinnon, S. Colson, *J. Electrochem. Soc.* 138 (1991) 2859 – 2864.
- [26] J.M. Tarascon, D. Guyomard, *J. Electrochem. Soc.* 138 (1991) 2864–2868.
- [27] D. Guyomard, J.M. Tarascon, *J. Electrochem. Soc.* 139 (1992) 937 – 948.
- [28] J.M. Tarascon, D. Guyomard, G.L. Baker, *J. Power Sources.* 44 (1993) 689–700.
- [29] J.M. Tarascon, D. Guyomard, *Electrochim. Acta.* 38 (1993) 1221–1231.
- [30] D. Guyomard, J.M. Tarascon, *J. Power Sources.* 54 (1995) 92–98.
- [31] D. Guyomard, J.M. Tarascon, *J. Electrochem. Soc.* 140 (1993) 3071–3081.
- [32] J.M. Tarascon, W.R. McKinnon, F. Coowar, T.N. Bowmer, G. Amatucci, D. Guyomard, *J. Electrochem. Soc.* 141 (1994) 1421–1431.
- [33] Y. Gao, J.R. Dahn, *J. Electrochem. Soc.* 143 (1996) 100–114.
- [34] Y. Gao, J.R. Dahn, *Solid State Ionics.* 84 (1996) 33–40.
- [35] B. Deng, H. Nakamura, M. Yoshio, *J. Power Sources.* 180 (2008) 864–868.
- [36] X. Wang, H. Nakamura, M. Yoshio, *J. Power Sources.* 110 (2002) 19–26.
- [37] M.M. Thackeray, P.J. Johnson, L. a. de Picciotto, P.G. Bruce, J.B. Goodenough, *Mater. Res. Bull.* 19 (1984) 179–187.
- [38] D.H. Jang, *J. Electrochem. Soc.* 144 (1997) 3342.
- [39] G.G. Amatucci, A. Blyr, C. Sigala, P. Alfonse, J.M. Tarascon, *Solid State*

- Ionics*. 104 (1997) 13–25.
- [40] A. Blyr, G.G. Amatucci, D. Guyomard, Y. Chabre, J.-M. Tarascon, *J. Electrochem. Soc.* 145 (1998) 194–209.
- [41] G. Amatucci, a Du Pasquier, a Blyr, T. Zheng, J. Tarascon, *Electrochim. Acta*. 45 (1999) 255–271.
- [42] G.G. Amatucci, C.N. Schmutz, a Blyr, C. Sigala, a S. Gozdz, D. Larcher, et al., *J. Power Sources*. 69 (1997) 11–25.
- [43] A. Du Pasquier, a Blyr, P. Courjal, D. Larcher, G. Amatucci, B. Gérard, et al., *J. Electrochem. Soc.* 146 (1999) 428–436.
- [44] M. Ochida, Y. Domi, T. Doi, S. Tsubouchi, H. Nakagawa, T. Yamanaka, et al., *J. Electrochem. Soc.* 159 (2012) A961–A966.
- [45] X. Xiao, Z. Liu, L. Baggetto, G.M. Veith, K.L. More, R.R. Unocic, *Phys. Chem. Chem. Phys.* 16 (2014) 10398–402.
- [46] C. Zhan, J. Lu, a Jeremy Kropf, T. Wu, A.N. Jansen, Y.-K. Sun, et al., *Nat. Commun.* 4 (2013) 2437.
- [47] J. Li, Y. Zhu, L. Wang, C. Cao, *Appl. Mater. Interfaces*. 6 (2014) 18742 – 18750.
- [48] T. Shi, Y. Dong, C.-M. Wang, F. Tao, L. Chen, *J. Power Sources*. 273 (2015) 959–965.
- [49] L. Yu, X. Qiu, J. Xi, W. Zhu, L. Chen, *Electrochim. Acta*. 51 (2006) 6406–6411.
- [50] K. A. Walz, C.S. Johnson, J. Genthe, L.C. Stoiber, W. A. Zeltner, M. A. Anderson, et al., *J. Power Sources*. 195 (2010) 4943–4951.
- [51] J. Lu, C. Zhan, T. Wu, J. Wen, Y. Lei, a J. Kropf, et al., *Nat. Commun.* 5 (2014) 5693.
- [52] M.M. Thackeray, C.S. Johnson, J.S. Kim, K.C. Lauzze, J.T. Vaughey, N. Dietz, et al., *Electrochem. Commun.* 5 (2003) 752–758.
- [53] A. M. Kannan, a Manthiram, *Electrochem. Solid-State Lett.* 5 (2002) A167.
- [54] A. Eftekhari, *Solid State Ionics*. 167 (2004) 237–242.
- [55] Y.-K. Sun, K.-J. Hong, J. Prakash, *J. Electrochem. Soc.* 150 (2003) A970.

- [56] S. Zhao, Y. Bai, Q. Chang, Y. Yang, W. Zhang, *Electrochim. Acta.* 108 (2013) 727–735.
- [57] Q. Chen, Y. Wang, T. Zhang, W. Yin, J. Yang, X. Wang, *Electrochim. Acta.* 83 (2012) 65–72.
- [58] W. Choi, A. Manthiram, *J. Electrochem. Soc.* 153 (2006) A1760–A1764.
- [59] S.R. Gowda, K.G. Gallagher, J.R. Croy, M. Bettge, M.M. Thackeray, M. Balasubramanian, *Phys. Chem. Chem. Phys.* 16 (2014) 6898–902.
- [60] A. Yamada, *J. Solid State Chem.* 122 (1996) 160–165.
- [61] A. Yamada, M. Tanaka, *Mater. Res. Bull.* 30 (1995) 715–721.
- [62] M.M. Thackeray, Y. Shao-Horn, A.J. Kahaian, K.D. Kepler, E. Skinner, J.T. Vaughey, et al., *Electrochem. Solid-State Lett.* 1 (1998) 7–9.
- [63] J. Cho, M.M. Thackeray, *J. Electrochem. Soc.* 146 (1999) 3577.
- [64] M.M. Thackeray, *Prog. Solid State Chem.* 25 (1997) 1–71.
- [65] S.H. Kang, J.B. Goodenough, L.K. Rabenberg, *Chem. Mater.* 13 (2001) 1758–1764.
- [66] S.-H. Kang, J.B. Goodenough, *J. Electrochem. Soc.* 147 (2000) 3621 – 3627.
- [67] S.-H. Kang, J.B. Goodenough, *Electrochem. Solid-State Lett.* 3 (1999) 536–539.
- [68] R. Gummow, A. De Kock, M. Thackeray, *Solid State Ionics.* 69 (1994) 59–67.
- [69] G.G. Amatucci, N. Pereira, T. Zheng, J.-M. Tarascon, *J. Electrochem. Soc.* 148 (2001) A171–A182.
- [70] R. Bittihn, R. Herr, D. Hoge, *J. Power Sources.* 43 (1993) 223–231.
- [71] J.M. Amarilla, J.L.M. de Vidales, R.M. Rojas, *Solid State Ionics.* 127 (2000) 73–81.
- [72] M. Wohlfahrt-Mehrens, A. Butz, R. Oesten, G. Arnold, R.P. Hemmer, R.A. Huggins, *J. Power Sources.* 68 (1997) 582–585.
- [73] L. Guohua, H. Ikuta, T. Uchida, M. Wakihara, *J. Electrochem. Soc.* 143 (1996) 178.
- [74] D. Song, H. Ikuta, T. Uchida, M. Wakihara, *Solid State Ionics.* 117 (1999)

151–156.

- [75] X. Li, Y. Xu, C. Wang, *J. Alloys Compd.* 479 (2009) 310–313.
- [76] H. Zhao, F. Li, X. Liu, C. Cheng, Z. Zhang, Y. Wu, et al., *Electrochim. Acta.* 151 (2015) 263–269.
- [77] W. Wen, B. Ju, X. Wang, C. Wu, H. Shu, X. Yang, *Electrochim. Acta.* 147 (2014) 271–278.
- [78] T. Tsuji, M. Nagao, Y. Yamamura, N.T. Tai, *Solid State Ionics.* 154-155 (2002) 381–386.
- [79] Y. Ein-Eli, S.H. Lu, J.W.F. Howard, S. Mukerjee, J. McGreen, J.T. Vaughey, et al., *J. Electrochem. Soc.* 145 (1998) 1238–1244.
- [80] D. Capsoni, M. Bini, G. Chiodelli, P. Mustarelli, V. Massarotti, C.B. Azzoni, et al., *J. Phys. Chem. B.* 106 (2002) 7432–7438.
- [81] A. Veluchamy, H. Ikuta, M. Wakihara, *Solid State Ionics.* 143 (2001) 161–171.
- [82] S. Wang, J. Yang, X. Wu, Y. Li, Z. Gong, W. Wen, et al., *J. Power Sources.* 245 (2014) 570–578.
- [83] R. Chen, M. Knapp, M. Yavuz, R. Heinzmann, D. Wang, S. Ren, et al., *J. Phys. Chem. C.* 118 (2014) 12608–12616.
- [84] H. Sun, Y. Chen, C. Xu, D. Zhu, L. Huang, *J. Solid State Electrochem.* 16 (2012) 1247–1254.
- [85] S. Balaji, T. Manichandran, D. Mutharasu, *Bull. Mater. Sci.* 35 (2012) 471–480.
- [86] F. Le Cras, D. Bloch, M. Anne, P. Strobel, *Solid State Ionics.* 89 (1996) 203–213.
- [87] Y.-S. Lee, M. Yoshio, *Electrochem. Solid-State Lett.* 4 (2001) A85–A88.
- [88] Y.S. Lee, H. joo Lee, M. Yoshio, *Electrochem. Commun.* 165 (1996) 160–165.
- [89] G. Pistoia, G. Wang, C. Wang, *Solid State Ionics.* 58 (1992) 285–292.
- [90] W. Baochen, X. Yangyao, Z. Dongjiang, *J. Power Sources.* 43-44 (1993) 539–546.

- [91] Y.-K. Sun, Y.-S. Jeon, *Electrochem. Commun.* 1 (1999) 597–599.
- [92] Y.-K. Sun, Y.-S. Jeon, H.J. Lee, *Electrochem. Solid-State Lett.* 3 (1999) 7–9.
- [93] Y. Sun, I. Oh, *J. Power Sources.* 94 (2001) 132–136.
- [94] K. Amine, H. Tukamoto, H. Yasuda, Y. Fujita, *J. Power Sources.* 504 (1997) 604–608.
- [95] K. Amine, K. Amine, H. Tukamoto, H. Tukamoto, H. Yasuda, H. Yasuda, et al., *J. Electrochem. Soc.* 143 (1996) 1607–1613.
- [96] S.-H. Park, S.-W. Oh, C.-S. Yoon, S.-T. Myung, Y.-K. Sun, *Electrochem. Solid-State Lett.* 8 (2005) A163.
- [97] Y.K. Sun, S.W. Oh, C.S. Yoon, H.J. Bang, J. Prakash, *J. Power Sources.* 161 (2006) 19–26.
- [98] M.M. Thackeray, A. De Kock, M.H. Rossow, D. Liles, R. Bittihn, D. Hoge, *J. Electrochem. Soc.* 139 (1992) 363–366.
- [99] M.N. Richard, E.W. Fuller, J.R. Dahn, *Solid State Ionics.* 73 (1994) 81–91.
- [100] E. Ferg, R.J. Gummow, A. de Kock, M.M. Thackeray, *J. Electrochem. Soc.* 141 (1994) L147–L150.
- [101] a D. Robertson, a R. Armstrong, P.G. Bruce, *J. Power Sources.* 98 (2001) 332–335.
- [102] M.M. Thackeray, M.F. Mansuetto, D.W. Dees, D.R. Vissers, *Mater. Res. Bull.* 31 (1996) 133–140.
- [103] T. Takada, H. Hayakawa, T. Kumagai, E. Akiba, *J. Solid State Chem.* 121 (1996) 79–86.
- [104] T. Takada, H. Enoki, H. Hayakawa, E. Akiba, *J. Solid State Chem.* 139 (1998) 290–298.
- [105] T. Takada, H. Hayakawa, E. Akiba, F. Izumi, B.C. Chakoumakos, *J. Power Sources.* 68 (1997) 613–617.
- [106] T. Takada, H. Hayakawa, E. Akiba, *J. Solid State Chem.* 115 (1995) 420–426.
- [107] T. Takada, H. Hayakawa, H. Enoki, E. Akiba, H. Slegel, I. Davidson, et al., *J. Power Sources.* 81–82 (1999) 505–509.

- [108] W. Choi, a Manthiram, *Solid State Ionics*. 178 (2007) 1541–1545.
- [109] Y. Zhang, H. Wang, B. Wang, H. Yan, A. Ahniyaz, M. Yoshimura, *Mater. Res. Bull.* 37 (2002) 1411–1417.
- [110] Y.P. Jiang, J. Xie, G.S. Cao, X.B. Zhao, *Electrochim. Acta*. 56 (2010) 412–417.
- [111] Y.J. Hao, Y.Y. Wang, Q.Y. Lai, Y. Zhao, L.M. Chen, X.Y. Ji, *J. Solid State Electrochem.* 13 (2009) 905–912.
- [112] Y. Tian, D. Chen, X. Jiao, Y. Duan, *Chem. Commun. (Camb)*. (2007) 2072–2074.
- [113] C.M. Julien, M. Massot, K. Zaghib, *J. Power Sources*. 136 (2004) 72–79.
- [114] C.M. Julien, K. Zaghib, *Electrochim. Acta*. 50 (2004) 411–416.
- [115] M.L.P. Le, P. Strobel, C. V. Colin, T. Pagnier, F. Alloin, *J. Phys. Chem. Solids*. 72 (2011) 124–135.
- [116] Y. Li, Y. Makita, Z. Lin, S. Lin, N. Nagaoka, X. Yang, *Solid State Ionics*. 196 (2011) 34–40.
- [117] C.S. Johnson, N. Li, J.T. Vaughey, S. a. Hackney, M.M. Thackeray, *Electrochem. Commun.* 7 (2005) 528–536.
- [118] S. Ivanova, E. Zhecheva, D. Nihtianova, M. Mladenov, R. Stoyanova, *J. Alloys Compd.* 561 (2013) 252–261.
- [119] S. Ivanova, E. Zhecheva, D. Nihtianova, R. Stoyanova, *J. Mater. Sci.* 46 (2011) 7098–7105.

Chapter 3

Experimental Methodology

This chapter will enumerate the rationale behind selection of the various techniques employed for synthesizing and characterizing the desired materials. Structural and electrochemical characterization techniques will be discussed in detail.

3.1 Rationale for selection of methods/materials.

In this study, the effect of elemental substitutions on electrochemical performance and the effect of morphology are investigated. The synthesis techniques employed here were chosen based on the following considerations.

1. Homogenous mixing of precursors
2. Morphological control.
3. Possibility to scale up.
4. Access to equipment.

Keeping the above 4 considerations in mind, 3 different synthesis techniques were chosen namely solid state synthesis, co-precipitation synthesis and electrospinning synthesis. Co-precipitation technique (via hydroxide and carbonate) offer a very homogenous mixing of precursors on an atomic scale while offering the possibility of scaling up and offering morphological control as well. Electrospinning technique employed in this study also satisfies the above considerations. Although the setup employed does not offer scaling up, it has been demonstrated numerous times that it is possible to scale up electrospinning. The solid state technique does not offer the same homogeneity during precursor mixing like co-precipitation or electrospinning and cannot offer morphological control either. But it has the ability to be scaled up. The solid state technique is employed more as a baseline method to compare with other techniques since it is the standard method employed in the battery industry for synthesis of active materials.

The selection of characterization techniques were dictated by the type of information that is necessary to understand its performance. X-ray diffraction would be useful in determining the phase purity and extracting lattice parameter information while scanning electron microscopy would be suitable for evaluating the morphology and particle size. In electrochemical characterization, 3 major techniques were employed namely galvanostatic cycling, cyclic voltammetry and impedance spectroscopy.

The subsequent sections would discuss each of the synthesis and characterization techniques in detail.

3.2 Synthesis of active materials

The literature available on synthesis of electrode materials for lithium ion batteries is rather voluminous[1–11]. Here we discuss briefly three techniques which would be

employed in the current work namely – solid state synthesis, co-precipitation synthesis and single spinneret electrospinning synthesis. The advantages and disadvantages of each technique are also pointed out.

3.2.1 Solid state synthesis – Principles and analysis

Solid state or conventional synthesis involves mixing of precursors either simply by hand grinding in a pestle and mortar or in a more effective way via ball mills. The mixed precursors are then subjected to calcination at elevated temperatures followed by several re-annealing steps with intermediate grinding to form the desired final product. Typically for example to synthesise the spinel LiMn_2O_4 compound, one could start by mixing powdered oxides of Mn (e.g Mn_2O_3 , MnO_2 etc.) and hydroxide or carbonate of lithium ($\text{LiOH}/\text{Li}_2\text{CO}_3$). This mixture may be subjected to pelletizing in a pellet press to bring together the precursors so as to enable effective diffusion and homogenization of the components during calcination.

Usually hand grinding is not sufficient in all cases (and also not suitable for industrial scale production). Ball milling is generally required to intimately mix the precursors. Ball milling involves loading the precursors in a container (typically made of stainless steel or tungsten) together with small spherical balls of different diameters. This container assembly is then loaded in a ‘mill’ which agitates the container and supplies energy to the balls to move around very fast thereby colliding with each other. The powdered precursors are pulverized in these collisions between the balls leading to uniform mixing.

Solid state synthesis is a very simple method that allows preparation of large quantities of material in a single batch from cheap raw materials. It also offers easy scaling up to industrial levels. Minor batch to batch variations in raw materials can be handled easily in this method unlike other methods where starting material purity often has significant impact on the properties. However its limitation lies in the degree of mixing of the precursors. This creates a possibility of ending up with unreacted products if the temperature during calcination/annealing is not sufficient enough to activate diffusion processes which are necessary to obtain homogenous products. But in cases where the temperatures required for synthesis are high, this is a very effective technique to produce on a large scale economically. Solid state synthesis also does not offer morphological control and ability to synthesize nanoparticles with well-defined characteristics like other processes such as co-precipitation and electrospinning (both

discussed subsequently) for example. In the current work, solid state synthesis is employed to produce spinel LNM with irregular morphology.

In a typical synthesis, 25 mmol of anhydrous lithium acetate (99.95%, Sigma Aldrich), 12.5 mmol nickel nitrate hexahydrate (98 %, Alfa Aesar) and 37.5 mmol anhydrous manganese acetate (98%, Alfa Aesar) were weighed and subjected to ball milling. Acetone was employed as the milling medium. The milling speed was set to 300 rpm for 2 hours. The program was designed to include breaks of 10 minutes after 30 minutes of milling. Stainless steel balls of diameter 5mm were employed and a ball to powder ratio of 5:1 was used. The resulting paste from the ball milling was subjected to calcination at 900 °C for 5 hours followed by an annealing step at 700 °C for 24 hours in a box furnace (Carbolite, UK). The heating rate was fixed to 5 °C/min for both calcination and annealing steps and powders were naturally cooled inside the furnace to ambient conditions.

3.2.2 Co-precipitation synthesis – Principles and analysis

Co-precipitation synthesis [6,7,12] differs from the conventional synthesis in the way the precursors are mixed together. It was earlier mentioned that it was not possible to obtain atomic scale mixing of precursors with conventional precursor mixing (solid state synthesis). In order to obtain such uniformity, co-precipitation of precursors could be employed. This technique makes use of the difference in solubilities of compounds in solvents. Hydroxides and carbonates of certain elements are known to be generally insoluble in a variety of solvents including water. This fact is employed to precipitate out desired mixtures of compounds. A typical procedure involves dissolving metallic salts such as acetates/nitrates/sulphates of the desired elements (Ni/Mn) in water/ethanol and then adding a precipitating agent such as bicarbonate/hydroxide to precipitate out a very uniform mixture of these elements as the respective bicarbonates/hydroxides. Here it is evident that the starting precursors (i.e nitrates/acetates/sulphates are generally soluble in a variety of solvents) compared to the hydroxides. Hence as soon as the hydroxide/carbonate is added, the equilibrium is driven towards formation of the solid precipitate of the respective hydroxide or carbonate. Addition of lithium salt can be accomplished during the co-precipitation step itself or subsequently as a separate step as well.

It should be kept in mind that different variations of these techniques have since been employed. The main benefit arises from the initial step which involves dissolution of

the precursors. This ensures homogeneous distribution on an atomic scale of different elements. This homogenous mixture would then undergo precipitation simultaneously leading to the formation of a much more uniform mixture of precursors than can be obtained by ball milling/hand grinding. The co-precipitated mixture could subsequently be mixed with lithium salt and then subjected to calcination to obtain a much more pure product. The process also allows one to control the morphology/size of products through careful control of pH, temperature and proper combination of salts. This process also allows for upscaling to industrial levels without much hassle. The drawback however would be that the cost of metallic salts (e.g nitrates/acetates/sulphates) required might make it expensive compared to precursors used in conventional synthesis. Another drawback is the fabrication of well-defined nanostructured materials. The method involves calcination of the co-precipitated precursor at elevated temperature resulting in no control over the size of particles formed. While low temperatures can result in nanostructured particles, their morphology cannot be controlled. In this work, both hydroxide co-precipitation as well as carbonate co-precipitation are employed. The hydroxide method applied here offers atomic scale mixing of precursors while offering no morphological control. The main purpose is to synthesize pure phase compounds with substitutions. The carbonate method employed here however offers morphological control of the precursors. Spherical or cube shaped particles could be synthesized via the carbonate co-precipitation method as has been reported previously [7,12,13]. The main benefit of this technique is the possibility of fixing the particle size/morphology while varying the annealing conditions to obtain different degrees of crystallinity in the same material. This allows one to study the effect of crystallinity on performance while eliminating effects due to morphology and particle size on performance.

3.2.2.1 LiMn_2O_4 and $\text{LiNi}_{0.5}\text{Mn}_{1.5}\text{O}_4$ via hydroxide co-precipitation

Spinel LMO and LNM were synthesized via a hydroxide co-precipitation method followed by solid state firing. In a typical synthesis for the spinel LNM, 10 mmols of nickel nitrate hexahydrate (98 %, Sigma Aldrich) and 30 mmols of manganese nitrate solution (50 % by weight, Alfa Aesar) were dissolved in ethanol (95%). About 60 mmol of ammonium hydroxide solution (28%, Alfa Aesar) was added drop by drop to this mixture under vigorous stirring to obtain a uniform Ni-Mn coprecipitated hydroxide. Finally 20 mmol of lithium hydroxide monohydrate (98%, Alfa Aesar) was

added to the co-precipitated hydroxide solution. The resulting mixture was allowed to stir for 2 hours following which the mixed hydroxides were separated from the ethanol using a rotavapor system (Buchi). The mixed hydroxides so obtained were subjected to drying at 60 °C overnight followed by calcination at 500 °C for 3 hours to decomposed the volatiles. The resulting powders was further annealed at a range of temperatures from 500 – 800 °C for 10 hours to improve the crystallinity. The heating rate employed for the calcination and annealing steps were 5 °C/min and the powders were naturally cooled inside the furnace. All the calcination treatments were performed in a box furnace (Carbolite, UK). In case of spinel LMO, the exact same procedure as described above was followed except for the addition of nickel nitrate which is not required. Hence about 40 mmols of manganese nitrate solution was taken initially which was co-precipitated using 60 mmol of NH₄OH and 20 mmol of LiOH. All other conditions remain the same.

3.2.2.2 Li₄Ti_xMn_{5-x}O₁₂ (0 ≤ x ≤ 2) via hydroxide co-precipitation

A required amount of manganese nitrate solution (50 % by weight, Alfa Aesar) is dissolved in 70 ml of absolute ethanol (Merck KgA, Germany). Two drops of concentrated nitric acid (69%, Honeywell) were added to prevent hydrolysis of the titanium precursor. Next stoichiometric amount of tetraisopropylorthotitanate (96%, Tokyo Chemical Industry) is added to the mixture of manganese nitrate in ethanol. This is followed by a drop by drop addition of the required amount of ammonium hydroxide (28%, Alfa Aesar) to precipitate out the Mn-Ti hydroxide. After addition of the ammonia, the required amount of lithium hydroxide is added and the mixture is allowed to stir overnight. The mixed hydroxides are separated from the ethanol using a rotavapor system (Buchi, Switzerland). The separated hydroxides are then dried at 80 °C overnight before being calcined at temperatures in the range of 400 – 500 °C for 2 days under constant flow of oxygen in a horizontal flow tube furnace (Carbolite, UK).

3.2.2.3 LiNi_{0.5}Mn_{1.5}O₄ via carbonate co-precipitation

To prepare spinel LNM with a spherical morphology, carbonate co-precipitation technique was employed. It is a well-known method to prepare spherical/cubic shaped particles of different materials [14]. The procedure slightly modified from this reference involves 3 stage. In the first stage, 10 mmol of MnSO₄·H₂O (98%, Alfa Aesar) was dissolved in about 700 ml of DI water. Separately about 100 mmol of NH₄HCO₃ (98%, Alfa Aesar) was dissolved in 700 ml of DI water. Then the dissolved

NH_4HCO_3 solution is added to the stirring solution of MnSO_4 in DI water. Slowly a white precipitate of MnCO_3 forms that eventually fills the entire container. The solution is allowed to stir for 3 hours following which it is subjected to vacuum filtration with a glass microfiber filter paper (Whatmann) to separate the precipitate from the distillate. The collected precipitate is washed repeatedly with DI water and ethanol until the pH of the resulting filtrate is neutral (this would indicate all the excess NH_4HCO_3 has been removed). The MnCO_3 powder is subjected to drying overnight at 80 °C to eliminate moisture completely. The spherical morphology is established in this stage itself. The second stage involves conversion of the MnCO_3 powder to MnO_2 . This is achieved by calcination of the powder in a box furnace at 400 °C for 5 hours. This results in elimination of CO_2 leading to a porous morphology as well. The third stage involves mixing the MnO_2 with a lithium and nickel precursor followed by calcination. Here stoichiometric amounts of spherical MnO_2 , anhydrous lithium acetate (Sigma, 99.99%) and nickel nitrate hexahydrate (98%, Alfa Aesar) are suspended in 30 ml of ethanol. The lithium acetate and nickel nitrate dissolve instantly and infiltrate the pores of the spherical MnO_2 giving rise to a very homogeneously distributed precursor mix. This mixture is subsequently calcined in a box furnace at 500 °C for 3 hours (heating rate 5 °C/min followed by natural cooling) initially to drive off volatiles. The obtained powder is divided into batches and subjected to annealing at temperatures ranging from 500 °C to 800 °C for 10 hours to obtain the spherical spinel LNM samples.

3.2.3 Electrospinning – principles and analysis

Electrospinning is a well-known technique for the synthesis of one dimensional fibrous materials which are employed in a host of biological applications such as cardiovascular implants, drug delivery, wound dressing scaffolds and more [15]. It was initially discovered in 1934 and since then has evolved into an attractive technique for synthesis of 1D nanostructures for a variety of applications including energy storage and harvesting [16]. With the advent of nanotechnology in energy storage applications, electrospinning became a sought after technique to generate 1D materials with novel properties for energy storage applications [17–19]. The main benefit of this technique is the cost and ability to scale up relatively easily compared to other techniques for production of nanomaterials such as hydrothermal, electrodeposition or CVD/PVD techniques etc.

A schematic of the setup is shown in figure 3.1. The technique basically involves dissolving mixtures of salts such as acetates/acetylacetonates of Li/Ni/Mn/Co etc in a relatively volatile solvent such as ethanol/dimethylformamide/methanol together with a high molecular weight polymer such as polyethylene glycol/polyvinyl alcohol. This method of precursor preparation allows for control of solution viscosity which can in turn be used to modify the dimensions of the fibres produced.

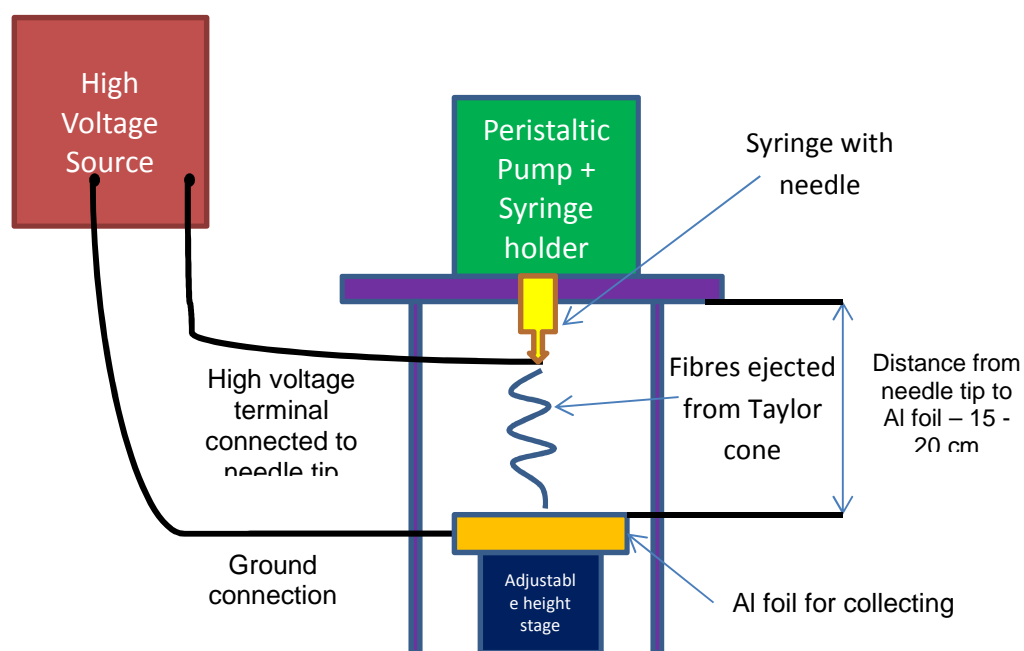


Figure 3.1 Schematic of electrospinning setup

The prepared precursor solution is then transferred into a syringe with a needle of specific dimensions and discharged at a controlled rate so as to form droplets at the tip of the needle. Simultaneously a high voltage of the order of 15 – 30 kV (typically) is applied to the needle. The electrostatic forces generated by the high voltage in the droplet cause it to shear into a ‘jet’ of liquid fibre (part of the Taylor cone). The volatile solvent evaporates instantly from this fibre jet causing the formation of a polymeric backbone that consists of homogeneously dispersed precursor salts. This polymer is collected on a substrate that is usually grounded such as an aluminium foil. This polymer backbone could be removed by calcining in a furnace resulting in the formation of a 1D structure consisting of nano-sized crystallites of oxides joined together. Figure 3.2 shows the process flow for generating 1D fibres consisting of oxide nanoparticles.

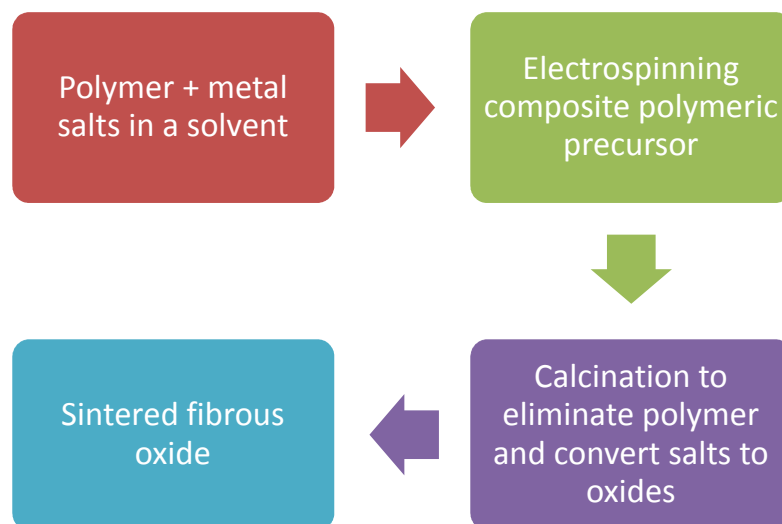


Figure 3.2 Process flow for synthesis of 1D nanofibrous oxides.

$\text{LiNi}_{0.5}\text{Mn}_{1.5}\text{O}_4$ was synthesized via a single spinnerette electrospinning technique. Briefly, 5 mM of anhydrous lithium acetate (99.95%, Sigma Aldrich), 2.5 mM of nickel nitrate hexahydrate (98%, Alfa Aesar) and 7.5 mM anhydrous manganese acetate (98%, Alfa Aesar) were dissolved in 30 ml of methanol (Fisher Scientific) and 1 ml of acetic acid (99.99%, Alfa Aesar) by stirring at 80 °C. Separately, about 2 g of polyvinylpyrrolidone of $M_w = 360,000$ g/mol (PVP, Fluka) was dissolved in approximately 10 ml of absolute ethanol (EMSURE, Merck). The solution of methanol containing the dissolved salts of lithium nickel and manganese was then added to the solution of PVP in ethanol under stirring. The resulting solution was stirred overnight at 80 °C to obtain a homogenous spinning solution. About 12 ml of this solution is then taken in a syringe with an 18G needle (inner diameter 0.838mm). This solution was then pumped out from the syringe at a constant rate of 0.8 ml per hour using a dosing pump (Kd Scientific). A high voltage generator (Gamma High Voltage Research DC Power supply) was employed to apply a positive voltage of 18 kV between the tip of the needle and a grounded aluminum foil which acted as a collector for the fibers. The distance between the tip of the needle and the current collector was maintained at 15cm. The humidity in the spinning chamber was maintained at 30% throughout the duration of the spinning process. The resulting fibers were then transferred to a box furnace maintained at 100 °C and then ramped up at a rate of 1 °C/min to 600 °C. The fibres were allowed to dwell for 1 hour at 600 °C before being ramped down to room temperature at 1 °C/min to obtain crystalline nanofibres of spinel LNM.

3.2.4 Comparison of synthesis techniques employed

Solid state method does not offer a lot of control with respect to nanostructuring or morphology. However on an industrial scale it is the most preferred method and easiest to implement. Pure raw materials such as lithium carbonate, manganese/nickel/cobalt oxides which come from the mines could be used without further purification/treatments to convert them to the desired electrode materials. In comparison electrospinning would require highly pure precursors which would be costly or require subsequent purification steps before usage. Table 3.1 presents a comparison of the conventional, co-precipitation and electrospinning techniques for synthesis

Table 3.1 Comparison of different synthesis techniques.

Characteristic	Solid state	Co-precipitation	Electrospinning
Final product purity	✓	✓	✓
Raw material quality variation	✓	✗	✗
Controlled nanostructuring	✗	✗	✓
Morphological control	✗	✓	✓
Process scale up	✓	✓	✓

3.3 Characterization

This section will describe the various physical, structural and electrochemical characterization techniques employed in this work.

3.3.1 Powder diffraction with X-rays – Principles and analysis

X-ray diffraction could be employed to obtain a wealth of information regarding the crystal structure of the compounds of interest. The technique was made possible by the fact that a crystal lattice acts as a diffraction grating that can diffract radiation which has a wavelength close to the size of the grating. It was found that x-rays which have wavelengths in the range of 0.1-10 nm were ideal for this purpose. The diffracted intensity and peak position depends on the nature and position of atoms within a crystal lattice thereby giving materials a method to ‘finger print’ materials. The

conditions necessary for diffraction is given by the Bragg's law which is stated as follows.

$$n\lambda = 2d\sin\theta \dots\dots\dots(1)$$

Where λ is the wavelength of radiation employed, d is the interplanar spacing between lattice planes and θ is the angle between the incident beam and the lattice plane. This law enables one to determine the interplanar spacing 'd' provided one knew the wavelength (λ) and diffraction angle (θ). In practise, a diffractometer is employed to perform this analysis on powder samples or thin films or other bulk samples. This instrument records diffracted intensities at different angles of the incident beam. This plot could then be analysed with the help of a database of such recorded patterns to obtain further information of purity, quantity of phases etc. Furthermore, the obtained pattern could be subjected to various fitting procedures using ideal patterns to generate the lattice parameters, crystallite size etc. One such technique is the Rietveld method which An appropriate starting point (i.e the ideal pattern) is required to perform this analysis. Various programs such as TOPAS, FULLPROF etc. are available that can provide one with the ability to perform Rietveld analysis of diffraction data. A good quality pattern (with sufficient signal to noise ratio) is mandatory for performing rietveld analysis.

Powder x-ray diffraction studies were carried out using either a Bruker D8 Advance diffractometer (Germany)\Rigaku Smartlab diffractometer (Japan) operating in a bragg-brentano geometry. Diffraction patterns were collected in the range of 10 - 90° using Bruker X-ray diffractometer, a step size of 0.02° coupled with a recording time of 1 s/step was used to obtain patterns. With the Rigaku instrument, since a higher power was employed the step size was 0.02° but the recording time was approximately 0.06 s/step. The recorded data were subjected to Rietveld refinement using a Topas V3/Rigaku lab software to obtain lattice parameters and quantify the amount of phases and impurities.

For diffraction studies of cycled electrodes, the electrodes are subjected to washing using DMC and drying under vacuum in a glovebox. They are subsequently transferred in a sealed container to the XRD equipment. XRD was performed directly on the electrode with the Al current collector attached. In cases where the main peaks belonging to the active material were pushed into the background due to the very high

intensity of the Al peak, the active material was scraped off from the aluminium current collector and loaded on to the sample holder.

3.3.2 Scanning electron microscopy – Principles and analysis.

Scanning electron microscopy as the name suggests involves the use of scanning a surface with electrons to perform microscopy. The technique employs a focussed primary electron beam which is scanned across a surface of interest. The interaction of this primary beam with the sample results in a host of different responses (emission of secondary electrons, scattering of electrons, emission of X-rays etc.) that emanate from different interaction regions on the surface of the specimen. Different detectors that are specially equipped to analyse each of these signals enable one to gather information about the sample. The signals emanating from each point scanned on the specimen are mapped directly onto a screen. Hence by controlling, the spot size, area scanned on the specimen and area of the screen, it is possible to obtain very high magnifications that are impossible to achieve in a light microscope.

Two major signals are employed in this work namely secondary electrons and x-rays emanating from the specimen. Secondary electrons are primarily conducting/valence band electrons that are not very tightly bound to the atom and hence can be knocked off easily. These secondary electrons can be gathered using a special detector that allows only low energy electrons to pass through. The collected electrons can be subsequently amplified to generate an image. The detection of secondary electrons is highly dependent on the nature of the surface and its topology. More secondary electrons are collected from ‘raised’ surfaces or edges compared to ‘lowered’ areas on the sample surface. This leads to a difference in brightness between a raised and lowered region on the surface thus providing the contrast necessary to distinguish two areas of a surface. By adjusting the probe size, the resolution can be further enhanced. However reducing the probe size also results in a reduction of the amount of signal generated and thus there is trade-off between resolution and contrast. X-rays on the other hand are generated due to K/L shell ionization. Electrons from the innermost shell (closest to the nucleus) are excited to a higher state momentarily by incoming electrons from the primary beam and fall back resulting in a emission of photons in the form of x-rays. The energy required to cause K/L shell ionization is unique for each element thus giving this method the ability to differentiate between elements present in the sample by analysing the energy of the emitted x-rays. The intensity of the x-rays

on the other hand is dependent on the number of atoms being excited. This can then provide a quantitative measure of the elements present.

Particle size, morphology, chemical compositions are some of the characteristics that can be investigated using the SEM. SEM offers very high resolution (compared to an optical microscope) and is hence suitable for studying surfaces in great detail. However there are some restrictions such as the requirement for high vacuum which is necessary to avoid interaction between the primary electron beam and the surrounding atmosphere. This makes it difficult or impossible to analyse volatile or liquid samples that give off vapours. Also the sample needs to be conducting in order to eliminate interference between the primary beam electrons and signals. This can however be accomplished using a conductive carbon/metallic coating on the surface. Finally it is not a bulk technique unlike x-ray diffraction which makes it not very representative unless a large number of runs are accumulated. However despite these limitations, it is still a useful technique for characterization.

Two different scanning electron microscopes were employed for morphological studies of the various materials. In cases where high resolution was not required, a JEOL 6360 SEM operating with a tungsten filament gun was employed. In cases where higher resolution was needed, a JEOL 7600 SEM equipped with a field emission gun was employed. In order to obtain good secondary electron images from non-conducting materials, a thin layer of gold was deposited on to the powders via a sputtering technique. Typically an operating voltage of 15 – 20 kV was employed to obtain high resolution images. For polymer containing samples, the voltage was reduced as required to avoid decomposition of the polymer under electron irradiation.

Energy dispersive analysis of x-rays was performed on the JEOL 6360 SEM. An operating voltage about twice that of the K shell electron excitation was applied. Typically these values are around 20 – 25 kV for nickel, manganese and titanium. The spot size was adjusted to give counts per second (CPS) value of 2000 and it was ensured that the scanned area was maintained similar across different samples.

3.3.3 Transmission electron microscopy – Principles and analysis

Transmission electron microscopy can be considered similar to a transmission optical light microscope except that instead of light, a beam of electrons is employed to

analyse the specimen. One can consider this as attempting to ‘shine’ electrons through a specimen and then collecting the electrons that pass through on a screen to generate an image. The basic requirement for this technique hence is that the sample should be ‘electron transparent’. Although this places some limitations on the samples for analysis, it can be a very powerful tool to gather data about the specimen. The TEM can be operated in two modes – namely imaging and diffraction mode. In imaging, the microscope works like a light microscope and the electrons passing through a specimen can be collected on a fluorescent screen/charge coupled device detector. Areas which have lesser electron penetration would appear dark while areas that have higher electron penetration would appear bright. This difference would be the source of contrast for images. Again since electrons are employed, the resolution obtainable can be very high (resolution is directly proportional to wavelength of light used, hence lower the wavelength lower the resolution or higher the resolving power). TEM can routinely offer imaging in the range of few nanometers to angstroms. The second mode namely the diffraction mode is a very powerful mode that can offer insights into the local crystal structure of the specimen. A focussed electron beam is allowed to pass through the specimen and the resulting diffracted beams are collected on a fluorescent screen/charge couple device detector. From the patterns, one can obtain useful information about the interplanar spacing and different diffracting planes. Energy dispersive analysis of X-rays could also be performed using a sensitive x-ray detector setup attached to the TEM. By performing fourier transforms of the electron diffraction patterns, one could even distinguish atomic positions in a lattice. All these capabilities make the TEM a very powerful analytical technique for material characterization. In this work TEM is primarily employed to study nanofibers fabricated via electrospinning technique.

Transmission electron microscopy was performed using a JEOL 2100F TEM (Japan) operating at 200 KeV beam energy. The materials for analysis were dispersed in ethanol using mild sonication and a drop of this solution was dropped on to a carbon-copper microgrid. The ethanol was evaporated away to leave behind particles on the grid which could be observed under the TEM. Select Area Diffraction patterns were recorded to determine the interplanar spacing in the different crystallites.

3.3.4 Thermal analysis techniques – principles and analysis

Thermal analysis involves the study of materials which are subjected to heating or cooling. There are many techniques for thermal analysis. In this work, we use 2 main methods namely Thermogravimetric analysis and Differential Scanning Calorimetry. Thermogravimetric analysis is a useful technique for identifying physical and chemical properties of samples. The technique involves heating a sample in a specific atmosphere of flowing gases (argon/oxygen/nitrogen etc) at a constant rate and measuring the mass changes occurring in the sample with the help of a very sensitive balance. Alternatively, one can also hold a sample at a specific temperature and study how the mass varies with time. If a sample undergoes decomposition leading to mass losses, it can be detected accurately via this technique. There are many applications for such a method. For example, it can be applied to determine the conditions at which certain reactions proceed to complete thus enabling one to fix calcination conditions based on this. Thermal stability of materials to temperature can also be determined. If a material loses no mass on heating, then it indirectly indicates that the material is not dissociating on being subject to heating. Differential scanning calorimetry is another powerful technique that can be employed as a complementary technique to TGA. In DSC, the heat flow to a sample is measured with respect to a reference that is maintained at about the same temperature as the sample. If the sample undergoes an exothermic/endothermic reaction, there will be heat flowing out/into the sample while the reference would not display such heat flow. This enables one to determine heat flows occurring at different temperatures for samples under consideration. Combined with TGA, this technique can throw significant light on a lot of processes. For example, during combustion of a polymeric or carbon precursor, one can observe significant mass loss occurring together with a positive heat flow occurring from the sample. The positive heat flow is what one would expect from an exothermic reaction while mass loss is occurring due to the formation of gases such as CO and CO₂. Similarly during removal of water, heat would be absorbed by the sample while there would be a mass loss observed by the TGA. This is expected as removal of water requires heating as and it results in weight reduction to the water vapour escaping out from the sample.

In this work, TGA-DSC is employed to determine the stability of samples, calcination conditions, amount of water present in the samples/residual carbon content after

calcination. The samples are loaded in to aluminium/aluminium oxide crucibles depending on the maximum temperature reached during the analysis (900 °C). Typically the samples are ramped up at a rate of 10 °C/min. Depending on the requirement, high purity argon or oxygen was employed as the analysis gas.

3.3.5 Fourier Transform Infrared spectroscopy – Principles and analysis

Infrared spectroscopy is a valuable technique that helps in analysing and characterizing compounds by virtue of their molecular structure. Molecular bonds are known to display different types of movements ranging from vibration to stretching or rocking, twisting etc. If the associated movement creates a dipole (or if the dipole is a permanent one as well), then it is possible that this dipole can interact with the incident infrared beam at certain frequencies absorbing the infrared light. Each bond can absorb a specific level of infrared energy that gives it a signature pattern that depends on the frequency of the vibration (absorption occurs at resonance condition i.e when the frequency of the incident beam matches the frequency of vibration). For example, the O-H bond stretching movement typically absorbs infrared energy corresponding to a wavenumber of around 3000 - 3500 cm^{-1} . Thus if a compound containing an O-H bond is present, it can be easily identified using infrared spectroscopy using this signature peak. The number of modes that are ‘infrared active’ would basically depend on the nature of atoms forming the molecule, its surroundings etc. For example, homogenous diatomic molecules such as O_2 , Cl_2 etc cannot generate a dipole moment and hence cannot be identified via infrared spectroscopy. Similarly, in oxide compounds, the nature of bonding and surroundings display ‘fingerprint’ infrared spectra that can be used to distinguish them. Typically, infrared spectrum is divided into 3 regions namely – the mid IR region (4000 – 400 cm^{-1}), the far IR region (700 – 30 cm^{-1}) and the near IR region (14000 – 4000 cm^{-1}). Different functional groups require excitation with different levels of energy. Depending on the requirement, one needs to select the appropriate range for analysis. The result of an analysis is usually displayed as a transmittance versus wavenumber plot in this analysis. By analysing the peak position and intensity, it is possible to identify the functional groups present in a sample. The equipment employed for obtaining the spectra is known as an Infrared spectrometer. A limitation with the infrared spectrometer is that it can scan only one wavelength/frequency at a time. Since recording spectra requires that a wide range of frequencies be scanned, it would take too much time to analyse a single sample. This

was overcome by employing the interferometer which basically is a device that produces a signal that contains all frequencies encoded in it. Now when this signal is allowed to analyse a sample, the resulting signal would contain information pertaining to the original signal minus the frequencies absorbed by the sample. This signal can then be deconvoluted back to obtain frequency information using a Fourier Transform function. This is now known as Fourier Transform Infrared Spectroscopy. FTIR allows analysis of a wide variety of samples (liquids, solids or gases) by employing different modes (transmission, reflection etc.).

In this study, FTIR would be employed to ascertain the nature of space group present in the different spinel LNM samples synthesized. Spinel LNM crystallizes in two different structures depending on the ordering of the nickel and manganese ions in the lattice. These two structures have different symmetry groups/space groups namely – $P4_332$ and $Fd\bar{3}m$. Since the symmetry is different for these two structures, there will be discrete vibrations occurring in one which will not be present in the other. This difference can be detected easily by FTIR spectroscopy.

A Perkin Elmer Frontier Infrared spectrometer is employed to obtain the infrared spectra in the frequency range $4000 - 400 \text{ cm}^{-1}$. The solid samples were prepared by mixing together with FTIR Grade KBr (Merck) and subjected to pelletizing to obtain a thin translucent sample. About 0.25 mg of sample was dispersed in 100 mg of KBr powder. The pelletization was performed using a load of 10 tons for 1 minute. Blank pellets with only the KBr powder were employed to obtain backgrounds which were subtracted from the resulting spectra. An average of 16 scans was collected for each sample to eliminate disturbances due to equipment.

3.3.6 Electrode preparation and cell assembly – Principles and analysis

In order to perform electrochemical studies on the active material, it is necessary to mix it with a conductive additive and binder to fabricate it into the form of an electrode that can be handled easily. The conductive additive (mostly acetylene black or a conducting carbon) provides the path for transport of electrons into and out of the active material. The binder on the other hand holds together the carbon and active material thus providing a stable electrode. The binder also helps bind the mixture of active material and carbon to the current collectors (aluminium or copper). Typically one could mix these materials using a pestle and mortar and form slurry that can be

coated directly on a current collector. However the dispersion of the components might not be very good. To ensure a very homogenous dispersion, these components could be subjected to stirring for long times. The amount of NMP added can affect the viscosity of the slurry which in turn can directly affect the thickness of the coating and the mass loading of the electrode. Similarly the thickness of the doctor blade used for coating the slurry would directly determine the mass loading as well with bigger gaps giving a higher mass loading. The energy storage community employs a wide variety of techniques and devices for preparing the electrodes. In this study, the method and equipment used is basically restricted by the availability in the labs. However effort was taken to come up with a reproducible procedure for electrode preparation.

Cell assembly is an important procedural step that affects results significantly. Different configurations of cells are possible depending on the requirement. Typically, a 3 – electrode system should be employed to conduct electrochemical studies. The 3-electrode system as the name suggests consists of 3 electrodes. One is the working electrode which consists of the mixture of the material to be investigated, the second is a counter electrode which is necessary for completion of the electrical circuit with the working electrode. The 3rd electrode is a reference electrode which is used to accurately determine the potential of the working electrode. The main benefit of the 3-electrode system is that there is no current passed through the reference electrode. This allows for a much more stable reference potential which can in turn give more accurate potentials at the working electrode. Different formats including Swagelok type cells, pouch cells can be used to assemble 3-electrode systems. Another configuration for electrochemical testing is the 2-electrode system. They are employed where a single electrode functions as both the reference as well as counter electrode apart from the working electrode. In this case it is necessary to know that the reference potential does not vary that much due to changes occurring when it carries current. For testing of lithium based energy devices, the 2-electrode configuration is accepted widely as the testing configuration. It is cheap and easy to assemble and use 2-electrode cells. The most common 2-electrode configuration encountered is a coin cell. One can come across such cells in watches, calculators etc. (albeit with a different chemistry). Coin cells come in various formats such as CR2016, CR2032, CR2322 etc. The differences primarily are in the diameter and maximum thickness of the cells. A CR 2016 cell has a diameter of 20 mm with a thickness of 1.6mm while a CR 2032

cell has the same diameter but thicker at 3.2mm. In a typical setup employed for testing lithium ion based devices, lithium metal is employed as the reference counter electrode. This will ensure a virtually unlimited supply of lithium ions for electrochemical reactions at the working electrode and thus provide a stable potential throughout measurements. But this also poses a limitation in handling since lithium is highly reactive and can form LiOH / Li_2O / Li_3N on reacting with ambient atmosphere. To prevent this reaction, the entire assembly must be conducted in an inert atmosphere. A glovebox is employed for this purpose. A glovebox consists of an atmosphere that is made up of an inert gas (argon/nitrogen) and this atmosphere is continuously circulated through a purifying unit that consists of special materials that have the ability to remove oxygen and moisture. Typical oxygen and moisture contents in a glovebox are <1 ppm. The glovebox is also beneficial for handling reactive electrolytes such as LiPF_6 containing electrolytes (PF_6^- ion can react with moisture to form HF and PF_5^-).

The active materials employed in this work were fabricated into working electrodes for electrochemical characterization via a standardized slurry coating procedure. Unless otherwise stated, a composition of 75 % active material, 15 % conductive agent and 10 % binder was employed for all materials investigated in this work. The conductive agent was acetylene black (50 % compressed, Alfa Aesar) while the binder was a solution containing 6 wt % polyvinylidene di fluoride (HSV 900 Kynar) in *n*-methylpyrrolidone (98 %, Alfa Aesar). The acetylene black had a BET surface area of $75 \text{ m}^2/\text{g}$. The procedure for the slurry preparation consisted of the following steps. First the acetylene black and active material were weighed in the required proportions and ground in the pestle and mortar. To this mixture, the required amount of binder solution was added. The resulting paste was further diluted with a fixed amount of NMP to form homogeneous slurry. The slurry was stirred overnight keeping in line with standard industry practice. In a typical preparation, 0.200 g of active material, 0.040 g of acetylene black and 0.444 g of binder solution would be mixed in 0.7 – 0.9 ml of NMP. The amount of NMP was adjusted based on the nature of materials tested as well. For e.g., nanomaterials required more NMP compared to conventional micron sized materials for the same mass loading.

The homogenous slurry was then coated onto the rough side of aluminium foil (Goodfellow, 15μ thickness, battery grade) which acts as the current collector using a

slurry coating machine (Coatmaster, ERICHSEN) and doctor blades. The gap on the doctor blades ranged from 50 – 300 μm in order to facilitate obtaining electrodes with different mass loadings. Typically a 100 μm gap doctor blade results in electrodes with an active material loading of 3.5 – 4 mg (on a 16 mm diameter Al foil punched from the bigger sheet) whereas a gap of 200 μm results in an active material loading of roughly 6.5 – 7.5 mg.

After coating, the sheets are transferred to a hot plate maintained at 80 $^{\circ}\text{C}$ in order to remove the NMP solvent from the electrodes. Once the electrode sheets become visually dry, they are transferred into an oven maintained at 120 $^{\circ}\text{C}$ and allowed to dry for 4 hours before being taken for further processing. This was necessary in order to prevent delamination during electrode punching.

The dried electrode sheet is then subjected to roll pressing to improve electrical contact within the electrode. The dried electrode sheet is placed in between stainless steel plates 100 μm thick and the assembly is fed between the rolls of a roll press (MTI Corp). The gap between the rolls is set to 200 μm during the first pass and then reduced to 50 μm for the second pass. Each time the electrode sheet direction is turned by 180 $^{\circ}$ to achieve uniform compaction across the electrode width.

After roll pressing, the electrode sheets are subjected to punching to generate 16 mm diameter disks which would fit into CR 2016 coin cells. The punched electrodes are weighed to calculate the active mass loading on each electrode and then subjected to drying under vacuum at 110 $^{\circ}\text{C}$ in order to completely eliminate moisture and leftover NMP. The drying is performed in a specially designed tubes and oven (Buchi, Switzerland) which enables transport of the electrodes under vacuum into the glovebox.

Electrochemical characterization for systems employing non-aqueous electrolytes was performed by assembling coin cells (2-electrode configuration) of the working electrode and a lithium metal foil counter electrode. The thickness of the lithium metal foil was about 0.25 mm. The lithium metal acts as both the reference and counter electrode in the assembly. The exploded view of the coin cell assembly is presented in figure.

All coin cells were assembled in inert atmosphere gloveboxes (MBraun, Germany and Vacuum Atmospheres Company, USA) to avoid electrolyte and lithium metal

contamination. The oxygen and moisture levels were maintained at <0.1 ppm in the MBraun box and <1 ppm in the Vacuum atmospheres box. Standard battery grade electrolytes manufactured by established suppliers were employed for the electrochemical characterization. A typical formulation consists of 1M LiPF_6 in a 1:1 mixture of ethylene carbonate and diethyl carbonate by volume. The electrolytes employed were obtained from various suppliers (Sigma Aldrich, Tomiyama, Charlston Technologies) throughout the course of this work. However Karl Fischer titration results revealed that all the electrolytes employed had <10 ppm of moisture content. Hence the variation in supplier is not expected to cause a significant deviation in results.

A wide variety of electrochemical characterization techniques were employed in this study. The purposes of those tests together with the equipments employed for each of them are briefly discussed in the subsequent sections.

3.3.7 Cyclic voltammetry – principles and analysis

Cyclic Voltammetry (CV) involves subjecting the potential of the working electrode to small increments of voltage and recording the current response of the electrode. The output is a plot of current vs voltage. This technique is useful in identifying the potentials at which the main redox reaction(s) occur (indicated by the presence of peaks in currents at distinct potentials) and the presence of side reactions in the system as well. CV also helps in estimating the reversibility and capacity fading (if any) of the material under consideration. The technique can also give us information about the kinetics of processes occurring in the system and the presence of unwanted side reactions in the system. To obtain accurate data, it is best to perform CV at the slowest rate of scan possible. This will give rise to well defined peaks in the plots. Typically, CV studies in this work were performed at a slow rate of 0.1-0.2 mV/s for organic electrolytes. To determine if the performance of a system is limited by diffusion, CV is performed at different rates and plots of peak current versus square root of scan rate are employed. A linear relationship in this plot would indicate diffusion controlled processes are occurring in the system. All CV measurements were performed either using Solartron 1260 (UK) or Biologic VMP3 (France) instruments.

3.3.8 Galvanostatic cycling – principles and analysis

In order to obtain the specific capacity of a material, galvanostatic charge discharge measurements can be employed. This technique involves the application of a constant current to the working electrode and monitoring the voltage evolution of that electrode with respect to the reference electrode. A typical output would be in the form of a voltage versus time/capacity plot which enables one to determine capacities of active materials and make estimates of cell level energy density/power density. This technique is also essential in determining the coulombic efficiency of the systems. For example, if there is any electrolyte decomposition occurring, this would show up as a difference between the charge and discharge capacities. The experiments are ideally performed at different C-rates which indicate the rate at which electrons are withdrawn or supplied to the working electrode. The C-rate is decided based on the theoretical capacity and aim of the test. Typically, a 1C rate indicates a complete charge or discharge cycle that occurs in one hour. C/2 rate on the other hand refers to a full cycle of charge/discharge that takes about 2 hours to complete. C-rate are also often quoted in mA/g. This basically can be calculated from the theoretical capacity of the material. For example, spinel LiMn_2O_4 has a theoretical capacity of 146 mAh.g^{-1} . If a current rate of 50 mA.g^{-1} is employed to charge it, then it would take roughly 2.92 hours to complete the charge. This indicates a C-rate of roughly C/3. In the present study galvanostatic cycling was performed on Neware BTS battery cyclers with the capability to employ currents as low as $10 \mu\text{A}$ and as high as 10 mA . For currents beyond 10 mA , Arbin BT2000 battery testers were employed which have the capability to apply currents as high as 1 A . Normally 3 coin cells are prepared for each material to ensure reproducibility. The error observed was about $\pm 5 \text{ mAh.g}^{-1}$.

3.3.9 Electrochemical impedance spectroscopy – principles and analysis.

Impedance spectroscopy is a powerful technique that can be used to study a variety of processes occurring on a microscopic level in the active material. It involves the application of a small amplitude alternating current perturbation to a steady state system and observing the current response of the system. The process is repeated at different frequencies in order to obtain the response of different processes that occur on different timescales. For example, diffusion inside solids which is a slow process is visible at very low frequencies while non-faradaic processes such as double layer formation can occur at very high frequencies. Charge transfer processes occur at

frequencies that are in between diffusion and double layer formation. The impedance measurements could be made at different states of charge as well to monitor how certain processes/parameters vary with state of charge. For example, surface film formation is greatly affected by the voltage of the working electrode. This can be easily determined from impedance studies. The data obtained from the impedance analysis is usually plotted in the form a Nyquist plot or Bode plot. A Nyquist plot gives the variation of 2 components of impedance namely the real and imaginary plots at different frequencies. A Bode plot on the other hand would plot the phase shift as a function of frequency. Data from impedance analysis can then be subjected to fitting using equivalent circuits that serve to model different processes occurring in the system. For example, formation of an electrical double layer and transport of charges across this double layer can be modelled using a parallel R-C circuit. From the fitting, one can determine the resistance and double layer capacitance for various processes. Impedance measurements can be performed on 2-electrode coin cells or 3- electrode cells. However care must be taken while assembling the cells since even a slight misalignment in the electrodes can affect reproducibility between the cells.

In this study, impedance is employed to determine the charge transfer resistance and resistance due to surface films that form during charging/discharging on the working electrodes. Impedance measurements are performed on 2 electrode coin cells with the assumption that the changes occurring at the counter electrode are similar and that the changes occurring can be attributed to the working electrode. Impedance measurements were performed before and after cycling as well as at different states of charge as per requirements. All impedance measurements were performed on a Biologic VMP3 instrument (France) which has a frequency response analyser coupled to the channels.

3.4 Overview of methodologies

To sum up, a host of experimental methodologies have been employed in this work. For physical and structural characterization, the main aim was to characterize the phase purity, lattice parameters, morphology and particle size. Hence x-ray diffraction, scanning electron microscopy and transmission electron microscopy were the main methods which were employed. Thermogravimetric analysis and differential scanning

calorimetry were also employed to identify optimum conditions for calcination and residual carbon content after calcination.

The experimental methodology involves synthesis followed by physical and structural characterization. Once the purity of the phase and other requisite factors such as morphology were achieved, electrochemical characterization was performed for the material. In the synthesis step, attempts were made to fabricate large batches of samples to minimize batch to batch variations. For example, in co-precipitation synthesis, a single batch of roughly 6 grams is calcined at 500 °C for 3 hours. This batch is then divided into 5 equal portions for further annealing at different temperatures. In this way, the variation between samples is kept to a minimum as they are processed from the same master batch. In cases where it was not possible to synthesize large batches, multiple batches were produced and later on mixed to obtain a large batch which was then subjected to characterization. For example in electrospinning, there was a limitation in the quantity of material that could be synthesized owing to the nature of the technique and requirement for immediate calcination. In this case, multiple batches of electrospun and calcined samples were mixed together to obtain a large batch that was analysed.

References

- [1] J. Chen , *Recent Pat. Nanotechnol.* **2012**, 7 1–12.
- [2] J. Chen, S. Wang, M.S. Whittingham, *J. Power Sources.* **2007**, 174, 442–448.
- [3] S. Balaji, D. Mutharasu, N.S. Subramanian, K. Ramanathan, *Ionics.* **2009**, 15, 765–777.
- [4] J.M. Tarascon, N. Recham, M. Armand, J.N. Chotard, P. Barpanda, W. Walker, et al., *Chem. Mater.* **2010**, 22, 724–739.
- [5] X.Y. Feng, C. Shen, X. Fang, C.H. Chen, *J. Alloys & Compd.* **2011**, 509, 3623–3626.
- [6] J.H. Lim, H. Bang, K.S. Lee, K. Amine, Y.K. Sun, *J. Power Sources.* **2009**, 189, 571–575.
- [7] A. van Bommel, J.R. Dahn, *J. Electrochem. Soc.* **2009**, 156, A362.
- [8] V. Aravindan, J. Sundaramurthy, P. Suresh Kumar, Y.-S. Lee, S. Ramakrishna, S. Madhavi, *Chem. Commun.* **2015**, 51, 2225–2234.

- [9] Y. Tanaka, Q. Zhang, F. Saito, *Powder Technol.* **2003**, 132, 74–80.
- [10] S.H. Park, S.T. Myung, S.W. Oh, C.S. Yoon, Y.K. Sun, *Electrochim. Acta.* **2006**, 51, 4089–4095.
- [11] S.-H. Kang, J.B. Goodenough, *Electrochem. Solid-State Lett.* **1999**, 3, 536.
- [12] S.H. Park, S.H. Kang, I. Belharouak, Y.K. Sun, K. Amine, *J. Power Sources.* **2008**, 177, 177–183.
- [13] Y. Fu, H. Jiang, Y. Hu, L. Zhang, C. Li, *J. Power Sources.* **2014**, 261, 306–310.
- [14] L. Zhou, D. Zhao, X. Lou, *Angew. Chem. Int. Ed. Engl.* **2012**, 51, 239–41.
- [15] R. Sridhar, R. Lakshminarayanan, K. Madhaiyan, V. Amutha Barathi, K.H.C. Lim, S. Ramakrishna, *Chem. Soc. Rev.* **2015**, 44, 790–814.
- [16] P.S. Kumar, J. Sundaramurthy, S. Sundarajan, V.J. Babu, G. Singh, S.I. Allakhverdiev, et al., *Energy Environ. Sci.* **2014**, 7, 3192–3222.
- [17] S. Kalluri, K.H. Seng, Z. Guo, H.K. Liu, S.X. Dou, *RSC Adv.* **2013**, 3, 25576 - 25601.
- [18] X. Zhang, L. Ji, O. Toprakci, Y. Liang, M. Alcoutlabi, *Polym. Rev.* **2011**, 51, 239–264.
- [19] S. Cavaliere, S. Subianto, I. Savych, D.J. Jones, J. Rozière, *Energy Environ. Sci.* **2011**, 4, 4761

Chapter 4

Effect of elemental substitutions on performance

This chapter presents the results of elemental substitutions on electrochemical performance for spinel LiMn_2O_4 (substituted with Ni) and $\text{Li}_4\text{Mn}_5\text{O}_{12}$ (substituted with Ti) synthesised via hydroxide co-precipitation method. Results of physical and structural characterization followed by galvanostatic characterisation and ex-situ studies are presented. Finally the major observations are summed up.

4.1 Introduction

The first major objective of this work is to identify and systematically study the effect of nickel substitution for manganese in LiMn_2O_4 and titanium substitution for manganese in $\text{Li}_4\text{Mn}_5\text{O}_{12}$. To facilitate this study, samples were synthesized via hydroxide co-precipitation method. Detailed structural and electrochemical characterization results are presented in the subsequent sections. First the effect of nickel substitution will be analysed. This will be followed by studies of the effect of titanium substitution.

To prepare the nickel substituted spinels, the precursors obtained from co-precipitation were subjected to calcination at several temperatures ranging from 500 – 800 °C for 10 hours after an initial calcination step at 500 °C for 3 hours.

Synthesis of the excess spinel $\text{Li}_4\text{Mn}_5\text{O}_{12}$ is typically performed at around 400 – 500 °C. Higher temperatures are known to cause decomposition to other mixed spinel phases. The atmosphere can also have a significant effect on the final phase purity [1–3]. It was well known that a temperature of 400 °C was insufficient for enabling diffusion processes that would ultimately result in a pure phase material while a temperature of 500 °C while enabling diffusion processes would result in decomposition of the spinel phase formed. However these problems could be overcome by performing the annealing in an oxygen rich atmosphere. Hence in this study, two temperatures – 400 °C and 500 °C were investigated with the synthesis time set to 2 days. It is worth noting that Manthiram et.al. [1] employed similar conditions to prepare their samples as well although their annealing was performed under ambient atmospheres rather than oxygen. Nevertheless, the use of oxygen in our case should be able to avoid disproportionation completely should it occur. To prepare the titanium substituted spinel, precursors obtained from calcination were subjected to calcination at 400/500/600 °C. It will be shown that calcination performed in oxygen is more effective in producing pure phase spinel.

For ease of usage, samples are identified using a labelling system. For nickel substitution in LiMn_2O_4 , the labels include the type of material (LMO/LNM), the temperature and time of annealing. For e.g, a spinel LMO calcined at 500 °C for 3 hours will be labelled as LMO_500_3h. For Ti substitution in $\text{Li}_4\text{Mn}_5\text{O}_{12}$, the samples prepared are labelled $\text{Ti}_{0.1/0.5/1/2}$ along with the temperature of calcination, time and atmosphere used. $0.1/0.5/1/2$ represents the mols of the Ti substituted for

manganese. Atmosphere refers to the environment employed during annealing (oxygen or ambient atmospheres). For example, Ti0_400_2d_O₂ represents a spinel with no Ti annealed for 2 days in an atmosphere of O₂ at 400 °C. For the sake of convenience, samples annealed at a specific temperature will be identified using the Ti content alone (Ti0, Ti0.1 etc).

4.2 Experimental Methods – nickel substitution in LiMn₂O₄.

4.2.1 Powder X-ray diffraction

The results of powder diffraction for the spinel LMO\LNM are presented in figure 4.1 (a & b).

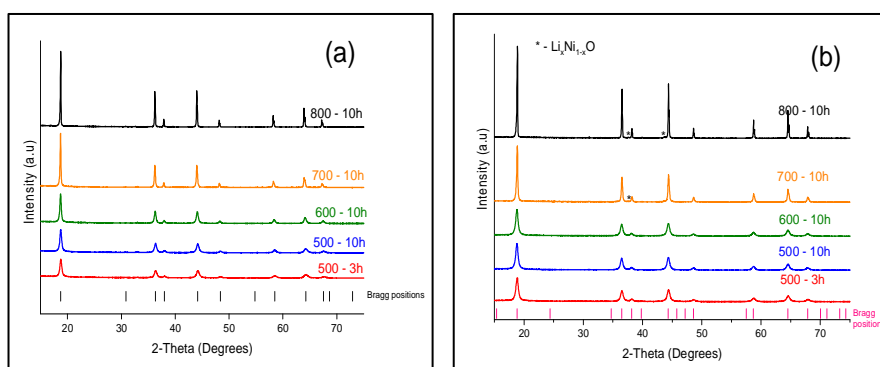


Figure 4.1 XRD patterns of (a) spinel LMO (b) spinel LNM at different synthesis temperatures.

The XRD patterns observed for the LNM samples could be indexed to a cubic spinel structure with $Fd\bar{3}m$ space group (ICSD Coll code: 90650) while those of the LMO samples could be indexed to the cubic spinel structure with $Fd3m$ space group (ICSD Coll code: 88644). A minor impurity phase belonging to a rock-salt type phase $\text{Li}_x\text{Ni}_{1-x}\text{O}$ ($Fm3m$ space group, ICSD Coll code: 71422) was observed to be present for LNM_700_10h and LNM_800_10h samples.

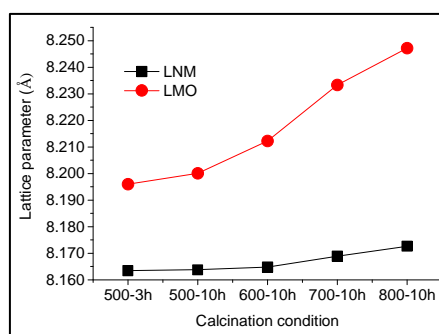


Figure 4.2 Variation of lattice parameter with calcination condition

Table 4.1 Refinement results for LNM and LMO

Sample	Lattice constant , a (Å)	R _p (%)	R _{wp} (%)	GOF
LNM - 500 – 3h	8.1635 (12)	2.6	3.2	1.1
LNM – 500 – 10h	8.1638(11)	2.5	3.1	1.1
LNM – 600 – 10h	8.1648 (7)	2.1	2.7	1.7
LNM – 700 – 10h	8.1689(3)	2.8	3.7	1.5
LNM – 800 – 10h	8.17275(17)	3.3	4.4	2.2
LMO – 500 – 3h	8.196(12)	5.4	4.2	1.3
LMO – 500 – 10h	8.2001(12)	5.8	4.3	1.6
LMO – 600 – 10h	8.2122(9)	5.6	4.2	1.5
LMO – 700 – 10h	8.2333(4)	5.9	4.5	1.7
LMO – 800 – 10h	8.2472(9)	7.2	5.6	2.3

The lattice parameters (together with the uncertainty in the last digit calculated by the program) obtained from refinements is given in table 4.1 and the variation in lattice parameters with temperature is presented in figure 4.2. It is easy to see that the lattice parameters for LNM samples are reduced compared to the LMO samples reflecting the fact that the larger Mn^{3+} ions in LMO are now replaced with smaller Mn^{4+} ions in LNM. This indicates that nickel has been successfully incorporated into the lattice of LMO. The lattice parameters are in good agreement with reported literature values [4]. It should be noted however that XRD cannot conclusively identify the space group since it would be very difficult to observe superstructure reflections corresponding to the $P4_332$ space group in XRD unless very high intensity beams with long scanning times are employed. The difference in space groups can be more clearly understood from other techniques such as Fourier Transform Infrared spectroscopy which will be described subsequently.

4.2.2 Scanning electron microscopy

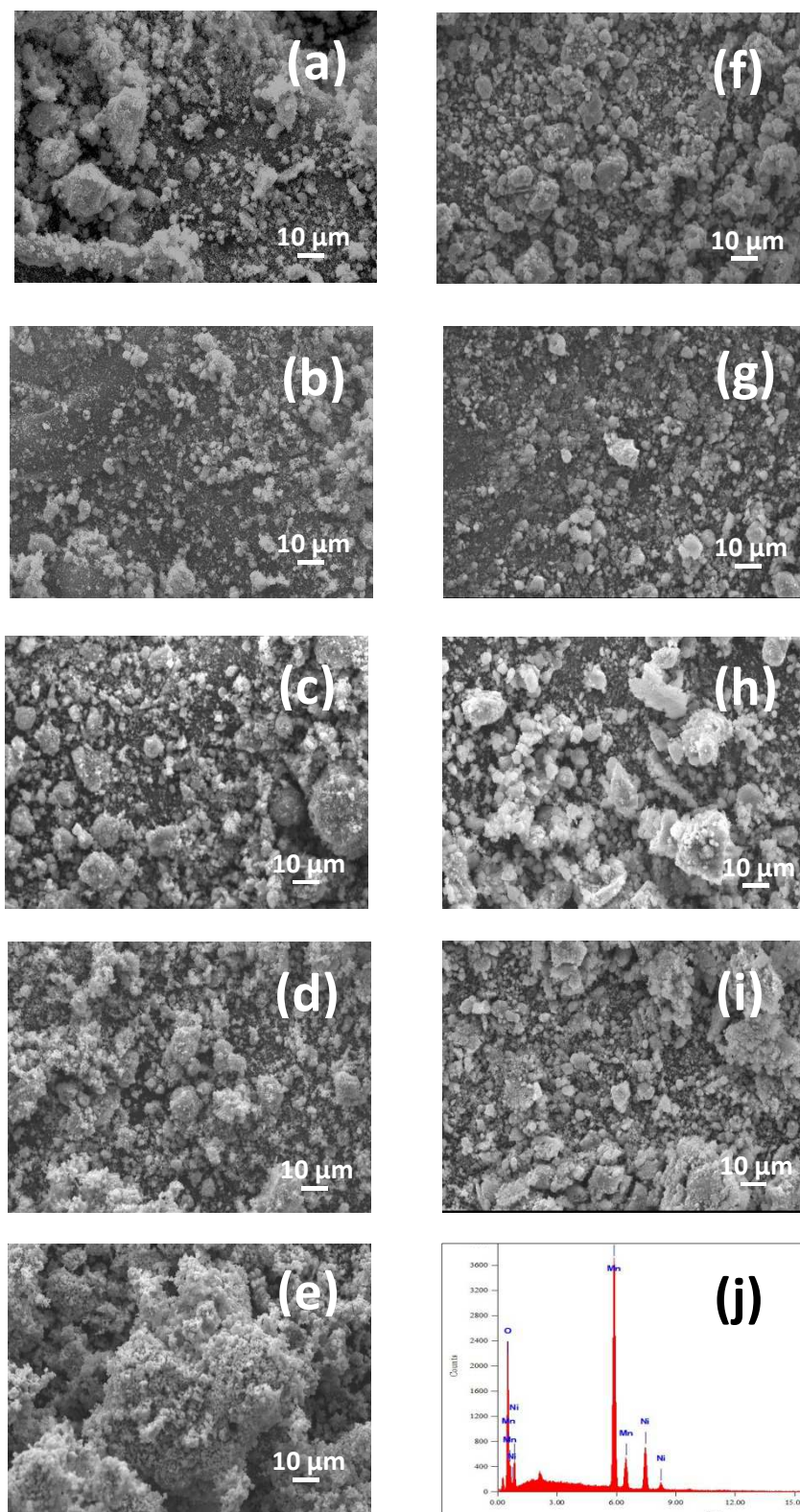


Figure 4.3 SEI of spinel LNM and LMO, synthesized at different temperatures (a-e are spinel LMO, f – i are spinel LNM), (a & f) – 500 °C-3h, (b & g) – 500 °C – 10h, (c & h) – 600 °C -10h, (d & i) – 700 °C – 10h, e – 800 °C – 10h, j – EDX spectrum from LNM_500_10h

Secondary electron images of the various spinel LMO and LNM samples synthesized via hydroxide co-precipitation and annealing are given in figure 4.3 (a-i). In general, the morphology is irregular and the samples consist of particles in the size range of 5 – 20 μm . These big particles are in turn made up of smaller crystallites that are less than 100 nm in size. As the annealing temperature is increased sintering of these crystallites can be observed. EDX analysis of the spinel LNM (figure 4.3 j) was also performed and the Ni: Mn mass ratio was determined to be approximately 0.348 against the expected value of 0.350 suggesting that the stoichiometry of the spinel is around the expected value. Since temperatures are resulting in sintering of particles, it can be assumed that there would be a decrease in the surface area of the samples as well. Hence as annealing temperature increases, there would be sintering of the particles resulting in bigger particles as well as reduced surface area.

4.2.3 Fourier Transform Infrared spectroscopy (FTIR)

This can be discerned clearly in FTIR/Raman spectroscopy which are both sensitive to changes in the vibrational bands. In this respect, the various LNM samples were subjected to analysis and the results are presented in figure 4.4a. For comparison, the FTIR spectra of LMO samples are also provided.

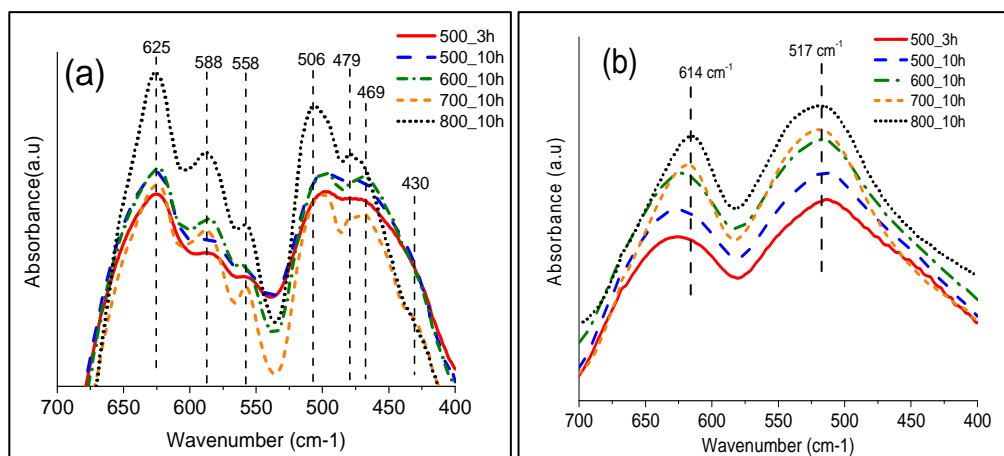


Figure 4.4 FTIR spectra of (a) LNM (b) LMO.

From the XRD results, it was clear that it was not possible to assign a definitive space group to the different samples. It is known that FTIR is a very useful technique when it comes to identifying the space group for LNM [5–7]. The basis for this is that the difference in arrangement of nickel and manganese ions (in the ordered and disordered structures) would give rise to different/extra vibrations for one of the phases (ordered phase).

The spectra of LMO reveal two major bands at around 614 cm^{-1} and 517 cm^{-1} as indicated in figure 4.4b. The results are in line with other studies reported for LiMn_2O_4 [8]. There seems to be a slight shift in the 614 cm^{-1} band towards increasing wavenumber with decreasing synthesis temperatures. This suggests a variation in the asymmetric stretching vibration of the MnO_6 octahedra. This possibly arises because of minor differences in the valence state of manganese between the different LMO samples. However no other noticeable bands are present. Nickel substitution leads to the presence of well-defined bands as highlighted by the dashed lines. Prominent amongst these are the bands at 625 cm^{-1} and 588 cm^{-1} . It has been suggested that for an ordered space group, the 588 cm^{-1} and 558 cm^{-1} bands become more well defined and that their intensity increases relative to the 625 cm^{-1} band [5–7] with increasing amounts of ordered phase in the mixture. Furthermore, extra bands at 430 cm^{-1} and 469 cm^{-1} are also observable for the ordered space group. On the other hand, for a disordered structure (with $Fd\bar{3}m$ space group), the 588 and 558 cm^{-1} bands are less intense and not well defined. Keeping this in mind, the above spectra were compared with available literature to obtain an idea of the possible space groups. The analysis suggests that the LNM_500_3h and LNM_500_10h samples clearly belong to the $Fd\bar{3}m$ space group since the bands at 588 and 558 cm^{-1} are not well defined nor do they display the extra bands observed for an ordered structure. The LNM_600_10h sample displays sharper bands at $588/558\text{ cm}^{-1}$. For the LNM_700_10h and LNM_800_10h samples, the extra band at 430 cm^{-1} corresponding to the ordered structure is also evident. However a one-one correspondence with the literature results for the ordered structure is not present. This leads to the conclusion that the 600, 700 and 800 °C samples most probably consist of a mixture of both ordered and disordered phases. It is also evident that the peaks are the well-defined for the 700 °C calcined samples. This would indicate that this sample possibly has the highest amount of ordered phase amongst all the samples. The 800 °C sample displays reduced peak intensities for the $588/558\text{ cm}^{-1}$ bands suggesting that whatever ordered phase that would have formed at 700 °C would again begin converting to a disordered phase. This has again been well documented in literature [9]. Based on the observations, it is concluded that the LNM_500_3h, LNM_500_10h samples most likely consist of purely disordered phases while the remaining samples consist of a mixture of both ordered and disordered phases with the disordered phase constituting a majority.

However at this stage, it would not be possible to quantify the amount of ordered and disordered phases via this technique. Fortunately one can obtain more information from electrochemical characterization as well regarding the amount of ordered phases as will be shown later. The best method to identify and quantify the presence of ordered phase would be neutron powder diffraction which is not an easily accessible facility.

4.2.4 Thermal analysis

In order to determine if it is possible to obtain more information about the nature of the LNM samples synthesised, TGA was performed in an argon atmosphere. The weight loss of samples was measured by ramping up the samples to 900 °C at a rate of 10 Kelvin/minute. The results are presented in figure 4.5.

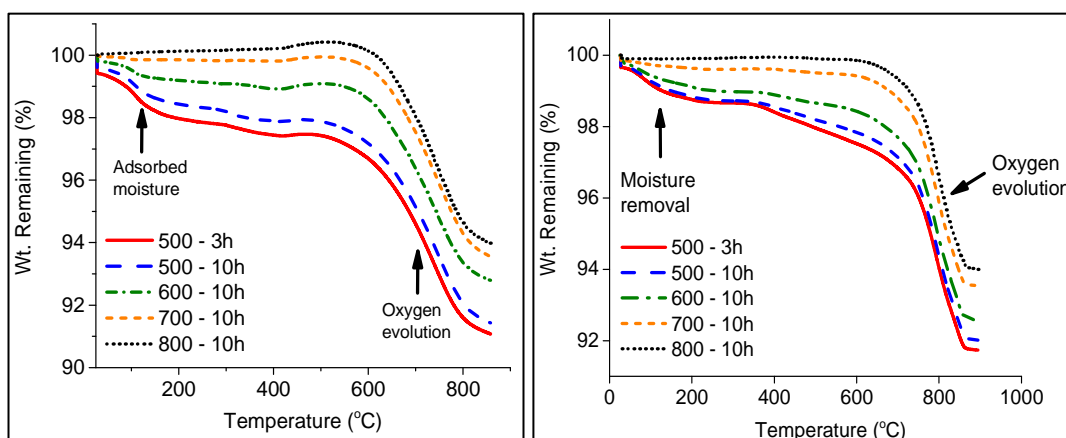


Figure 4.5 TGA of samples (a) LNM (b) LMO

The weight remaining in the samples is plotted as a % of the initial mass for the different samples. Samples calcined at 500 °C for 3 hours displayed the highest weight loss for both LMO and LNM. The total weight loss decreased with increasing annealing temperature for both LMO and LNM. Two major losses were observed. The first one occurs at around 95 – 120 °C for all the samples. This can be attributed to the removal of moisture adsorbed on the samples. This loss is directly proportional to the amount of adsorbed moisture on these samples. Hence the loss is highest for the 500 °C/3h samples which would be expected to have the highest surface area while it is almost zero for the 800 °C/10h sample which would be expected to have very low surface area. The second major weight loss arises from oxygen loss that is initiated at a temperature of roughly 450 – 600 °C for LNM depending on the synthesis conditions. For the spinel LMO, the onset temperatures seem to vary more widely from 400 °C –

700 °C depending on synthesis temperatures. The extent of weight loss is about roughly 6.3 – 6.5 % for both the spinel LNM and LMO. For the spinel LNM, this would indicate that the majority phase in all the samples is possibly the same for all samples (i.e $Fd\bar{3}m$). Considered together with the XRD and FTIR studies, it would be possible to conclude that the major phase present in all the samples is the disordered phase with $Fd\bar{3}m$ space group for spinel LNM.

4.2.5 Cyclic voltammetry

Electrochemical testing for the spinel LMO and LNM was performed in 2 different voltage ranges - the high voltage range (3.2 – 4.3V vs. Li/Li⁺ for spinel LMO and 3.5 - 5 V vs. Li/Li⁺ for spinel LNM) and the low voltage range (2.3 -3.3 V vs. Li/Li⁺ for both spinels). Initially LMO_800_10h and LNM_800_10h samples were fabricated into electrodes and subjected to electrochemical testing. Figure 4.6(a) presents the cyclic voltammograms in the low voltage range while figure 4.6(b) depicts the performance in the high voltage range.

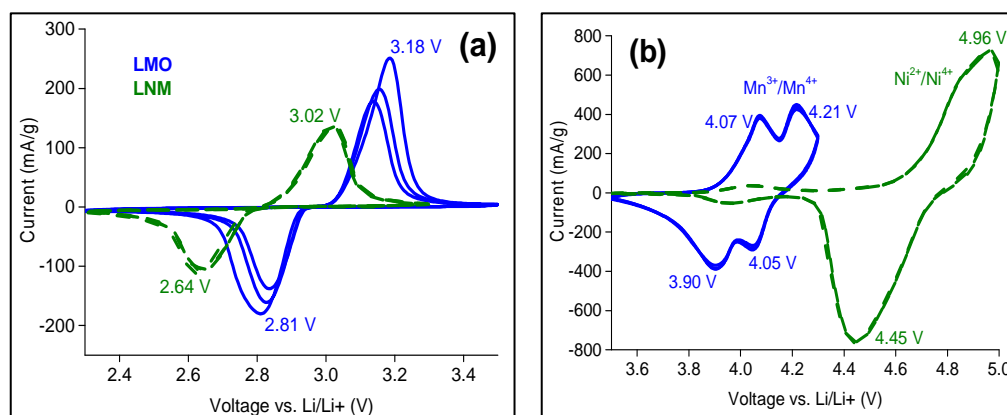


Figure 4.6 CV of spinel LMO and LNM in (a) 2.3 – 3.3 V and (b) 3.2 – 5 V, scan rate - 0.2 mV.s⁻¹, Blue solid curve - spinel LMO, green dashed curve – spinel LNM, both samples calcined at 800 °C – 10h.

During cycling in the lower voltage range, LMO_800_10h indicates reversible reduction and oxidation peaks at 2.81 and 3.18 V respectively which corresponds to the $Mn^{3+} \leftrightarrow Mn^{4+}$ couple. A polarization of 0.37 V is observed between the reduction and oxidation processes. Subsequent cycles display rapid fading in peak current as well as a shift in peak positions. The peak separation reduces to 0.29 V in the subsequent cycles (2.84 and 3.13 V respectively for reduction and oxidation processes). The LNM_800_10h exhibits peaks corresponding to the same $Mn^{3+} \leftrightarrow Mn^{4+}$

couple at 2.64 and 3.02 V respectively indicating a peak separation of 0.38 V. However, subsequent scans do not reveal a fading in performance like the LMO_800_10h sample.

The performance in the higher voltage region is however different for the 2 samples owing to the 2 different operating redox couples in operation. LMO_800_10h displays 2 distinct oxidation peaks at 4.07 and 4.21 V and 2 corresponding reduction peaks at 3.9 and 4.05 V (in the range of 3.2 - 4.3 V). The responsible redox couple here is $\text{Mn}^{3+} \leftrightarrow \text{Mn}^{4+}$. LNM_800_10h on the other hand displays reduction and oxidation peaks at 4.45 and 4.96 V by virtue of the $\text{Ni}^{2+} \leftrightarrow \text{Ni}^{4+}$ redox couple. This is slightly different from the literature reports [10] which report values of 4.65 – 4.7 V for the reduction and 4.75-4.85 V for the oxidation process. This is possibly due to the higher scan rate employed (0.2 mV/s). There are also another set of peaks observed at around 4V for LNM_800_10h. This can be ascribed to the presence of minor Mn^{3+} in the material. The current obtained is higher than that observed while scanning in the lower voltage range for both samples. No fading is observed with repeated scans in the higher voltage region unlike the low voltage region.

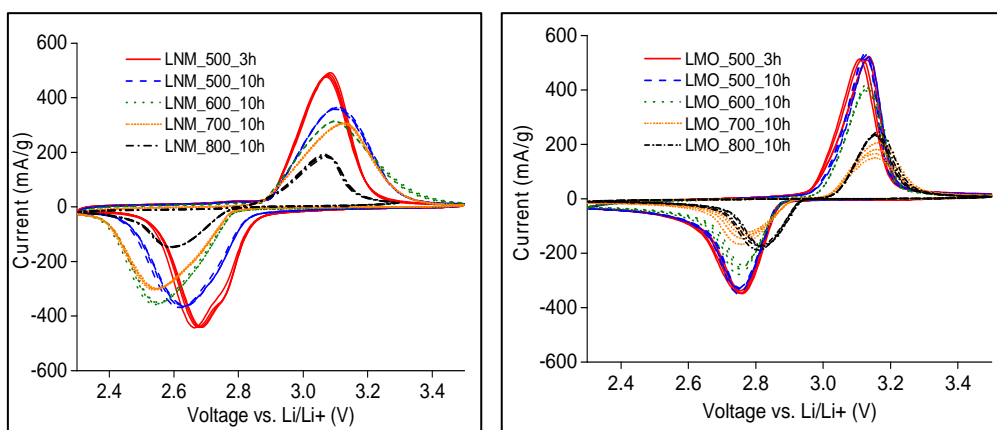


Figure 4.7 CV of spinels (a) LNM (b) LMO, voltage range 2.3 – 3.3V, scan rate – 0.2 mV.s⁻¹.

Next the effect of annealing temperature on the performance was evaluated for both spinel LMO and LNM in the low voltage range. CV curves at 0.2 mV/s is given in figure 4.7(a & b) for both spinel LNM and LMO samples. For the LNM samples, two distinct features are observable. First as the synthesis temperature increases, there is a shift in peak positions (more clear for the reduction peaks). The LNM_500_3h displays reduction and oxidation peaks at 2.67 and 3.08 V respectively while

LNM_700_10h exhibits peaks at 2.54 and 3.12 V. Peak separation is 0.39 V and 0.58V respectively for the two samples suggesting a significant polarization in samples annealed at elevated temperatures. The effect is evident even for LNM_500_10h (2.63 and 3.1 V with a peak separation of 0.47 V). For the LNM_800_10h, reduction and oxidation peaks are observed at 2.59 and 3.07 V respectively with a peak separation of 0.48V. Secondly, as the calcination temperature increases, there is a decrease in the peak current suggesting that capacity obtained would decrease. The peak current for LNM_500_3h is about 2.6 times that observed for LNM_800_10h.

For the spinel LMO, the trends are not obvious as for spinel LNM. For all the samples annealed between 500 °C and 700 °C, the peak shifts are not significant (2.75 & 3.12 V for 500 °C– 3h, 2.75 & 3.16V for 700 °C – 10h). Only for LMO_800_10h, the shift in position of the reduction peak is obvious (2.81 V). Similar to the spinel LNM, a decrease in peak current is observed with increasing calcination temperatures. The peak current decreases with repeating scans for samples annealed at higher temperatures (700/800 °C). This is again similar to spinel LNM.

4.2.6 Galvanostatic cycling

Galvanostatic cycling data at a rate of 30 mA.g⁻¹ (0.2C) is given in figure 4.8 (a-d). The data on performance is presented again for the 2 voltage ranges of testing. To obtain a clearer picture, the data has been consolidated in Table 4.2. For the spinel LMO, the 1st cycle discharge capacities increase with increasing annealing temperature. LMO_700_10h delivers 114 mAh.g⁻¹ after 50 cycles which is the best amongst all the samples. The capacity retention after 50 cycles is about 91 – 96 % of initial capacity for all samples except LMO_800_10h which retained only 73 % of the initial capacity. For the spinel LNM, the 1st cycle discharge capacity was observed to increase with the annealing temperature similar to the spinel LMO. LNM_800_10h delivered 121 mAh.g⁻¹ after 50 cycles which was the best amongst all the LNM samples. The capacity retention after 50 cycles was in the range of 80 – 97 % with LNM_700_10h displaying the highest value. The stability of the electrolyte employed is also an additional factor for spinel LNM compared to spinel LMO. The first charge capacity is higher than the theoretical value of 148 mAh.g⁻¹ for all samples except LNM_800_10h. The cycling efficiency (figure 4.9) demonstrates this clearly. With a reduction in annealing temperature, there is a significant decrease in the efficiency

during cycling. It is to be noted that the formation cycles have been included in the data presented here.

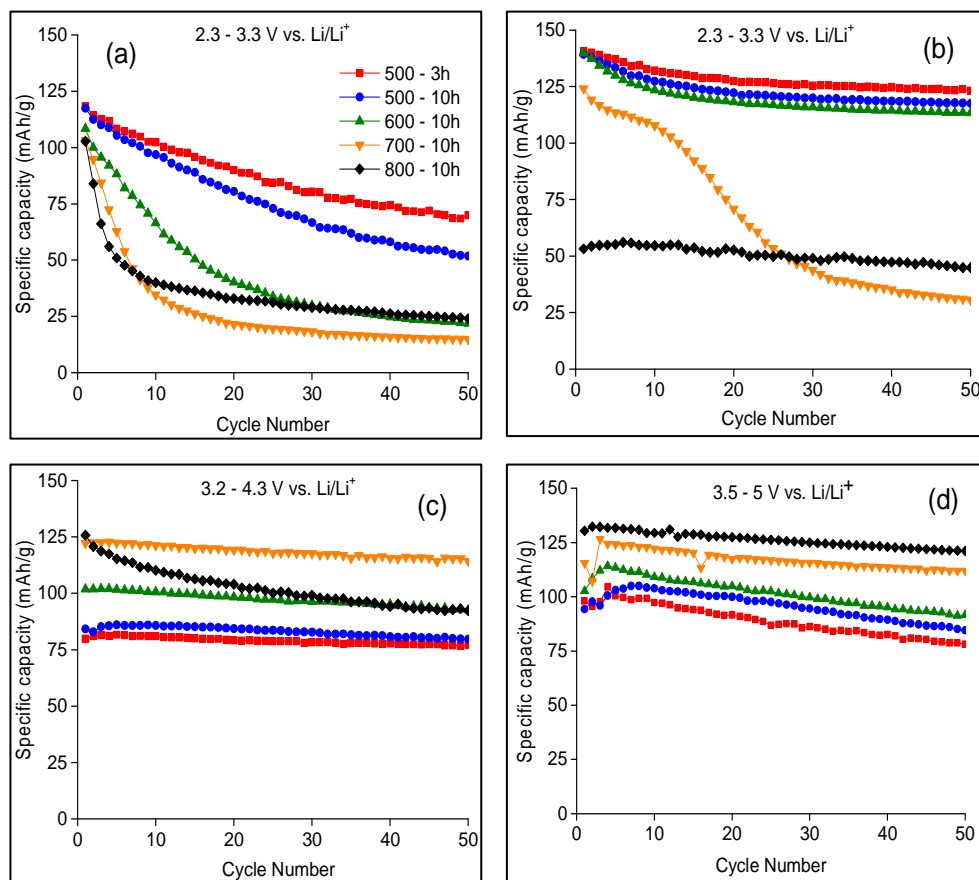


Figure 4.8 Galvanostatic cycling performance of (a & c) spinel LMO, (b & d) spinel LNM, rate – 30 mA.g^{-1} (0.2C), voltage ranges as specified.

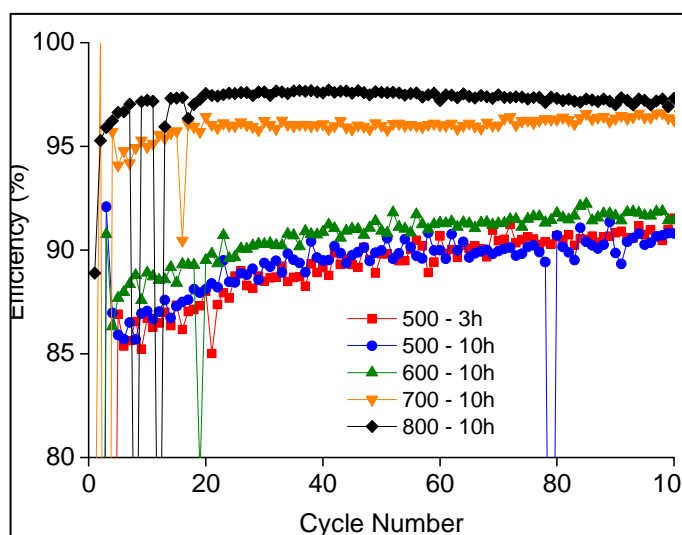


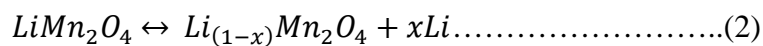
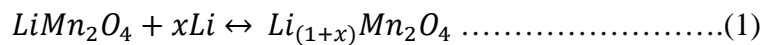
Figure 4.9 Efficiency of spinel LNM samples cycled in 5V region

Table 4.2 Initial capacities and retention for spinel LMO & LNM, (error in capacities is about ($\pm 4 \text{ mAh.g}^{-1}$))

Sample	1st charge (mAh.g⁻¹)	1st discharge (mAh.g⁻¹)	50th discharge (mAh.g⁻¹)	% retention after 50 cycles
Spinel LMO – 3.2 – 4.3V				
LMO_500_3h	83	79	77	96
LMO_500_10h	88	84	79	94
LMO_600_10h	105	101	92	90
LMO_700_10h	127	122	114	93
LMO_800_10h	133	125	92	73
Spinel LNM – 3.5 – 5V				
LNM_500_3h	166	97	78	79
LNM_500_10h	158	94	84	89
LNM_600_10h	162	102	91	89
LNM_700_10h	160	115	111	97
LNM_800_10h	146	130	121	92
Spinel LMO – 2.3 – 3.3V				
LMO_500_3h	118	129	68	53
LMO_500_10h	117	127	51	40
LMO_600_10h	108	116	22	18
LMO_700_10h	103	110	14	13
LMO_800_10h	102	107	24	22
Spinel LNM – 2.3 – 3.3V				
LNM_500_3h	140	145	121	83
LNM_500_10h	139	143	115	80
LNM_600_10h	139	143	112	78
LNM_700_10h	124	128	30	24
LNM_800_10h	53	56	44	79

The performance of the spinels in the 2.3 – 3.3 V range is different from the performance in the 4-5V range. For the spinel LMO, the 1st cycle discharge capacities are in the range of 105 – 130 mAh.g⁻¹ with LMO_500_3h delivering the highest capacity of 129 mAh.g⁻¹. With an increase in annealing temperature, the 1st cycle discharge capacity decreases gradually to 107 mAh.g⁻¹ for LMO_800_10h. The capacity delivered after 50 cycles reduces drastically with increasing annealing temperatures. LMO_500_3h retains a capacity of 68 mAh.g⁻¹ (53 % of initial capacity). On the other hand, LMO_700_10h which delivered the best performance in the high voltage range is able to deliver only 14 mAh.g⁻¹ (13.5 % of the initial capacity). Spinel LNM annealed at all temperatures except 700 °C/800 °C display higher 1st cycle capacities and much better retention compared to the spinel LMO. LNM_500_3h delivers a capacity of 145.6 mAh.g⁻¹ in the 1st cycle and retains 121.8 mAh.g⁻¹ (83.6 %) after 50 cycles. This is 30 % higher than the retention obtained for LMO_500_3h. On the other hand, LNM_700_10h retains about 24 % at the end of 50 cycles (about 11 % higher than LMO_700_10h). The initial capacity for LNM_800_10h is roughly half that of LMO_800_10h. However about 80 % of the initial capacity is retained after 50 cycles. Overall, spinel LNM exhibits much improved performance compared to spinel LMO which displays lower capacities, faster fading and poorer retention during cycling in the lower voltage range.

To understand the reasons for the results presented from galvanostatic cycling, we need to consider the degradation mechanisms at work. As already pointed out in the literature section, there are 2 dominant mechanisms for fading in manganese based oxides, namely manganese dissolution and structural transformation due to co-operative Jahn-Teller distortion. Equations (1) and (2) indicate the electrochemical reaction that would be expected to occur when spinel LMO is cycled in 2.3 – 3.3 V and 3.2 – 4.3 V ranges respectively.



It is clear from reaction (1) that more Mn³⁺ ions are created in the structure during cycling (as average manganese valence varies between +3.5 and +3) when compared to reaction (2) (where average manganese valence varies between +3.5 and +4). Mn³⁺ as already discussed is susceptible to manganese dissolution as well as a high spin ion

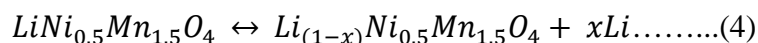
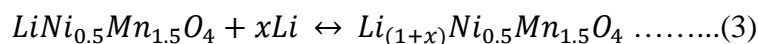
susceptible to the Jahn-Teller effect. Hence it can be expected that reaction (1) would give rise to a more severe structural degradation compared to reaction (2). This is evident from comparing the capacity retention values at the end of 50 cycles for the spinel LMO cycled in different voltage ranges. But when the reaction (1) is the same for all spinel LMO samples synthesized at different temperatures, how could it be possible that they are not fading at the same rate? This could partly be explained based on the particle size and surface area of the different spinel LMO samples synthesized. Both the particle size and surface area are significantly affected by the temperature and time of annealing employed in synthesis.

It is a well-known fact that lower synthesis temperatures usually result in smaller particle sizes during synthesis as fusion of particles via diffusion is quite limited at low temperatures. It is also known that particles with smaller size are more accommodative of the stresses generated during cycling [11]. Furthermore, the interphase formed between cubic and tetragonal phases (discussed in Sec 2.3, page 22) might be able to move throughout a smaller particle easily while finding it difficult to move inside a large particle. In this case, it is expected (and verified from SEM imaging) that as the synthesis temperature is decreased, the particles become finer. This would explain the observed trends for the spinel LMO which shows much better performance (on a relative scale) for the spinel LMO_500_10h compared to LMO_800_10h. It should however be noted that smaller particle size would result in a significantly higher contact area between the electrolyte and active material thereby accelerating the process of manganese dissolution. To sum up, when spinel LMO samples calcined at different temperatures are subjected to cycling in the voltage range 2.3 – 3.3V, they are degraded simultaneously by 2 different processes, the extent of which are significantly altered by the particle size.

In case of spinel LMO cycled in the 3.2 – 4.3V, again both these processes (Jahn-Teller induced structural changes and manganese dissolution) would be prevalent but to a much reduced extent since the amount of Mn^{3+} generated in the structure is much lower than that generated while cycling in the 2.3 – 3.3V range. In this case however, manganese dissolution would be expected to dominate as the capacity fading mechanism (Jahn-Teller induced structural changes would probably become significant at higher rates of cycling when the average local valence of manganese on the surface of the active particle can reduce below +3.5). As discussed earlier, lower

particle size would aid the manganese dissolution more thereby resulting in lower capacities and poorer performance for materials annealed at lower temperatures. This can explain the observed trends for spinel LMO cycled in the 3.2 – 4.3V range with LMO_500_3h displaying the worst performance and LMO_700_10h displaying the best electrochemical performance. The LMO_800_10h sample displays higher initial capacity but more pronounced fading. This could possibly be attributed to oxygen loss that is initiated in the spinel at 780 °C [12] which results in the formation of other detrimental phases.

Let us consider now the performance of the spinel LNM in the two voltage ranges (2.3 – 3.3V and 3.5 – 5V). The respective lithium intercalation reactions are given below.



Equation (3) refers to the performance of the spinel LNM in the 2.3 – 3.3V range. In this case, the average valence of manganese varies between +3.5 and 4 for insertion and extraction of 0.75 mol of Li⁺ into the structure. Hence the amount of Mn³⁺ present in the structure would be significantly reduced (compared to an un-substituted spinel). Accordingly, dissolution of manganese would reduce significantly. Moreover, the nature and extent of structural transformation induced by Jahn-Teller distortion should be different (from that of spinel LMO) since there is Ni²⁺ in the structure. Amine et.al. [13] have shown that chemically lithiating spinel LNM does not lead to the formation of a new phase (with tetragonal symmetry). Coupled together with small particle sizes, this might explain the observed superior performance of the LNM_500_3h and LNM_500_10h samples. However with increasing temperature of synthesis, the capacity obtained decreases. For example, LNM_800_10h displays a very low capacity of 50 mAh.g⁻¹. LNM_700_10h on the other hand seems to display higher initial capacity but rapidly fades (similar to LMO_700_10h samples). However this cannot be explained only using particle size as there is the effect of space group to consider as well. From the characterisation studies conducted earlier, it was concluded that as the synthesis temperature increased for LNM, the phases also changed from a purely disordered phase to a mixture of ordered and disordered phases. This makes it difficult to interpret the effect in terms of space groups as well since the exact percentage of the two phases is unknown. Literature has conflicting reports about the

electrochemical performance of spinel LNM in the 3V region. At this point the only likely reason for the observed performance of spinel LNM_700 and LNM_800 seem to be the presence of a mixed structure with both ordered and disordered forms. Nevertheless, all spinel LNM samples do display fading over 50 cycles and manganese dissolution certainly is one of the major reasons for that can explain the fading.

Finally the spinel LNM samples when cycled in the voltage range of 3.5 – 5V, display increasing capacities with increasing synthesis temperatures and better retention as well. This behaviour can again be correlated with particle size and almost no structural transformation due to the complete elimination of Mn^{3+} in the redox reaction. Lower temperatures of synthesis would result in lower particle size/higher surface areas which would multiply the effect of electrolyte decomposition significantly. This is also observable clearly in the 1st charge capacities (and efficiencies observed) which exceed the theoretical capacity for spinel LNM based on the $\text{Ni}^{2+}/\text{Ni}^{4+}$ redox couple for all the samples except LNM_800_10h. Electrolyte decomposition will directly influence capacity retention as well. This can explain the observed increase in capacity retention with cycling with increasing temperature of synthesis.

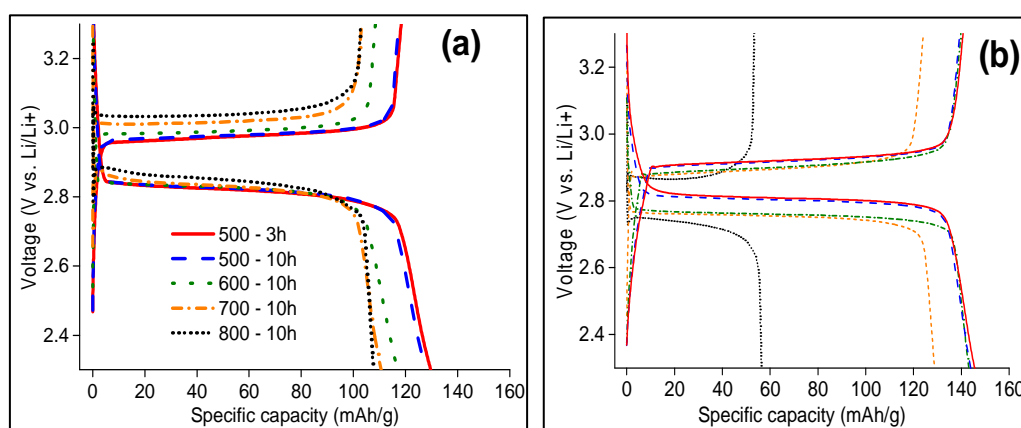


Figure 4.10 First cycle charge – discharge curves of spinel (a) LMO (b) LNM, 2.3 – 3.3 V, legends as indicated in fig (a)

The 1st cycle charge and discharge curves presented in figure 4.10 (a & b) for spinel LMO and LNM. Lithium insertion occurs at around 2.8 V for both spinel LMO and LNM samples. The average voltage of lithium insertion for the different spinel LMO samples is around 2.83 – 2.85 V while it is 2.75 to 2.8 V for the different spinel LNM samples. While there is not much polarization for lithium insertion voltage for spinel LMO, a trend is evident for spinel LNM. With increasing synthesis temperatures,

lower voltages are required to accomplish it. The lithium extraction voltage ranges from 2.97 – 3.03 V for the spinel LMO samples while it is around 2.86 – 2.92 V for the spinel LNM samples. Similarly, there seems to be a trend for spinel LMO for the lithium extraction voltages. As synthesis temperatures increase, there is an increase in the voltage required to extract the lithium from the structure for the spinel LMO. It seems as though nickel substitution seems to have the effect of slightly lowering the average voltages for both lithium insertion and extraction. The number of mols of lithium inserted into/extracted from the structure and the amount of lithium lost in the 1st cycle are given in the table 4.3. In the spinel LNM, lesser amount of Li⁺ is lost in the first cycle compared to the spinel LMO irrespective of the annealing temperatures of the samples.

Table 4.3 Amount of lithium cycled and irreversible loss, 1st cycle (1mol of Li⁺ corresponds to a capacity of 150 mAh.g⁻¹)

Temperature	Spinel LMO			Spinel LNM		
	mols of Li ⁺ Dchg	mols of Li ⁺ Chg	Li ⁺ lost	mols of Li ⁺ Dchg	mols of Li ⁺ Chg	Li ⁺ Lost
500 °C – 3h	0.86	0.79	0.07	0.97	0.94	0.03
500 °C – 10h	0.85	0.78	0.07	0.96	0.93	0.03
600 °C – 10h	0.78	0.72	0.06	0.95	0.93	0.02
700 °C – 10h	0.74	0.69	0.05	0.86	0.83	0.03
800 °C – 10h	0.72	0.68	0.04	0.37	0.35	0.02

Lithium can be lost due to a variety of reasons – such as 1) loss of active material due to manganese dissolution (the active mass reduces) 2) loss of accessible active material (due to Jahn-Teller related structural effects) and 3) disruption of lithium diffusion paths due to phase changes occurring.

The rate performance of the spinel LMO and LNM calcined at different temperatures in the voltage range 2.3 – 3.3V is presented in figure 4.11 (a, b). It is clear that spinel LNM displays better performance than the spinel LMO in the voltage range of 2.3 – 3.3V. Irrespective of the annealing temperatures, the capacities obtained are higher for the spinel LNM than the spinel LMO at all rates up to 4C. LNM_500_3h sample delivers the best performance with a capacity of 75 mAh.g⁻¹ at 4C rate compared to

LMO_500_3h which delivers 30 mAh.g^{-1} at the same rate. LNM_500_3h also displays reasonable capacity retention (133 mAh.g^{-1}) once the rate is switched back to 0.2C after a series of high rate cycles. However increasing the rate beyond 4C (6C and 8C) results in an almost similar performance to spinel LMO suggesting the rate capability is improvement is somewhat restricted.

Amongst the spinel samples (both LMO and LNM), the rate capability is clearly affected by the synthesis temperature in the 2.3 – 3.3 V range. LNM_500_3h with the smallest particle size/highest surface area would be expected to display the highest rate capability with increasing temperatures displaying reduced capacities. This is the trend observed as well. Similarly LMO_500_3h displays the highest capacity amongst LMO samples as well.

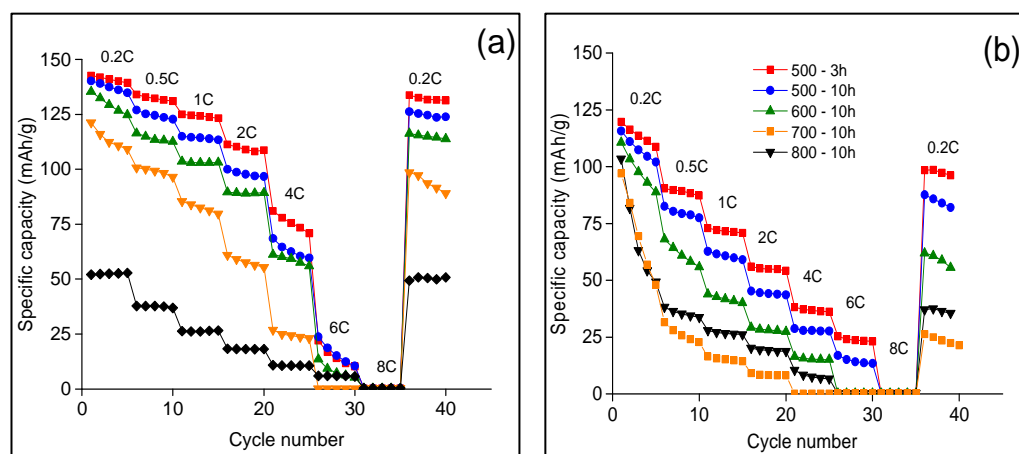


Figure 4.11 Rate capability of spinel (a) LNM and (b) LMO cycled in the voltage range of 2.3 – 3.3V, legends as indicated in figure (b)

It can be expected that co-operative Jahn-Teller distortion related effects are amplified at high rates since the local concentration of Mn^{3+} on the surface would be much higher. Furthermore, at high rates the mobility of the cubic – tetragonal interphase (postulated by Goodenough and co-workers, discussed in section 2.3) will be limited eventually resulting in poor performance. As can be seen from the results, even the best performing samples for LMO (LMO_500_3h) displays significantly low capacities at rates above 2C. A larger particle size is simply going to amplify the Jahn-Teller distortion effect resulting in very poor performance as evidenced for LMO_600, LMO_700 and LMO_800 samples. For spinel LNM, again the effect of Jahn-Teller distortion can be expected to be reduced but not eliminated completely especially at high rates. LNM_500_3h displays reasonable rate performance up to 4C but almost no

capacity at rates above 4C. Again it should be kept in mind that the space group could have an influence on the rate performance as well in case of spinel LNM. As can be seen for LNM_800_10h (and LNM_700_10h above 2C rates) which consists of a mixture of ordered as well disordered phases, rate performance is almost negligible.

The rate performance of the spinels in the 4 and 5V regions is given in figure 4.12.

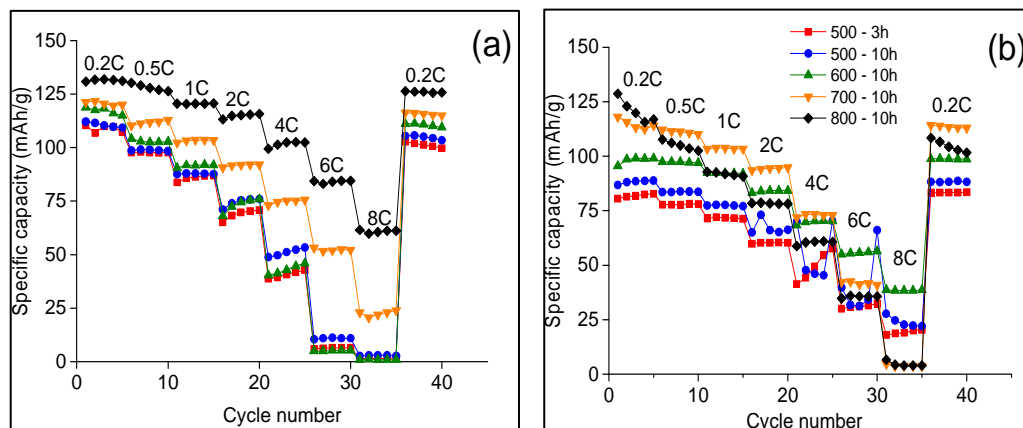


Figure 4.12 Rate capability of spinel (a) LNM cycled in 3.5 – 5V and (b) LMO cycled in 3.2 – 4.3V, legends as indicated in figure (b).

The rate performance of spinel LNM and LMO presented in figure 4.12 (a & b) in the higher voltage ranges (3.2 – 4.3 and 3.5 – 5 V) is again very different from the performance in the 2.3 – 3.3V. The LNM_800_10h sample which displayed lowest capacity in the 2.3 -3.3 V range has the highest capacity at all rates of testing in the 3.5 – 5 V range. LNM_500_3h displayed the lowest capacity and poorest performance in the same voltage range. The trend for spinel LMO in the 3.2 – 4.3 V is however not very clear. The LMO_700_10h sample displays the best performance up to a rate of 4C ($\sim 73 \text{ mAh.g}^{-1}$). However its capacity drops at rates higher than 4C and LMO_600_10h displays higher capacities at 6C and 8C. Here the argument based on synthesis temperatures and particle sizes does not seem to hold. Rather, bigger particles with higher crystallinity seem to offer better performance for both spinel LNM and LMO. In fact the poor performance of spinel LNM_500 and LNM_600 samples is most likely arising from severe electrolyte decomposition that accompanies LNM during charging up to 5V. In case of LNM, Mn dissolution is not expected to be a major reason for capacity fading as very little Mn^{3+} would be present. In case of spinel LMO, it is possible that Jahn-Teller distortion induced structural change would be significantly amplified. This could possibly explain why LMO_700 and LMO_800

samples display poorer performance at high rates (6C and 8C). These samples would not be able to counter co-operative Jahn-Teller distortion as effectively as LMO_500 and LMO_600 samples. In fact at 8C, both the LMO_700 and LMO_800 samples display zero capacity while LMO_600 offers the highest capacity.

To sum up, nickel substitution leads to considerably reduced fading in the 2.3 – 3.3 V. The effect can be attributed to reduced content of Mn^{3+} in the substituted spinel. This would directly reduce the extent of co-operative Jahn-Teller distortion induced damage as well as manganese dissolution.

Synthesis temperatures influence electrochemical performance by altering particle size. Lower synthesis temperatures result in smaller particle sizes which help accommodate the stresses induced by co-operative Jahn-Teller distortion better. But smaller particle sizes most likely also result in accelerated manganese dissolution due to the increased contact area between the electrolyte and active material. Furthermore, finer particle sizes would result in higher rate capability owing to shorter lithium diffusion distances within particles and a higher transfer rate of lithium ions from the particle to the electrolyte. Higher synthesis temperatures result in increasing particle sizes which would make the materials more susceptible to Jahn-Teller distortion induced damage. At the same time, higher synthesis temperatures would result in reducing surface areas which would reduce the extent of manganese dissolution as well as electrolyte decomposition (for spinel LNM). For spinel LNM, higher synthesis temperatures also result in a mixture of ordered and disordered phases which most likely affect the performance as well. For both the spinel LMO and LNM, the most striking aspect is that synthesis temperature affects the electrochemical performance in 2 different voltage ranges differently. This has not been demonstrated thus far in a systematic manner as investigated here.

4.2.7 Cyclic voltammetry at different rates

The presence of nickel stabilizes and improves the performance in the 3V region considerably. To understand further the effect of nickel substitution, cyclic voltammetry studies at different rates were performed on the LMO_500_10h and LNM_500_10h samples to identify if the lithium diffusion coefficient is different in the two materials. These materials are chosen since they are the best performing of all the samples investigated in this voltage range. Randles-Sevcik equation (Equation 5) is

employed to determine the lithium diffusion co-efficient. This method is an approximation as the electrode surface is not flat as specified.

$$I_p = 2.69 \times 10^5 \times n^{3/2} \times D_{Li} \times v^{1/2} \times C_{Li}^0 \text{-----Eq (5)}$$

Where,

$I_p \rightarrow$ Peak current density in A/cm^2 .

$n \rightarrow$ number of electrons per redox active species.

$D_{Li} \rightarrow$ Diffusion coefficient of lithium (cm^2/s)

$v \rightarrow$ Scan rate (V/s)

$C_{Li}^0 \rightarrow$ Concentration of lithium in the cathode (mol/cm^3)

Figure 4.13 gives the plot of anodic peak current density versus the square root of scan rate together with the calculated values for the lithium diffusion co-efficients. The plot reveals the difference in performance between spinel LNM and LMO is very marginal and in fact spinel LMO is slightly better. The diffusion co-efficient values (shown in figure 4.13) calculated from plot reaffirm this observation. This diffusion co-efficient value is an apparent value i.e it represents the average of lithium diffusion processes occurring in different medium like the electrolyte, inside the active material etc. The CV studies do not fully explain how the performance of spinel LNM is better than that of spinel LMO.

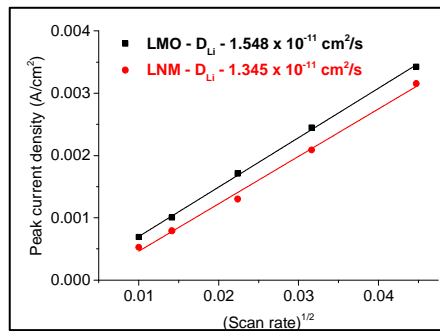


Figure 4.13 Peak current density vs. scan rate for spinel LMO_500_3h and LNM_500_3h, anodic process (lithium insertion).

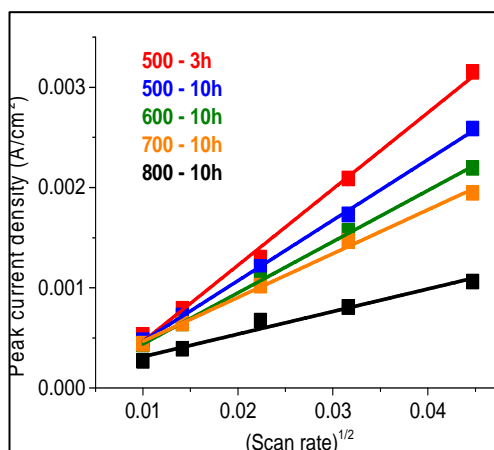


Figure 4.14 Peak current density vs. scan rate for spinel LNM, anodic process (lithium insertion)

To understand the effect of temperature on the diffusion performance, the spinel LNM samples were subjected to cyclic voltammetry and impedance studies as in the preceding section. From the cyclic voltammetry studies, the diffusion co-efficients were calculated as before. Figure 4.14 compares the variation in anodic peak current density with square root of the scan rate for different spinel LNM samples and the diffusion coefficients obtained are given in table 4.4. The trends reflect the galvanostatic cycling and rate testing results where the LNM_500_3h samples displayed the best performance while the LNM_800_10h sample displaying the worst performance. The diffusion coefficients reveal a gradual decrease with increasing calcination temperature suggesting that particle size has an effect on performance.

Table 4.4 Lithium diffusion coefficients in spinel LNM, 2.3 - 3.3V, (for anodic process)

Sample	Lithium diffusion coefficient (cm ² /s)
LNM_500_3h	1.345 x 10 ⁻¹⁰
LNM_500_10h	0.847 x 10 ⁻¹⁰
LNM_600_10h	0.605 x 10 ⁻¹⁰
LNM_700_10h	0.441 x 10 ⁻¹⁰
LNM_800_10h	0.177 x 10 ⁻¹⁰

4.2.8 Electrochemical Impedance Spectroscopy

To further investigate the actual reasons for the improvement in performance of the different samples, impedance spectroscopy was performed on the spinel LNM and LMO samples. The electrodes were assembled into coin cells versus lithium and the cells were subjected to staircase potential electrochemical impedance spectroscopy (SPEIS). This technique involves increasing the voltage in steps and floating the cells for a certain period of time until a steady state is reached (current is zero) and then performing an impedance measurement. This has the effect of measuring the impedance at different states of charge/lithium contents inside the electrode. In this study, the cells were subjected to voltage increases in 6 steps from 3.1 to 2.3 V and then back to 3.1 V in 6 steps. At each step, the cells were floated for 8 hours before the impedance measurement was made. Capacities obtained after resting by integrating the charge from the current-voltage plots are comparable to the values observed from charge-discharge curves. The resulting Nyquist plots were subjected to fitting using equivalent circuits (shown in figure 4.15) from which the resistance to lithium migration across the surface films (R_{sf}), charge transfer processes (R_{ct}) and the Warburg diffusion constant (W) were extracted for the different states of charge for both spinel LNM and LMO. Figure 4.16a shows the Nyquist plots of LNM and LMO samples synthesized at 500 °C for 3 hours. The spectra were recorded at a voltage of 2.7V where the maximum capacity was observed for both spinel LNM and LMO.

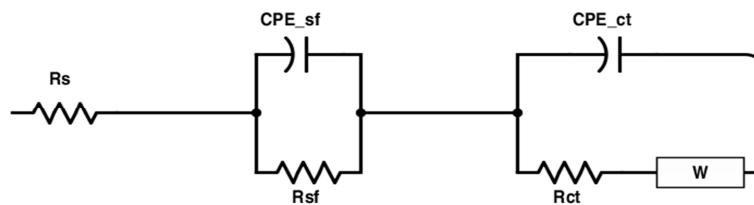


Figure 4.15 Equivalent circuit employed for fitting EIS data

The nyquist plots consist of 2 overlapping semi circles in the high to middle frequency and middle to low frequency range considered to represent impedance arising from two processes namely lithium diffusion across surface films formed (R_{sf}), charge transfer across interface (R_{ct}) (between surface film/active material) while the sloping

line at 45 degrees to both axes represents lithium diffusion inside the active material known (Warburg diffusion) [14–16]. The solution resistance value (R_s) which arises from electrolyte, separator and other cell components was observed to be around 1.5 – 2 Ω for all the cells subjected to analysis. The plot in figure 4.16 (b) gives the total impedance arising from surface films and charge transfer processes as a function of voltage during lithium insertion. For both spinel LMO and LNM, the impedance gradually increases with lithium insertion. Similar trends were reported elsewhere albeit in a different voltage range [14,15].

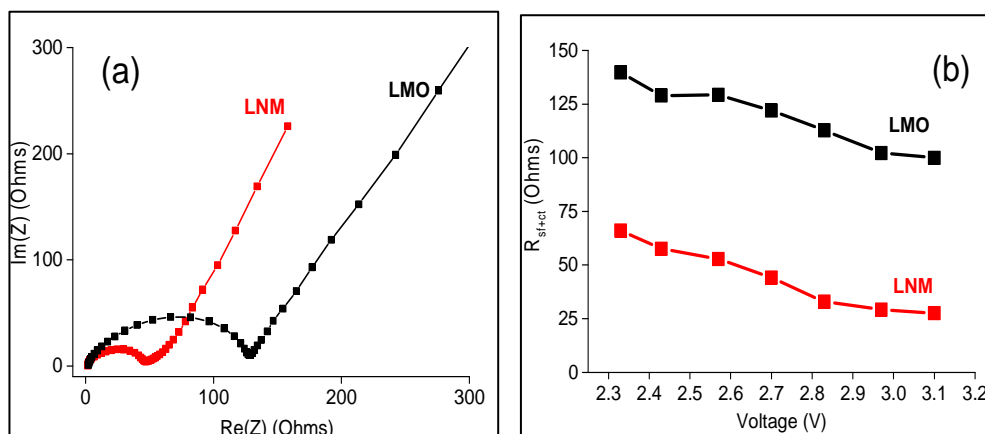


Figure 4.16 EIS analysis of LMO_500_3h & LNM_500_3h, (a) Nyquist plots at 2.7V, (b) Variation of resistance due to surface films and charge transfer processes (R_{sf+ct}) with voltage during lithium insertion.

It is clear that the spinel LNM displays lesser impedance (R_{sf+ct}) over the entire voltage range (3.1 to 2.3V) during lithium insertion compared to spinel LMO. This would indicate that the amount of lithium that can be inserted would be lesser for the LMO compared to LNM. This is reflected during galvanostatic cycling where the amount of lithium inserted in the 1st cycle is 0.86 mols for LMO_500_10h and 0.97 mols for LNM_500_10h. The Warburg impedance obtained from curve fitting for the spinel LNM and LMO are respectively 31.53 and 60.42 Ohms. $s^{-1/2}$. This suggests it is much easier for lithium to diffuse inside the LNM compared to LMO. The higher lithium diffusion coefficient inside the active material coupled with lesser impedance to charge-transfer processes can explain the considerably improved rate performance of the spinel LNM over LMO during rate testing even though cyclic voltammetry does not reveal a significant difference in the lithium diffusion values.

Figure 4.17 reveals the contributions to impedance arising from charge transfer processes and the total impedance to understand the effect of synthesis temperature. The Nyquist plots presented (figure 4.17a) were recorded at 2.83V. This is the voltage where maximum capacity was observed during lithium insertion. This was decided based on observations by Aurbach et.al [14,16] that the second semi-circle corresponding to charge transfer resistance is dependent on the voltage at which the measurement is performed. They showed that at potentials corresponding to peaks in cyclic voltammetry, the diameter of the second semi-circle was the least. It was also evident from their results that this semi-circle may not be fully apparent at potentials other than the peak potential as the size was simply too big to be recorded at the lowest frequencies. From figure 4.17a, it is apparent that the LNM_800_10h displays a similar semi-circle whose diameter is huge suggesting a very big charge transfer resistance compared to the other samples.

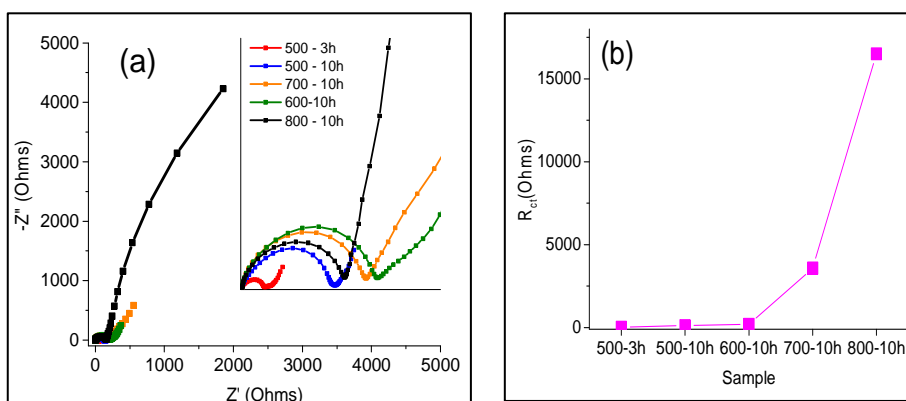


Figure 4.17 EIS analysis for spinel LNM (a) Nyquist plots at 2.83V (inset showing enlarged section of same graph) (b) Charge-transfer resistance for different synthesis conditions.

The Nyquist plots were fitted with the equivalent circuit shown in figure 4.15 again to obtain the charge transfer resistance of the different samples at the peak intercalation potential. The results are plotted in figure 4.17b. It can be clearly seen that the charge transfer resistance increases with increasing synthesis temperature suggesting that it would become progressively more difficult to insert lithium into the structure. Charge transfer resistance actually refers to a combination of processes occurring in the electrode. First is an ionic charge transfer that involves lithium ions being transferred across the surface films and electrode-electrolyte interface into the host. Second is an electronic component that depends on the electronic conductivity of the host material

and the electrical connection present between them (the role played by conductive carbon additives is to improve this electronic conductivity). Both are affected considerably by particle size. Smaller particles would directly result in higher contact area with electrolyte thereby resulting in faster ionic charge transfer/lesser resistance. At the same time, the path an electron has to travel inside the host material is also reduced thus reducing electronic charge transfer resistance as well. Bigger particles on the other hand would result in lesser contact areas between the electrolyte and active material thus resulting in higher resistance to transfer of lithium ions from the electrolyte to the host. Similarly, electrons would also have to travel longer paths to be injected into the conduction bands of the host. This means increased overall resistance to both electronic and ionic charge transfer for bigger particles. The results of impedance analysis clearly mirror the trends observed in galvanostatic cycling where LNM_500_3h displays the highest capacity as well as best rate performance while the LNM_800_10h sample displays the worst performance. Thus the observed results of impedance could be explained based on particle size. But it should also be kept in mind that the effect of space groups on performance cannot be eliminated.

4.2.9 Ex-situ X-ray diffraction

It is clear that nickel substitution improves lithium diffusion kinetics and offers lower impedance which gives rise to better capacities and rate performance. To understand if there was an effect on phase transformation, ex-situ XRD was performed on cycled electrodes.

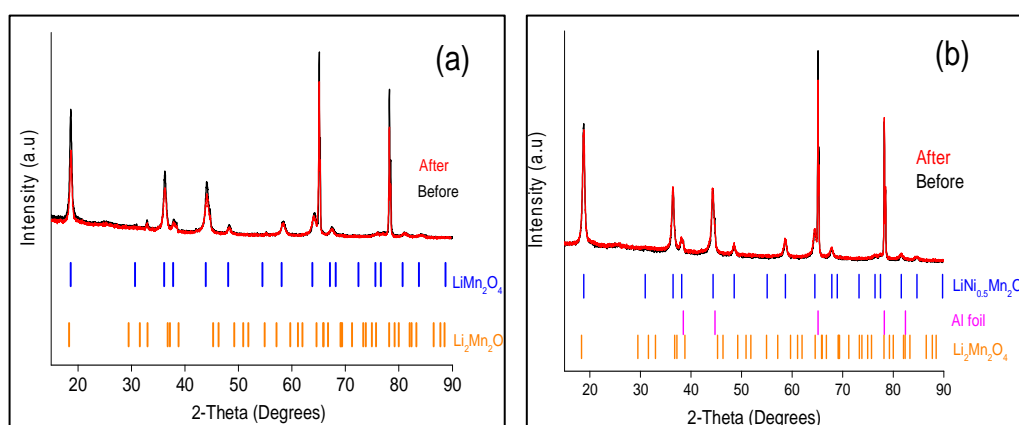


Figure 4.18 Ex-situ XRD patterns before and after cycling for (a) spinel LMO_500_3h and (b) LNM_500_3h

The electrodes were taken as such for the analysis (i.e with the aluminium foil). This would enable aluminium to serve as an internal reference for peak position as well helping to eliminate peak shifts arising due to instrumental factors. The XRD patterns after cycling are presented in figure 4.18. One would expect the formation of $\text{Li}_2\text{Mn}_2\text{O}_4$ during insertion of lithium into spinel LiMn_2O_4 . It is apparent that there are no new phases such as the tetragonal $\text{Li}_2\text{Mn}_2\text{O}_4/\text{Li}_2\text{Ni}_{0.5}\text{Mn}_{1.5}\text{O}_4$ detectable via XRD that form during cycling of either LMO_500_10h or LNM_500_10h. This suggests that the fading mechanism is possibly not structural transformation for these samples. However it is possible that manganese dissolution is occurring in both materials and it might explain the initial capacity fading observed during the 1st 50cycles. However, it was evident that samples calcined at higher temperatures were displaying lesser capacity and fading as well. To verify if phase transformation was occurring in those samples, ex-situ XRD was performed on all the remaining samples of LMO and LNM.

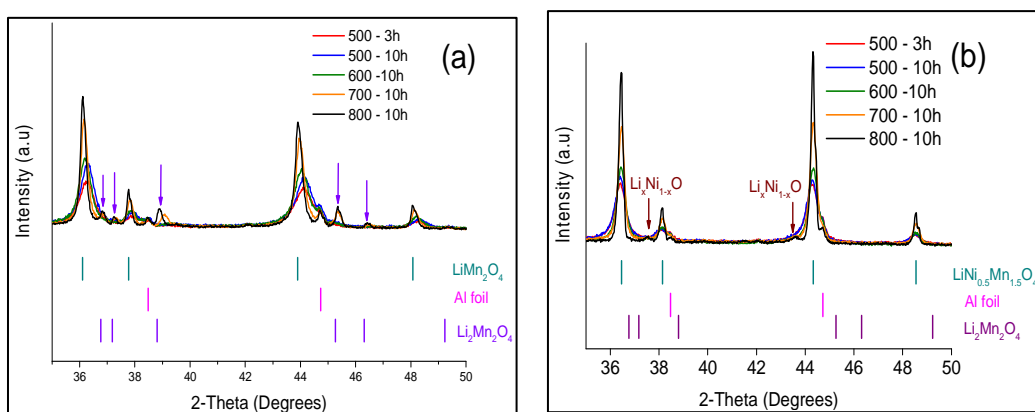


Figure 4.19 Ex-situ XRD of electrodes after cycling for (a)LMO (b)LNM. Purple arrows represent peaks corresponding to $\text{Li}_2\text{Mn}_2\text{O}_4$.

Figure 4.19 (a & b) compares the patterns obtained from electrodes subjected to cycling. It is clear that in the samples calcined at elevated temperatures, $\text{Li}_2\text{Mn}_2\text{O}_4$ phase is generated during cycling. The LMO_500_3h sample does not seem to convert to the $\text{Li}_2\text{Mn}_2\text{O}_4$ phase. However in case of LMO_700_10h and LMO_800_10h, new peaks corresponding to the $\text{Li}_2\text{Mn}_2\text{O}_4$ phase (observable at 18.4° , 36.9° , 37.3° , 38.9° and 45.4° in figure 4.19a) are observed. This suggests that more crystalline LMO is transforming to $\text{Li}_2\text{Mn}_2\text{O}_4$ during cycling.

Nickel substitution seems to alter this behaviour. None of the spinel LNM samples display new phases after cycling as can be seen in figure 4.19b. The only impurity

phase detectable is that of the $\text{Li}_x\text{Ni}_{1-x}\text{O}$ which was already present in the powder after synthesis. A comparison of the patterns of LMO_800_10h and LNM_800_10h after cycling is given in figure 4.20. It clearly reveals that even the worst performing sample of spinel LNM_800_10h (in galvanostatic cycling) does not transform to the tetragonal phase observed in case of spinel LMO. Hence it can be concluded that nickel substitution seems to avoid the formation of new phases during cycling in the voltage range of 2.3 – 3.3V for the spinel structure.

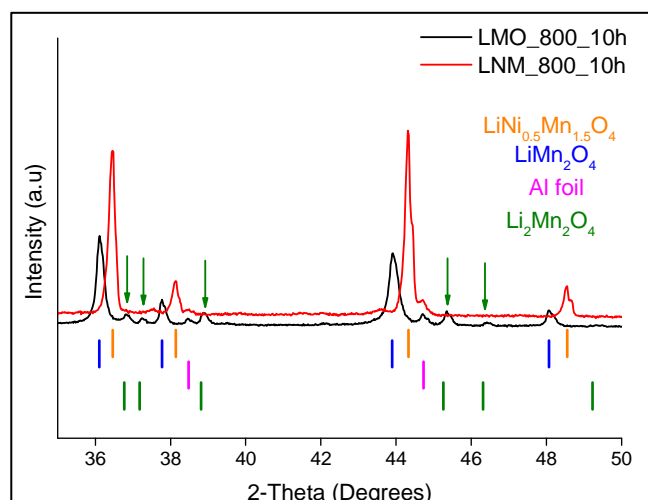


Figure 4.20 Ex-situ XRD of spinel LMO and LNM after cycling.

From the above ex-situ XRD analysis, it is clear that spinel LMO synthesized via annealing at lower temperatures (500 °C & 600 °C) do not seem to undergo the transformation to a tetragonal phase during cycling while the spinel LMO calcined at elevated temperatures (700 & 800 °C for 10 hours) undergo this transformation. The results here demonstrate that for un-substituted spinel LMO, the annealing temperature has an effect on the transformation to the spinel phase. As was discussed in the literature section, it is already well known and documented that the spinel LMO phase transforms to the tetragonal phase on insertion of Li^+ into the LiMn_2O_4 structure. Goodenough and co-workers [17,18] had theorized the possibility of an interface between tetragonal and cubic spinel phases within a crystallite of the particle as the reason for fading in performance. It was already suspected that either nano-sized grains or strains imposed on a particle result can improve the cycling stability of spinel LMO in the 3V region[18]. Hence the performance here could possibly be attributed to the fact that the spinel LMO synthesized at lower temperatures has a smaller particle size (verified by SEM analysis of various samples in section 4.2.2). On the other hand,

nickel substitution helps prevent transformation to the tetragonal spinel phase irrespective of the annealing temperatures. This is in line with the observations of Amine et.al. [13,19] who had claimed that spinel LNM does not transform to tetragonal phase although they had not presented the effect of synthesis conditions on electrochemical performance or the transformation. They had prepared spinel LNM via two methods – sol-gel and solid state methods and demonstrated that chemically lithiated LNM has the same XRD pattern as that of the $\text{LiNi}_{0.5}\text{Mn}_{1.5}\text{O}_4$ suggesting that the structure does not change on insertion of lithium. They suggested that since the initial oxidation state of Mn is +4, this change to tetragonal phase does not occur. This was considered possible since at that time it was thought that as long as the overall Mn valence does not decrease below +3.5, co-operative Jahn-Teller distortion does not set in and hence there would be no structural transformation. However their results do not analyse the cycled electrodes and also does not consider the possibility of the manganese valence falling below +3.5 locally (i.e on the surface of particles) as pointed out by Thackeray et.al [20]. These results however are not in line with the observations made by Park and co-workers [21] who had demonstrated reversible transformation to tetragonal phase for a spinel LNM with an ordered structure ($P4_332$ space group) and irreversible transformation for a spinel LNM with disordered structure ($Fd\bar{3}m$ space group). Again it should be noted that they did not systematically investigate the effect of synthesis conditions on phase transformation. Hence this work provides the first systematic investigation of the effect of synthesis temperature on phase transformation between the un-substituted and nickel substituted spinel LiMn_2O_4 .

4.3 Experimental methods – Titanium substitution in $\text{Li}_4\text{Mn}_5\text{O}_{12}$.

4.3.1 Powder X-ray diffraction

The XRD patterns for the different samples of titanium substituted spinel $\text{Li}_4\text{Mn}_5\text{O}_{12}$ are presented in Figure 4.21a. The XRD pattern on the unsubstituted sample could be indexed to $\text{Li}_4\text{Mn}_5\text{O}_{12}$ (ICSD Coll. Code. 84757). The TiO sample annealed at 400 °C and 500 °C for 2 days could be indexed to pure phase spinel $\text{Li}_4\text{Mn}_5\text{O}_{12}$ as well (figure 4.21a). Rietveld refinements indicate a structure with lattice parameter a of 8.1268 (4) Å and 8.1299 (4) Å respectively for the 400 °C and 500 °C annealed samples. These

values are similar to those reported by Takada et.al. [22]. However phase analysis during refinement of the patterns for the 400 °C annealed Ti0 sample indicated the presence of only about 68 % of the $\text{Li}_4\text{Mn}_5\text{O}_{12}$ phase with about 27.4 % of a $\text{Li}_{1+x}\text{Mn}_{2-x}\text{O}_4$ phase ($x=0.234$, ICSD code : 183748) and about 3 % of Li_2MnO_3 phase (ICSD code:73370). The 500 °C annealed Ti0 sample on the other hand displayed very high purity and no accompanying cation mixed phases/ Li_2MnO_3 .

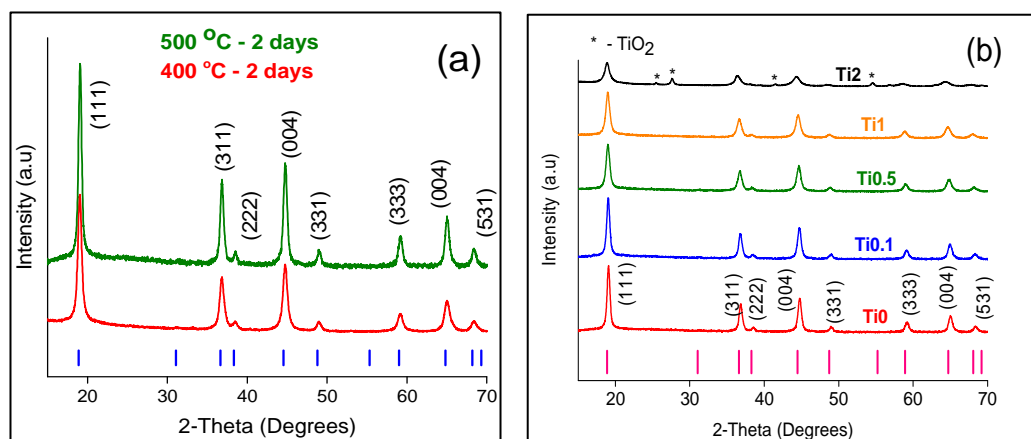


Figure 4.21 XRD patterns of $\text{Li}_4\text{Ti}_x\text{Mn}_{5-x}\text{O}_{12}$ ($0 \leq x \leq 1$) synthesised at different temperatures in O_2 atmosphere (a) $x=0$, 400 °C and 500 °C for 2 days, (b) $\text{Li}_4\text{Ti}_x\text{Mn}_{5-x}\text{O}_{12}$ ($0 \leq x \leq 1$) samples annealed at 500 °C – 2h.

Fig 4.21 (b) presents the patterns of the Ti^{4+} substituted samples calcined at 500 °C for 2 days. Up to 1 mol of Ti^{4+} could be successfully inserted into the lattice of $\text{Li}_4\text{Mn}_5\text{O}_{12}$. Attempting to substitute 2 mols of Ti^{4+} proved unsuccessful with the existing procedure as anatase TiO_2 was found to be present in the XRD patterns indicating Ti^{4+} prefers to crystallize out into a separate phase rather than substituting Mn^{4+} in the lattice. With increasing amounts of Ti^{4+} in the structure, the peak positions shift towards that of $\text{Li}_4\text{Ti}_5\text{O}_{12}$. The parameters obtained from fitting are presented in table 4.5. The lattice parameter increases with increasing Ti^{4+} content. This is in line with expectations since the lattice parameter of $\text{Li}_4\text{Ti}_5\text{O}_{12}$ is 8.354 – 8.359 Å which is higher than that of the manganese counterpart further confirming that Ti^{4+} has substituted Mn^{4+} in the lattice.

Table 4.5 Refinement results for $\text{Li}_4\text{Ti}_x\text{Mn}_{5-x}\text{O}_{12}$ ($0 \leq x \leq 1$), annealed at 500 °C for 2 days in oxygen atmosphere.

Sample	Lattice constant a , Å	R_p	R_{wp}	GOF
Ti0	8.1299(4)	1.74	2.16	1.4
Ti0.1	8.1302(16)	1.46	1.82	1.2
Ti0.5	8.1334(3)	1.7	2.24	1.3
Ti1	8.1444(4)	2.19	2.97	1.6

4.3.2 Cyclic voltammetry

CV curves recorded at 0.2mV/s for samples calcined at 500 °C – 2 days are given in figure 4.22 (a, b). CV traces reveal a reversible lithium insertion process accompanying a concurrent $\text{Mn}^{4+} \leftrightarrow \text{Mn}^{3+}$ redox process for all the samples. In all the 4 samples analysed, the reduction peak position for the first cycle (2.64, 2.65, 2.68 and 2.72V respectively for Ti0, Ti0.1, Ti0.5 and Ti1) is distinct from the rest of the cycles.

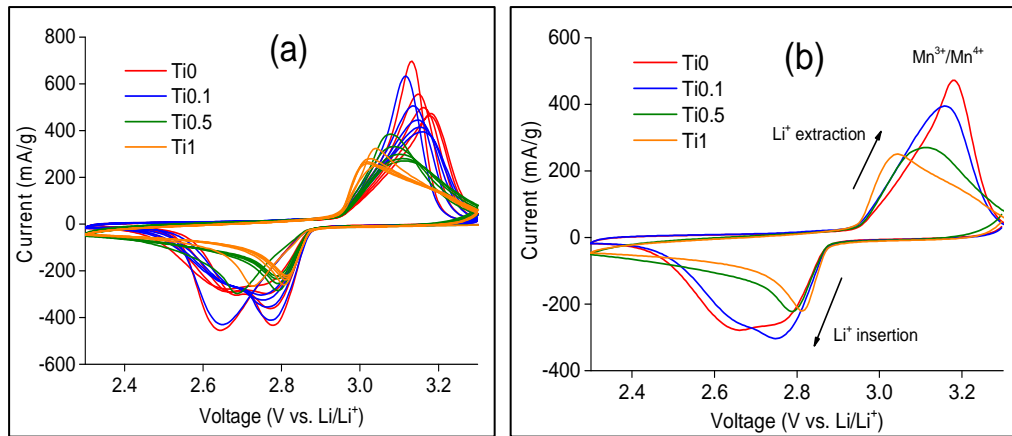


Figure 4.22 CV curves of $\text{Li}_4\text{Ti}_x\text{Mn}_{5-x}\text{O}_{12}$ ($0 \leq x \leq 1$) synthesized at 500 °C for 2 days under O_2 flow (a) cycles 1 – 5, (b) cycle 5, scan rate-0.2mV.s⁻¹

With increasing Ti content, the difference in peak positions between the oxidation and reduction peaks reduces from 0.52 V for the Ti0 sample to 0.23V for the Ti1 sample (see. Figure 4.22 (b), 5th cycle). No other reduction peak is observed indicating the lack of any side reactions or other redox couples (from $\text{Ti}^{4+}/\text{Ti}^{3+}$ for e.g). For the Ti0 and Ti0.1 samples, 2 reduction peaks (2.68 V and 2.78V for Ti0 sample) are observed

in cycles 2-5 while Ti0.5 and Ti1 do not display similar peaks on lithium insertion in cycles 2-5. Furthermore the current from one of these peaks (2.78 V for Ti0 sample) decreases with repeated scans for both samples suggesting whatever process is occurring is gradually fading. For Ti0.5 and Ti1 samples, the increase in current during both lithium insertion and extraction is steep while the decay in current is more gradual making the peaks asymmetric about the peak position. All the 4 samples exhibit fading with repeated cycling and the peak current obtained decreases with increasing Ti content above 0.1 mols.

4.3.3 Galvanostatic cycling

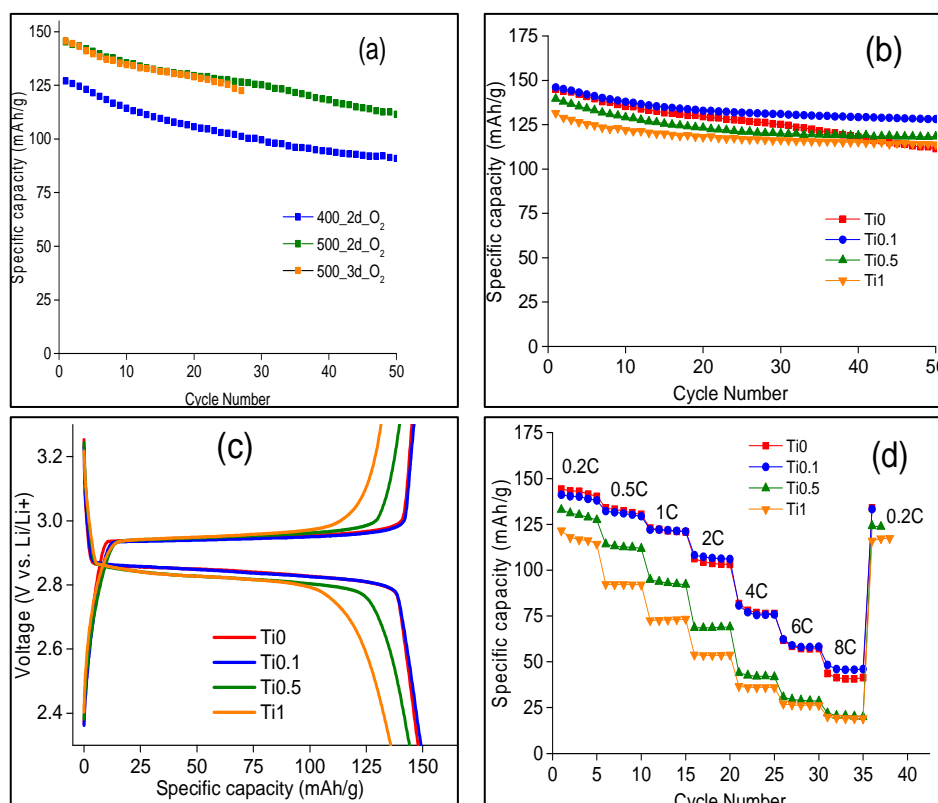


Figure 4.23 Electrochemical performance of $\text{Li}_4\text{Ti}_x\text{Mn}_{5-x}\text{O}_{12}$ in 2.3 – 3.3 V (a) cycling performance for unsubstituted spinel (Ti0) @ 30 mA.g⁻¹(0.2C), (b) cycling performance @ 30 mA.g⁻¹, (c) first charge/discharge (d) rate performance, samples in b-d annealed at 500 °C – 2 days in O₂ flow.

Figure 4.23 (a-d) gives the effect of different annealing conditions employed on the cycling performance and initial capacity. Annealing at 500 °C for 2 days in oxygen provided better performance. Increasing the calcination time to 3 days at 500 °C under oxygen flow did not result in any further increase in observed capacity (EXSP_Ti0_500_3d_O₂). The effect of varying the titanium content is given in Fig b.

The initial capacities are 145, 146, 139 and 131 mAh.g⁻¹ respectively for Ti0, Ti0.1, Ti0.5 and Ti1 samples.

All samples exhibit a gradual fading which is also in line with observations from cyclic voltammetry studies. The fading is marginally higher for the Ti0 sample (76.8% of initial capacity after 50 cycles). By comparison, the fading rate is about 87.8, 84.7 and 86.7 % for Ti0.1, Ti0.5 and Ti1 samples respectively after 50 cycles. This indicates that Ti⁴⁺ substitution is improving capacity retention during cycling. The rate performance reveals that Ti substitution beyond 0.1 mols results in a decrease in performance at all rates. The capacity at 8C rate is approximately 45 mAh.g⁻¹ for Ti0.1.

4.3.4 Cyclic voltammetry at different rates

To understand the effect of Ti substitution on the lithium diffusion kinetics, cyclic voltammetry was performed using different scan rates and a plot of peak current density as a function of square root of scan rate were constructed. It is given in figure 4.24

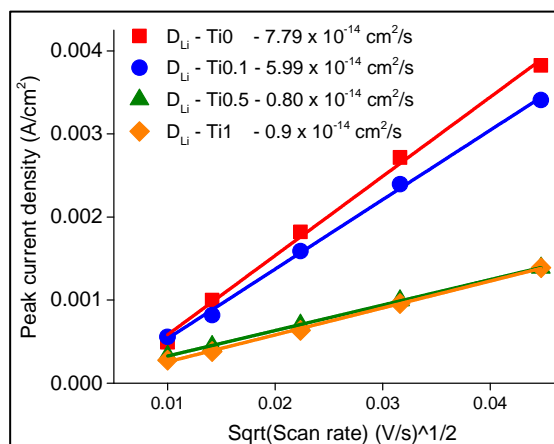


Figure 4.24 Peak current density vs scan rate for $\text{Li}_4\text{Ti}_x\text{Mn}_{5-x}\text{O}_{12}$ ($0 \leq x \leq 1$) via hydroxide co-precipitation +annealing at 500 °C for 2 days

The diffusion coefficients calculated from the slope of the anodic peak current density plot above reveal a decreasing trend with the Ti0 sample displaying the highest diffusion co-efficient of all the samples. One has to keep in mind however while interpreting these values that these are apparent coefficients and are hence bound to be affected by the presence of secondary phases inside the material. In this case, it was already determined from XRD studies that the Ti0.5 and Ti1 samples had Li_2MnO_3

impurities accompanying the excess spinel phase. Even though the Li_2MnO_3 is a lithium ion conducting phase, it would still show no electrochemical activity in the investigated voltage range. Moreover the presence of Li_2MnO_3 would result in a decrease in the number of contact points between the electrochemically active spinel and the electrolyte thus reducing diffusion rates of lithium. Hence the low diffusion coefficients could possibly be attributed to the presence a mixture of phases in the structure. Hence it is not possible to deduce a clear trend via this method and more advanced methods are required.

4.3.5 Ex-situ X-ray diffraction

In order to verify the causes for fading, ex-situ XRD was performed in order to understand if there were phase transformations and if so was titanium substitution controlling this. The cells subjected to cycling were opened inside a glovebox and the electrodes cleaned, washed and dried and taken for XRD. Initially the electrode was analysed as such but it was found that the intensity of the Al peak was too large that the background enveloped the peaks corresponding to the main phase/any other phases. Hence the active material was scraped off the electrode and subjected to XRD separately.

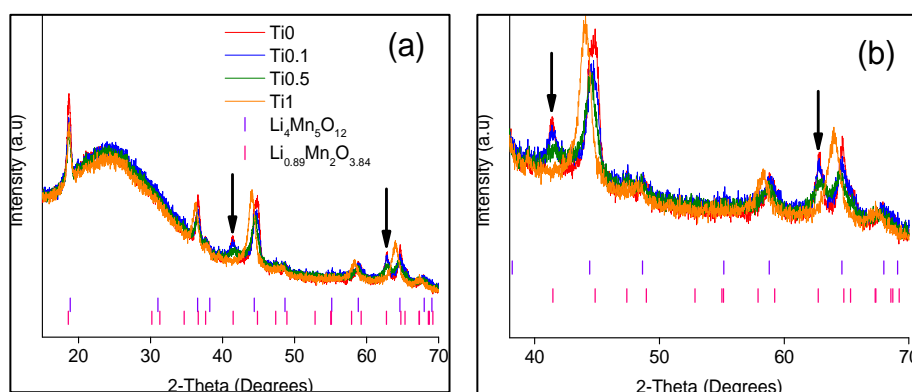


Figure 4.25 Ex-situ XRD after cycling, $\text{Li}_4\text{Ti}_x\text{Mn}_{5-x}\text{O}_{12}$ ($0 \leq x \leq 1$), fig b displays an enlarged section of the pattern in fig a, black arrows represent the tetragonal spinel phase.

A broad amorphous peak in the range of $20 - 30^\circ$ indicates the presence of acetylene black. However, the main peaks are clearly distinguishable. From the results it is clear that a phase transformation is occurring during cycling for the un-substituted excess spinel. New peaks corresponding to a tetragonal phase $\text{Li}_{0.89}\text{Mn}_2\text{O}_{3.84}$ (ICSD coll code: 50853) were observable in the unsubstituted spinel phase

The intensity of this peak decreased with increasing Ti content with the sample containing 1 mol of Ti displaying no tetragonal phase. Manthiram et.al. [1] had reported transformation during cycling to Li_2MnO_3 phase for spinel $\text{Li}_4\text{Mn}_5\text{O}_{12}$ and reported that as a reason for capacity fading. However a number of studies [23–25] have claimed that Li_2MnO_3 proves to be beneficial when integrated into the cubic structure in the form of nano domains. In this study, no transformation to Li_2MnO_3 was detected. In this study, we report a new previously unreported phase transformation as a reason for the capacity fading in un-substituted spinels.

4.4 Observations

4.4.1 Effect of nickel substitution in LiMn_2O_4

The effect of 0.5 mol nickel substitution for manganese in LiMn_2O_4 gives rise to the following observations from the results presented in the preceding sections.

- 0.5 mols of nickel was successfully substituted into LiMn_2O_4 via hydroxide co-precipitation synthesis method. Samples with varying particle sizes/degrees of crystallinity were prepared for both un-substituted and substituted spinels. Structural characterization revealed pure phases were obtained. Spinel LNM crystallized in a disordered structure with $Fd\bar{3}m$ space group at lower synthesis temperatures while a mixture of ordered and disordered structures were observed with increasing temperature of synthesis.
- Nickel substitution in LiMn_2O_4 considerably improves electrochemical performance in the voltage range of 2.3 – 3.3V. Three effects are distinguishable from that of the un-substituted spinel phase in the electrochemical performance. First, the number of mols of lithium inserted increases resulting in higher capacity (145 mAh.g^{-1} for spinel LNM compared to 130 mAh.g^{-1}). Second, the rate performance is improved significantly (75 mAh.g^{-1} at 4C for spinel LNM compared to 30 mAh.g^{-1} for spinel LMO). Finally capacity retention is much better (84 % for LNM vs 53 % for LMO). The improved rate performance for the nickel substituted spinel could be attributed to reduced charge transfer resistance as well as lower impedance to the movement of lithium ions within the structure from cyclic voltammetry and impedance analyses. The differences in performance between different LNM samples was possibly due to the differences in the nature

of space group for the samples synthesized at different temperatures and effects related to particle size.

- The galvanostatic cycling performance in the voltage range 2.3 – 3.3V displays a behaviour that is completely opposite to performance in the 4 and 5 V ranges. Materials annealed at a lower temperature display the highest capacity and rate performance in the 2.3 – 3.3V while materials synthesized at elevated temperatures perform better in the 4 and 5V regions. This effect of synthesis temperature on performance and a comparison with un-substituted material synthesized under similar conditions has not been reported before.
- Ex-situ XRD analysis revealed that spinel LMO undergoes phase transformation during cycling when annealed at elevated temperatures. Nickel substitution seems to avoid this phase transformation at all synthesis temperatures.
- There is still some fading occurring even in the best performing spinel LNM sample. This could possibly be due to manganese dissolution which requires to be tackled via other methods such as coatings, additives such as acid scavengers etc.

4.4.2 Effect of titanium substitution in $\text{Li}_4\text{Mn}_5\text{O}_{12}$

From the results of Ti substitutions, the following observations could be summarized.

- Different amounts of titanium up to 1 mol were successfully substituted into the $\text{Li}_4\text{Mn}_5\text{O}_{12}$ structure via hydroxide co-precipitation technique. In the samples synthesized via hydroxide co-precipitation method, Li_2MnO_3 phase was observed to form with increasing Ti content. Its amount increased with increasing Ti content up to 15 % in the sample with 1 mol Ti substituted for Mn. A cation mixed spinel phase was also observed in the un-substituted sample, but its amount was less than 5 %.
- 0.1 mol Ti substitution improved capacity retention marginally by about 10 % over 50 cycles and displayed slightly better rate performance compared to the unsubstituted spinel. For Ti contents greater than 0.1 mol, the capacity obtained decreases though the capacity retention is higher than the un-substituted counterpart over 50 cycles.
- Cyclic voltammetry reveals that diffusion co-efficient is reduced for titanium substituted spinels compared to un-substituted sample. This is reflected in the poorer rate performance of the spinels containing titanium.

- Ex-situ XRD analysis revealed that transformation to a tetragonal spinel phase during cycling was found to be the reason for capacity fading. The presence of Ti seems to suppress this transformation. However, in spite of the suppression, titanium substitution does not seem to improve electrochemical performance significantly.

4.5 Conclusions

In this chapter the effect of elemental substitutions on electrochemical performance was evaluated for 2 different spinel compounds namely LiMn_2O_4 and $\text{Li}_4\text{Mn}_5\text{O}_{12}$. Hydroxide co-precipitation method was employed to synthesize substituted samples. Nickel substitution was found to prevent phase transformation to tetragonal phases during cycling in the 2.3 – 3.3V suggesting the effect of Jahn-Teller distortion is avoided by the presence of nickel in the structure. Spinel LNM and LMO prepared at different temperatures were investigated and it was found that synthesis temperature affected performance significantly in different voltage ranges as evidenced by cycling data obtained in 2.3 – 3.3V and 3.5 – 5V ranges. The reason for this difference in performance most likely arises from the size of particles or the effect of space group. Titanium substitution also resulted in a reduction of the phase transformation to a tetragonal phase during cycling. However capacity obtained seemed to decrease with increasing titanium contents

Between the nickel substituted spinel and titanium substituted spinel, both display similar initial capacities ($\sim 145 \text{ mAh.g}^{-1}$) and rate performance ($\sim 75 \text{ mAh.g}^{-1}$ at 4C rate) and capacity retention (83% for spinel LNM compared to 87% for titanium substituted spinel). In fact the titanium substituted spinel displays much better rate performance at higher rates (6C and 8C). However the synthesis procedure is relatively more complex for the titanium substituted spinel requiring longer annealing times and the presence of oxygen atmospheres. Moreover, spinel LNM displays two useful voltage ranges (2.3 – 3.3 V and 3.5 – 5V) both of which can be exploited in energy storage applications. Hence the subsequent chapters will focus on improving the rate performance of the spinel LNM and understanding the reasons for the difference in electrochemical performance for samples synthesized at different temperatures.

References

- [1] W. Choi, a Manthiram, *Solid State Ionics*. 178 (2007) 1541–1545.
- [2] T. Takada, H. Hayakawa, E. Akiba, *J. Solid State Chem.* 115 (1995) 420–426.
- [3] T. Takada, H. Hayakawa, E. Akiba, F. Izumi, B.C. Chakoumakos, *J. Power Sources*. 68 (1997) 613–617.
- [4] Kuthanapillil M. Shaju and Peter G. Bruce, *Dalton Trans.* (2008) 5471 – 5475.
- [5] M. Kunduraci, G.G. Amatucci, *ECS Transactions*. 3 (2007) 165–170.
- [6] L. Wang, H. Li, X. Huang, E. Baudrin, *Solid State Ionics*. 193 (2011) 32–38.
- [7] M. Kunduraci, G.G. Amatucci, *J. Electrochem. Soc.* 153 (2006) A1345.
- [8] C.M. Julien, M. Massot, *Mater. Sci. Eng. B97* (2003) 217–230.
- [9] J. Xiao, X. Chen, P. V Sushko, M.L. Sushko, L. Kovarik, J. Feng, et al., *Adv. Mater.* 24 (2012) 2109–16.
- [10] X.Y. Feng, C. Shen, X. Fang, C.H. Chen, *J. Alloys Compd.* 509 (2011) 3623–3626.
- [11] Q. Zhang, E. Uchaker, S.L. Candelaria, G. Cao, *Chem. Soc. Rev.* 42 (2013) 3127–71.
- [12] M.M. Thackeray, M.F. Mansuetto, J.B. Bates, *J. Power Sources*. 68 (1997) 153–158.
- [13] K. Amine, K. Amine, H. Tukamoto, H. Tukamoto, H. Yasuda, H. Yasuda, et al., *J. Electrochem. Soc.* 143 (1996) 1607–1613.
- [14] D. Aurbach, *J. Electrochem. Soc.* 145 (1998) 3024.
- [15] S.S. Zhang, K. Xu, T.R. Jow, *Electrochim. Acta*. 49 (2004) 1057–1061.
- [16] D. Aurbach, M.D. Levi, K. Gamulski, B. Markovsky, G. Salitra, E. Levi, et al., *J. Power Sources*. 81 - 82 (1999) 472–479.
- [17] S.H. Kang, J.B. Goodenough, L.K. Rabenberg, *Chem. Mater.* 13 (2001) 1758–1764.
- [18] S.-H. Kang, J.B. Goodenough, *J. Electrochem. Soc.* 147 (2000) 3621 – 3627.
- [19] K. Amine, H. Tukamoto, H. Yasuda, Y. Fujita, *J. Power Sources*. 504 (1997) 604–608.

- [20] M.M. Thackeray, Y. Shao-Horn, A.J. Kahaian, K.D. Kepler, E. Skinner, J.T. Vaughey, et al., *Electrochem. Solid-State Lett.* 1 (1998) 7–9.
- [21] S.-H. Park, S.-W. Oh, C.-S. Yoon, S.-T. Myung, Y.-K. Sun, *Electrochem. Solid-State Lett.* 8 (2005) A163.
- [22] T. Takada, H. Enoki, H. Hayakawa, E. Akiba, *J. Solid State Chem.* 139 (1998) 290–298.
- [23] C.S. Johnson, N. Li, J.T. Vaughey, S. a. Hackney, M.M. Thackeray, *Electrochem. Commun.* 7 (2005) 528–536.
- [24] Y. Li, Y. Makita, Z. Lin, S. Lin, N. Nagaoka, X. Yang, *Solid State Ionics.* 196 (2011) 34–40.
- [25] S. Ivanova, E. Zhecheva, D. Nihtianova, M. Mladenov, R. Stoyanova, *J. Alloys Compd.* 561 (2013) 252–261.

Chapter 5

Influence of morphology and nano-structuring on performance

This chapter will discuss the effect of varying morphology on performance with an aim to enhance performance and understand the reason behind the variations in performance presented in the preceding chapter for spinel LNM. Spinel LNM is synthesized via different techniques and the electrochemical performance is evaluated for all the samples. It is found that spinel LNM synthesized via electrospinning displayed the best performance.

5.1 Introduction

From the preceding chapter, it is evident that nickel substitution seems to improve performance for the hydroxide co-precipitated spinels in the 2.3 – 3.3 V range. The improved performance can be attributed to the reduced charge transfer resistance and suppression of phase transformation to the tetragonal phases with nickel inside the structure. Annealing temperature had a significant effect on capacities obtained, rate performance and capacity retention during cycling. Spinel LNM_800_10h displayed the worst performance in the 2.3 – 3.3 V range while the same material offered the best performance in the 3.5 – 5 V range. Similarly LNM_500_3h displayed the worst performance in the 3.5 – 5V range while delivering the best performance in the 2.3 – 3.3 V range. That leaves us with another question. Why does a material with good crystallinity (LNM_800_10h) perform poorly in one voltage range (2.3 – 3.3V) while delivering the best performance in another voltage range (3.5 – 5V)? Could the reason be space group (LNM_800_10h seems to have a mixture of ordered and disordered phases present) or particle size? Before we can attribute the reason for the difference in performance to space group, one must eliminate particle size as a possible reason. For e.g, the LNM_500_10h displays the worst performance in the 3.5 – 5V range. This can be partly attributed to the significant electrolyte decomposition (1st cycle efficiency is about 58.8%) occurring due to the increased surface active area due to reduced particle size.

If the observed effects are indeed due to particle size, preparing samples of similar sizes (and morphology) should result in similar electrochemical performance. To verify this, the carbonate co-precipitation method was employed to synthesize the spinel LNM with a spherical morphology. The method would be ideal for preparing samples with similar particle sizes and morphology but varying degrees of crystallinity. As a by-product of this study, it would also be possible to investigate the effect of spherical morphology on the performance of these samples. The precursors employed include spherical MnO₂ particles synthesized via co-precipitation using manganese sulphate and ammonium bi-carbonate. This spherical MnO₂ is amorphous in nature and is employed as a precursor for the spinel LNM preparation together with lithium acetate and nickel nitrate hexahydrate. The detailed synthesis procedure is presented in the methods and materials section.

From the point of view of improving electrochemical performance of the spinel LNM in the 2.3-3.3V range, it was decided to employ nanostructuring. 1D nanofibers synthesised via single spinnerette electrospinning method were fabricated and evaluated for their electrochemical performance. For the sake of comparison, a standard sample is synthesized using a conventional solid state method with the same precursors employed for electrospinning as well. The following sections detail the structural and electrochemical evaluation of the various materials. As in the previous chapter, labels are employed for identification of samples. The spinel LNM synthesized via carbonate co-precipitation would be identified using LNMSPH_Temperature_Time while spinel LNM synthesized via electrospinning would be named as LNM-ES while the spinel synthesized via conventional solid state processing would be labelled as LNM-SS.

5.2 Experimental methods – LNM via carbonate co-precipitation

5.2.1 Powder X-ray diffraction

Figure 5.1 (a) presents the XRD patterns of the precursors at different stages of the carbonate co-precipitation method. MnCO_3 spheres having very good crystallinity are decomposed to form an amorphous MnO_2 phase on calcination at 400 °C for 5 hours. The amorphous MnO_2 is converted to a pure phase spinel LNM after mixing and calcining with the appropriate amounts of lithium and nickel precursors.

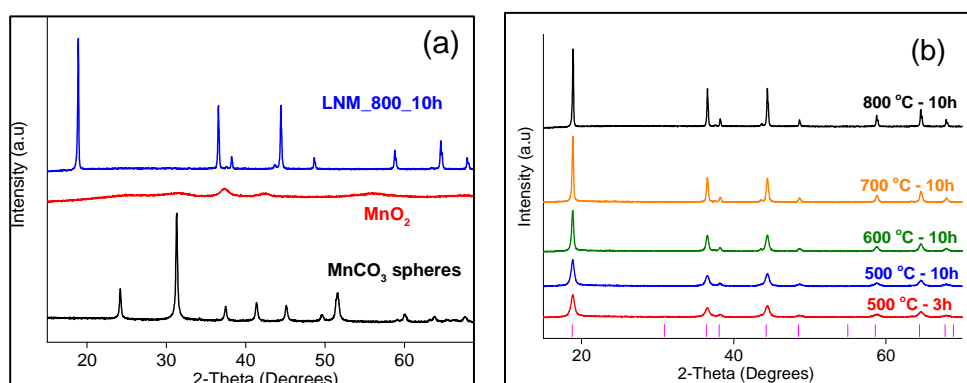


Figure 5.1 XRD patterns of (a) Precursors (b) LNM spheres synthesized at different temperatures.

Figure 5.1 (b) reveals diffraction peaks corresponding to LNM spinel obtained at different annealing temperatures. Impurity peaks corresponding to $\text{Li}_x\text{Ni}_{1-x}\text{O}$ observable in case of samples annealed at 700 °C and 800 °C for 10 hours. The

increasing peak intensity for the (110) plane is proof for the increasing crystallinity with temperature of annealing. The observed patterns could be indexed to a cubic spinel with $Fd\bar{3}m$ space group (ICSD Coll code: 90650). The lattice parameters obtained from Rietveld refinement were in the range of 8.1621 (4) – 8.1675 (12) for the different samples matching well with literature values. However FTIR studies would be performed to establish the space group as in the previous case with hydroxide co-precipitated spinels.

5.2.2 Scanning electron microscopy

Secondary electron images (figure 5.2, a - j) reveal that all the samples are composed of spherical particles with diameters in the range of 3 – 10 μm . They are also accompanied by broken fragments of the spheres presumably coming from the explosive nature of the reaction between lithium acetate and nickel nitrate. This would be a combustion reaction with lithium acetate acting as fuel and nickel nitrate acting as an oxidizer with the temperature of the furnace supplying the heat required for combustion. Since these fragments would be formed during the 1st calcination step (500 °C – 3h) itself, it can be reasonably assumed that the remaining annealing steps would not result in any further destruction and might probably result only in fusion of the broken fragments increasing temperature. For example, comparison of figure 5.2b/f with 5.2j clearly reveals this difference. It can also be observed from the SEM images that the morphology becomes smoother with increasing annealing temperature. This as mentioned earlier could be due to the fact that diffusion processes are activated inside the material that leads to mass transfer ultimately resulting in a smoother morphology. EDX analysis revealed the mass ratio between Ni and Mn to be 0.340 which is slightly lesser than the expected value of 0.350.

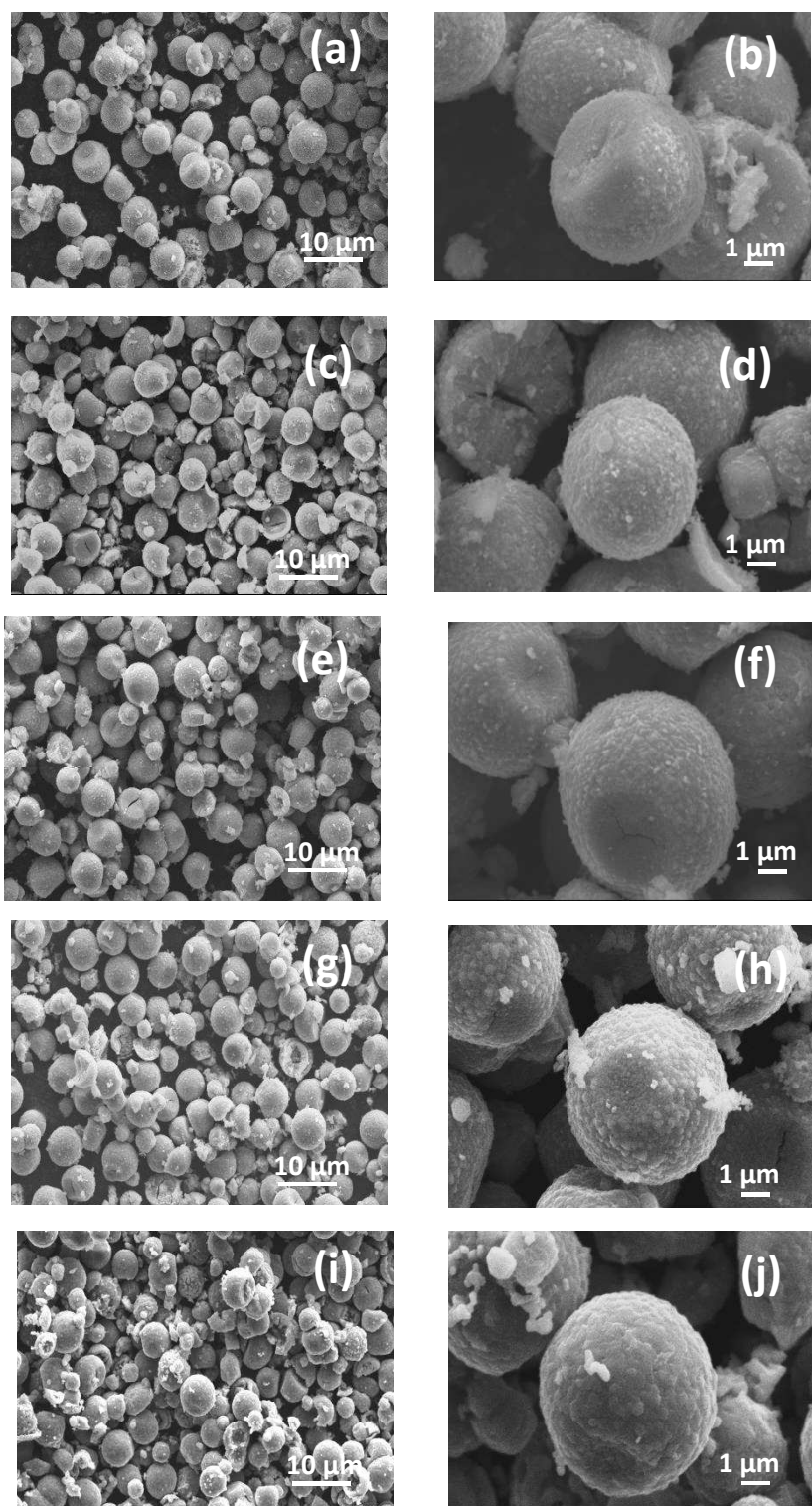


Figure 5.2 SEI of spherical LNM synthesized via carbonate co-precipitation method (a & b – 500 °C -3h), (c&d – 500 °C -10h), (e&f – 600 °C -10h), (g&h – 700 °C -10h), (i & j – 800°C -10h)

5.2.3 Fourier Transform Infrared spectroscopy

To identify the space group of the LNM spinel, FTIR spectra were recorded in the range of 400 – 4000 cm^{-1} and analysed. The results are provided in figure 5.3.

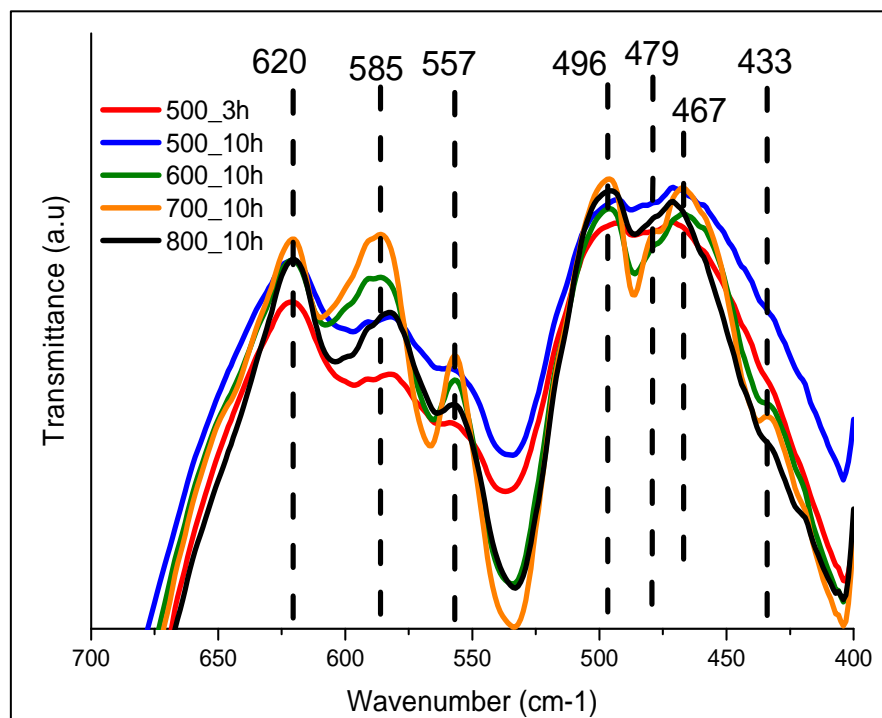


Figure 5.3 FTIR spectra of spherical LNM synthesised at different temperatures via carbonate co-precipitation

The trend of space groups seemed to evolve in a manner similar to that of hydroxide co-precipitated spinels. LNMSPH_500_3h and LNMSPH_500_10h display broad peaks at 557 and 585 cm^{-1} typical of an $Fd\bar{3}m$ space group. On increasing the temperature, the two peaks become sharper indicating the formation of an ordered phase with $P4_332$ space group. The peaks are very well defined for the LNMSPH_700_10h and become broad again for LNMSPH_800_10h suggesting that the amount of ordered phase is perhaps the highest in the 700 °C annealed sample. None of the patterns could however be matched to the exact reported pattern for the ordered space group [1,2] and hence the possibility of a mixture of the two space groups being present cannot be ruled out. The trend exactly reflects the same trend observed for hydroxide co-precipitated spinels. To conclude, it can be said that the LNMSPH_500_3h and LNMSPH_500_10h crystallize in an $Fd\bar{3}m$ structure while the remaining samples consist of a mixture of both $Fd\bar{3}m$ and $P4_332$ space groups.

5.2.4 Thermal Analysis

Thermogravimetric analysis was performed for the synthesized spinels and the results are presented in figure 5.4

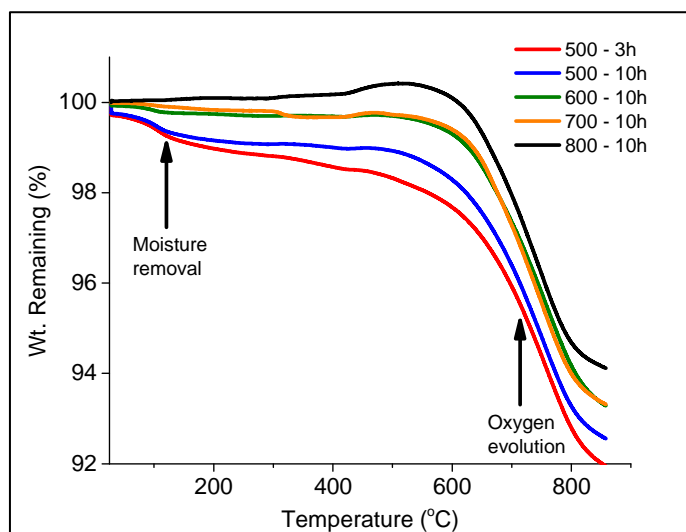


Figure 5.4 TGA curves of spherical LNM synthesised via carbonate co-precipitation

Two distinct weight loss regions can be observed. First corresponds to the removal of adsorbed moisture in the samples at around 95 – 120 °C. This loss is higher for samples synthesised at a lower temperature (0.6 %) compared to samples synthesized at higher temperatures (almost no weight loss). The second loss which seems to set in around 450 °C involves the loss of oxygen from the structure. The total weight loss due to oxygen ranges from 6.3 – 6.4 % for all the samples suggesting that the initial phase composition of the different samples was probably not very different to start with. This trend is again similar to the trend for hydroxide co-precipitated spinels. Thus considered together with XRD and FTIR analyses, it is concluded that the major phase present is a cubic structure with $Fd\bar{3}m$ space group.

5.2.5 Cyclic voltammetry and galvanostatic cycling

Cyclic voltammograms in the voltage range of 2.3 – 3.3V (figure 5.5a) reveals a reversible redox process ($Mn^{3+} \leftrightarrow Mn^{4+}$ couple) for all the samples. With increasing annealing temperature, the current obtained during the redox process decreases mirroring the trend reflected by hydroxide co-precipitated spinels.

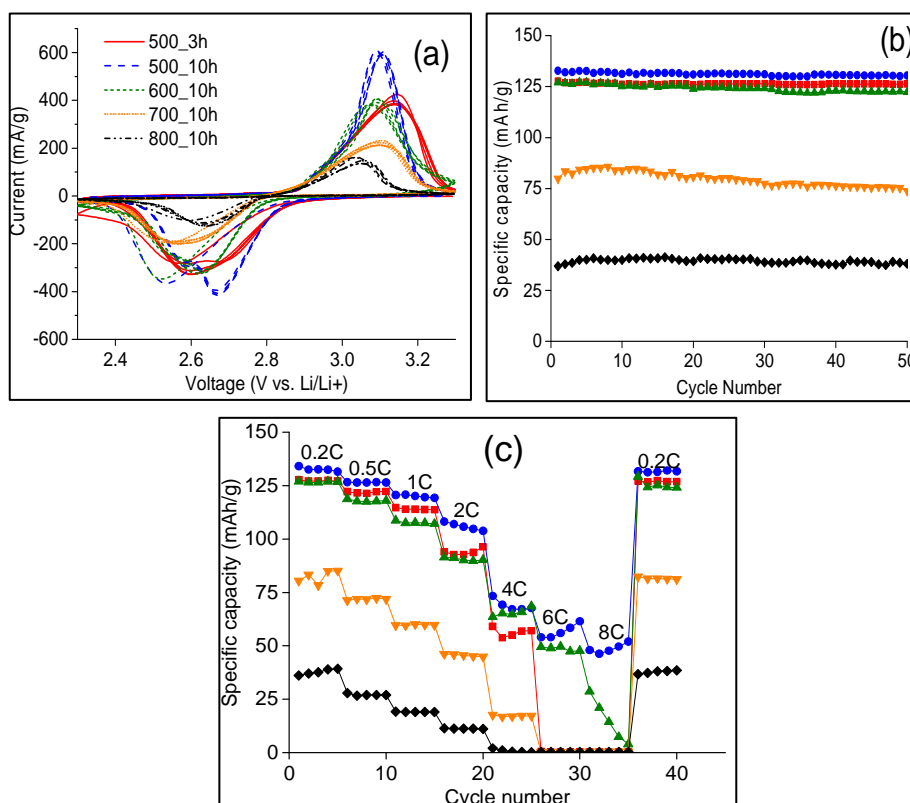


Figure 5.5 Electrochemical performance of spherical LNM in 2.3 – 3.3V (a) CV curves @ 0.2 mV/s, (b) Cycling performance at 30 mA.g⁻¹ (0.2C) (c) Rate capability

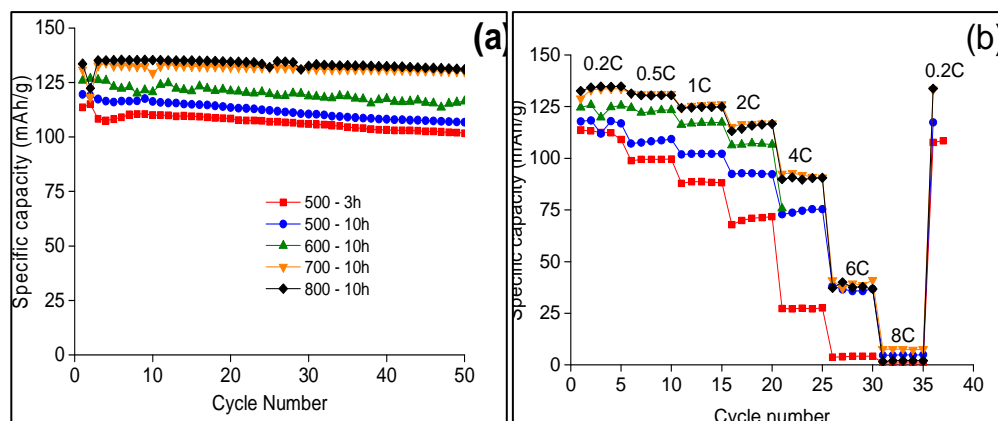


Figure 5.6 Electrochemical performance of spherical LNM in 3.5 – 5V (a) Cycling performance at 30 mA.g⁻¹ (0.2C) (b) Rate capability.

This is also reflected in the galvanostatic testing (figure 5.5b) in which LNMSPH_500_3h, LNMSPH_500_10h and LNM_600_10h samples deliver the highest initial capacities (127, 132 and 126 mAh.g⁻¹ respectively). Capacity retention is quite good for all these 3 samples (about 99% of initial capacity after 50 cycles respectively). LNMSPH_800_10h displays the lowest capacity at 40 mAh.g⁻¹ but

delivers the same value after 50 cycles roughly. In the rate tests (figure 5.5c), LNMSPH_500_10h displays the best performance with a capacity of 46 mAh.g^{-1} at 8C. All other samples calcined at higher temperatures reveal poor performance at C-rates higher than 2C. All the samples display good retention after high rate cycling suggesting that there are no structural changes occurring after high rate cycling.

Table 5.1 Initial capacities and retention for spherical LNM synthesized via carbonate co-precipitate method, error is around $\pm 5 \text{ mAh.g}^{-1}$.

Sample	1 st cycle charge capacity (mAh.g ⁻¹)	1 st cycle discharge capacity (mAh.g ⁻¹)	50 th cycle discharge capacity (mAh.g ⁻¹)	% capacity retention
2.3 – 3.3 V				
500 -3h	127.6	131.7	124.1	94.2
500 – 10h	132.8	136.3	128.2	94.1
600 – 10h	127.0	130.0	121.1	93.2
700 – 10h	79.8	70.1	73.8	92.5
800 – 10h	36.9	40.4	38.0	94.1
3.5 – 5 V				
500 -3h	150.6	113.6	101.7	89.5
500 – 10h	150.0	119.6	106.8	89.3
600 – 10h	149.8	125.9	116.4	92.5
700 – 10h	145.6	130.8	130.0	99.4
800 – 10h	144.0	133.6	131.0	98.1

Galvanostatic cycling performance in the 3.5 – 5V region (figure 5.6a) reveals that LNMSPH_800_10h delivers the highest initial discharge capacity of 133 mAh.g^{-1} retaining about 98% over 50 cycles. LNMSPH_500_10h on the other hand displays the lowest initial capacity (114 mAh.g^{-1}) and retention (90%). The capacity retention increases with increasing temperature. LNMSPH_800_10h also displays the best rate

performance (figure 5.6b) as well delivering a capacity of roughly 90 mAh.g^{-1} at 4C rate. However the capacity drops off at higher rates (6C and 8C). It is also noted that lower annealing temperatures resulted in increased electrolyte decomposition during charging (observed both in cyclic voltammetry and galvanostatic cycling) similar to the observations for hydroxide co-precipitated spinels. Increasing annealing temperatures result in better performance in the voltage range of 3.5 – 5V vs. Li/Li^+ .

To sum up, the general trends in electrochemical performance with temperature seem to mirror that of the different spinel LNM samples synthesized via hydroxide co-precipitation method with few exceptions. The first exception is that the stability during the initial 10 cycles for the spherical LNM is much more improved in the 2.3 – 3.3V region compared with the hydroxide co-precipitated LNM. Secondly, the 1st charge capacities obtained during galvanostatic cycling in the 3.5 – 5V region do not exceed the theoretical value by a lot indicating that the extent of electrolyte decomposition observed is very less compared to that of hydroxide co-precipitated spinels in the same voltage range.

5.2.6 Cyclic voltammetry at different rates

To establish the diffusion behaviour, the different spinel LNM electrodes were subjected to cyclic voltammetry at different rates and the apparent diffusion coefficients results were estimated using the Randles-Sevcik equation. The results are presented in table 5.2.

Table 5.2 Comparison of lithium diffusion co-efficients, spinels synthesized via two different co-precipitation methods

Annealing condition	Lithium diffusion coefficient (cm^2/s)	
	Hydroxide co-precipitation	Carbonate co-precipitation
500_3h	1.345×10^{-10}	1.379×10^{-10}
500_10h	0.847×10^{-10}	2.227×10^{-10}
600_10h	0.605×10^{-10}	1.185×10^{-10}
700_10h	0.441×10^{-10}	0.697×10^{-10}
800_10h	0.177×10^{-10}	-

For the spinel LNM synthesized via hydroxide co-precipitation, a clear trend of reducing lithium diffusion coefficients is observed whereas for the carbonate co-precipitation samples, the variation is not significant. It was already mentioned in the preceding discussion that the coefficient value obtained here is an apparent value (see section 5.1.1). The presence of approximately similar sized particles would thus give rise to almost similar apparent diffusion coefficients. The trend further corresponds well with the galvanostatic testing results where the LNMSPH_500_10h sample displayed the highest capacity and best rate performance. It would then be reasonable to assume that the differences that are evident in the performance here can be attributed to the structural differences in the samples mainly rather than particle size.

5.3 Experimental methods – spinel LNM via electrospinning and solid state method

5.3.1 Powder X-ray diffraction

The results of the Rietveld refinement of the patterns for LNM-SS and LNM-ES are presented in figure 5.7a and 5.7b respectively.

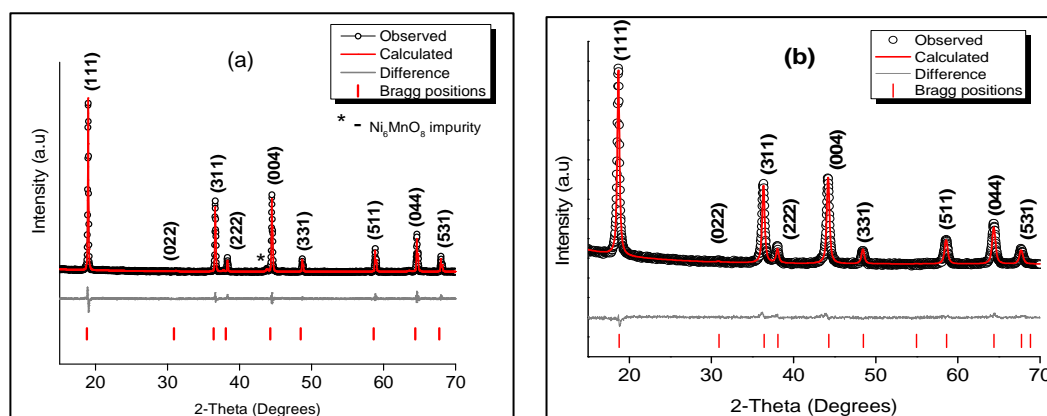


Figure 5.7 Powder XRD patterns (a) LNM-SS (b) LNM-ES, patterns subjected to refinement.

In the case of the LNM-SS synthesized here, the obtained pattern could be indexed to a cubic spinel structure with an $Fd\bar{3}m$ space group (ICSD Coll Code: 90650). The lattice parameter obtained from rietveld refinements ($R_{\text{exp}} = 2.48$, $R_{\text{wp}} = 3.06$, $R_p = 2.32$, $\text{GOF} = 1.23$) was $a = 8.176(3) \text{ \AA}$ which is in line with reported values for the disordered compound. A minor impurity phase of Ni_6MnO_8 is observed which is commonly observed in this method. The XRD patterns obtained for the LNM-ES powder could also be indexed to a cubic spinel structure with disorder. Lattice parameter values calculated from rietveld refinement was found to be $a = 8.176(3) \text{ \AA}$.

R-factors for refinement were $R_{\text{exp}} - 1.14$, $R_{\text{wp}} - 1.59$, $R_p - 1.21$, GOF- 1.40 suggesting good fitting of the experimental data to the structural model.

5.3.2 Electron microscopy

Secondary electron images of the LNM-ES and LNM-SS samples analysed through scanning electron microscopy is presented in figure 5.8 (a-c, f).

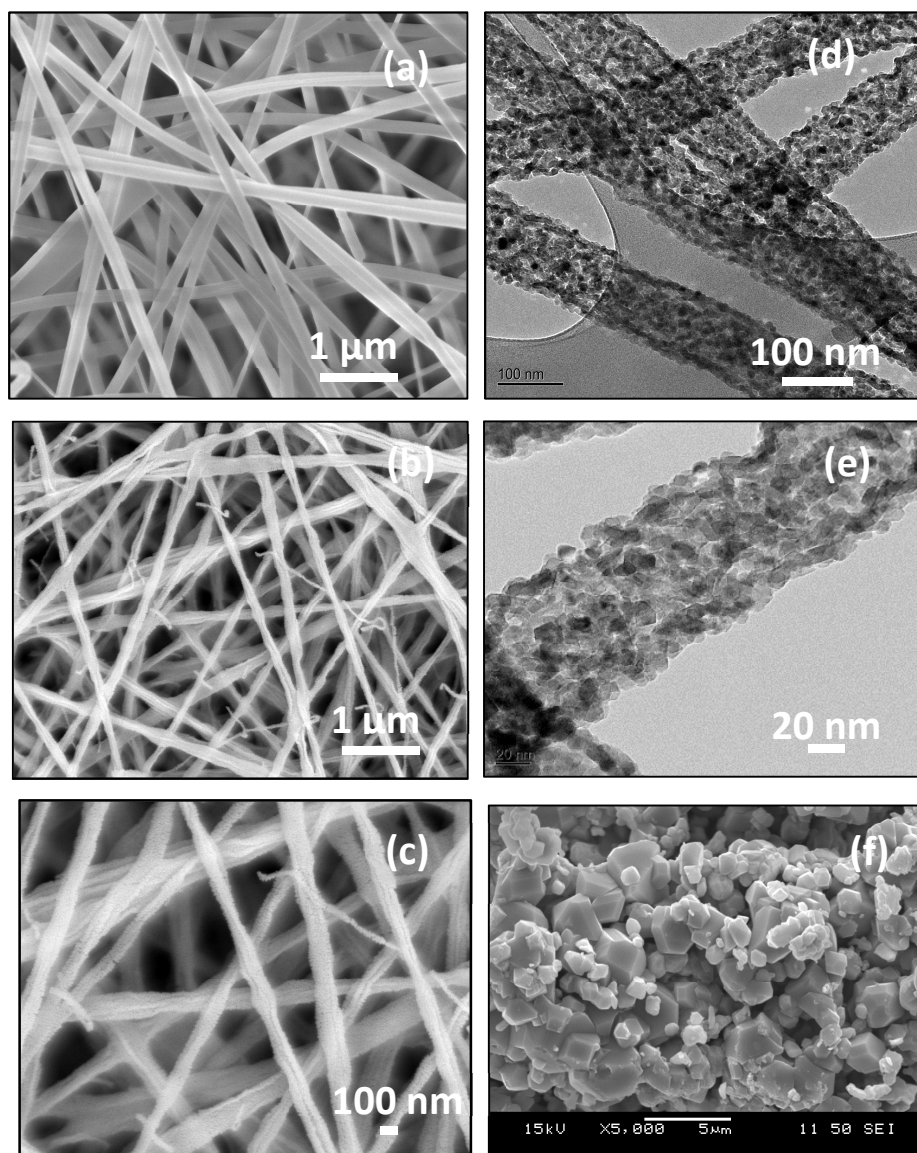


Figure 5.8 Electron micrographs of LNM-ES and LNM-SS, SEI of (a) As-spun fibres, (b,c) calcined fibres, TEI of calcined fibre (d, e), (f)SEI of LNM-SS sample.

The LNM-SS sample (figure 5.8f) reveals an irregular morphology with particles in the size range of 1 – 5 μm . They also reveal well defined octahedral facets which is typical for this material. For the LNM-ES sample, a field emission scanning electron

microscopy was employed to obtain secondary electron images. The as-spun fibres (figure 5.8a) have a smooth morphology without the appearance of beads suggesting the spinning conditions employed are resulting in good quality fibres. The diameter of the as-spun fibres ranges from 200 – 400 nm.

After calcination, the fibres lose their smooth morphology which is now replaced by a rougher surface. The fibre structure is preserved suggesting that the employed calcination conditions have not destroyed the morphology which is essential for realizing novel properties. The diameter of the fibres have reduced to 100 -200 nm after calcination. This is expected to occur due to the removal of the organic component of the fibres. Transmission electron images reveals that the fibres are made up of nanosized crystallites 25 – 35 nm in size fused together to form the long fibrous structure. Furthermore, pores can also be observed indicating the porous nature of these fibres. These can be attributed to the gases escaping during calcination of the polymeric backbone.

5.3.3 Thermal analysis

TGA was employed to determine the carbon content of the LNM-ES fibres formed after calcination. The powders were subjected to characterization via XRD, SEM and raman spectroscopy to analyse the crystallinity, phase purity and morphology. Figure 5.9 presents the TGA curves of as-spun and calcined fibres in a mixture of synthetic air to simulate ambient conditions during calcination.

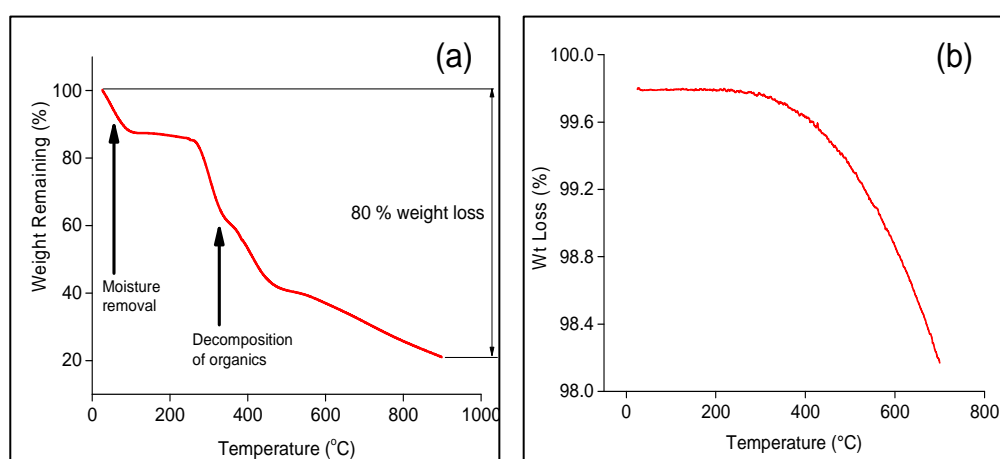


Figure 5.9 TGA curves of LNM-ES (a) As-spun fibres (b) Calcined fibres (600 °C for 1h)

The TGA curves of the as-spun fibres reveal a weight loss of about 80% which is in line with expected results (79.2 % for the total mass of precursors taken). The main loss occurs due to decomposition of the organic components present such as PVP, the acetate chains etc. To find out if there was any residual carbon leftover in the samples after calcination, a post calcination TGA was also performed (figure 5.9b) which shows a weight loss of less than 1.6 % clearly suggesting no residual carbon is present.

5.3.4 Fourier Transform Infrared spectroscopy

FTIR was performed to verify the space group of the LNM-ES and LNM-SS samples synthesized. The spectra are presented in figure 5.10

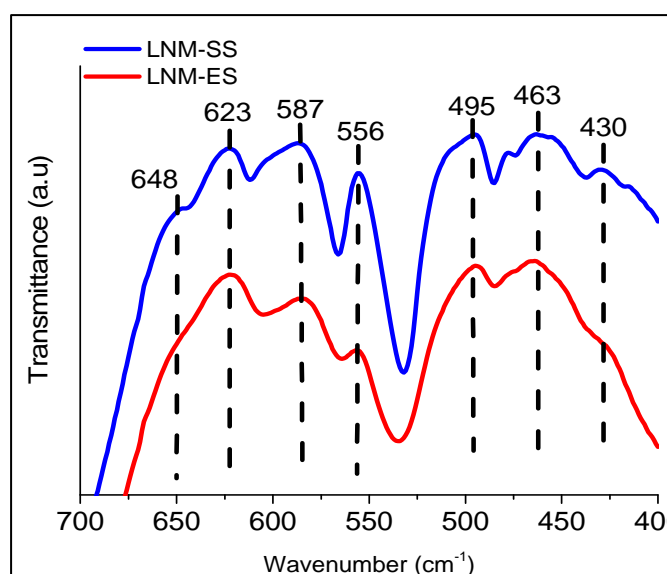


Figure 5.10 FTIR spectra of LNM-ES and LNM-SS samples.

The spectra reveal that LNM-ES consists of an $Fd\bar{3}m$ space group while the LNM-SS sample displays a combination of both $Fd\bar{3}m$ and $P4_332$ space groups. Together with XRD analysis, once again the major phase seems to be the both $Fd\bar{3}m$ space group in both samples.

5.3.5 Cyclic voltammetry and galvanostatic cycling

This section will present the results of electrochemical testing of both LNM-SS and LNM-ES. Initially the performance of the LNM-SS is presented followed by results for the LNM-ES sample. For both samples, investigations are performed in both voltage ranges (i.e 2.3 – 3.3V & 3.5 – 5V).

The cyclic voltammograms (figure 5.11a) recorded at a scan rate of 0.2 mV.s^{-1} in the 3.5 – 5V range reveal reduction and oxidation peaks located at 4.63 and 4.83 V respectively which correspond to the redox couple $\text{Ni}^{2+} \leftrightarrow \text{Ni}^{4+}$. A pair of redox peaks are also observed at around 4.01 V and 3.89 V. This suggests the presence of Mn^{3+} in the material indicating the presence of a disordered phase which correlates well with the results of XRD. The process seems reversible and no indications for fading are observable. The results of galvanostatic cycling in the high voltage range are given in figure 5.11(b & c).

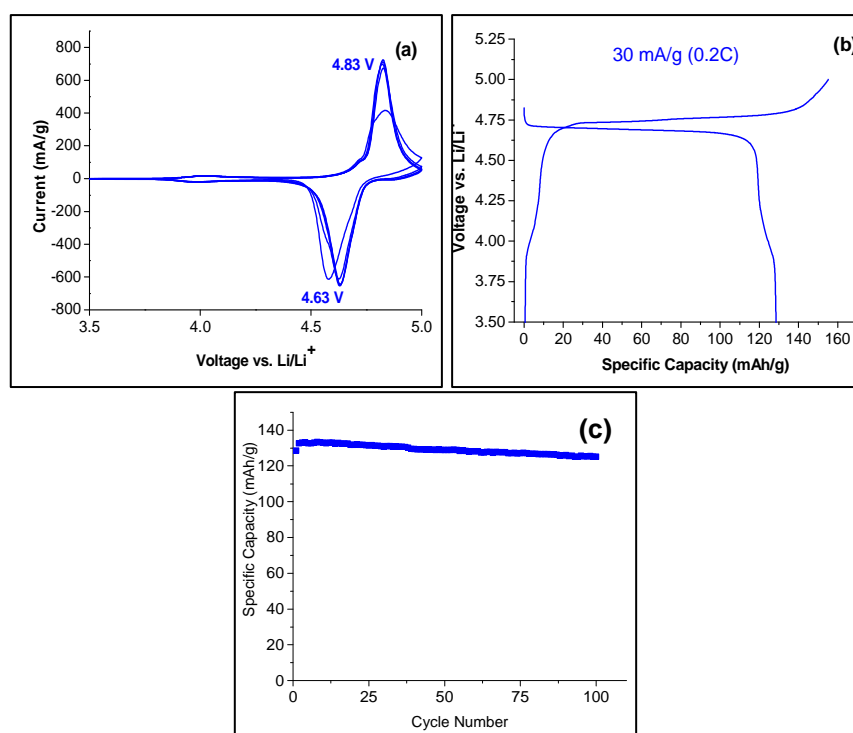


Figure 5.11 Electrochemical performance of LNM-SS in 3.5-5V (a) CV curves @ 0.2 mV.s^{-1} (b) first charge/discharge curve (c) cycling performance @ 30 mA.g^{-1} (0.2C)

The cycling was performed at a rate of 30 mA.g^{-1} ($\sim 0.2\text{C}$ assuming $1\text{C}=150 \text{ mA.g}^{-1}$). The observed capacity in the first cycle is 128.5 mAh.g^{-1} from the charge and discharge curves (figure 5.11b). About 7 % of this capacity can be ascribed to the $\text{Mn}^{3+}/\text{Mn}^{4+}$ redox couple. Figure 5.11c shows the superior performance during cycling displaying a capacity of 125 mAh.g^{-1} after 100 cycles which corresponds to 97 % retention of initial capacity.

The performance in the 3V region is presented in figure 5.12 (a - d). CV traces at 0.2 mV/s are given in figure 5.12a. Redox peaks are observed at 2.7 and 2.98 V indicating

a peak separation of about 0.3V. No other peaks are observed ruling out any other redox couples/side reactions in the system. Compared to the activity in the 5V region, the current obtained is about an order of magnitude smaller in this region. This indicates limited electrochemical activity in the 3V region. Galvanostatic cycling results (Fig 5.12b - d) further confirm this observation. A capacity of 49 mAh.g⁻¹ is delivered when LNM-SS is cycled at a 0.2C rate. This corresponds to the insertion of 0.33 mols of Li⁺ into the structure. About 0.31 mol of Li⁺ could be extracted back from the structure giving an efficiency of about 92.3 % for the first cycle. This value further decreases when the rate is increased to 1C (150 mA.g⁻¹). Only about 20 mAh.g⁻¹ capacity could be obtained suggesting there is virtually no significant activity in this region. Rate performance is also considerably poor as is evident with the capacity dropping to almost zero at high rates.

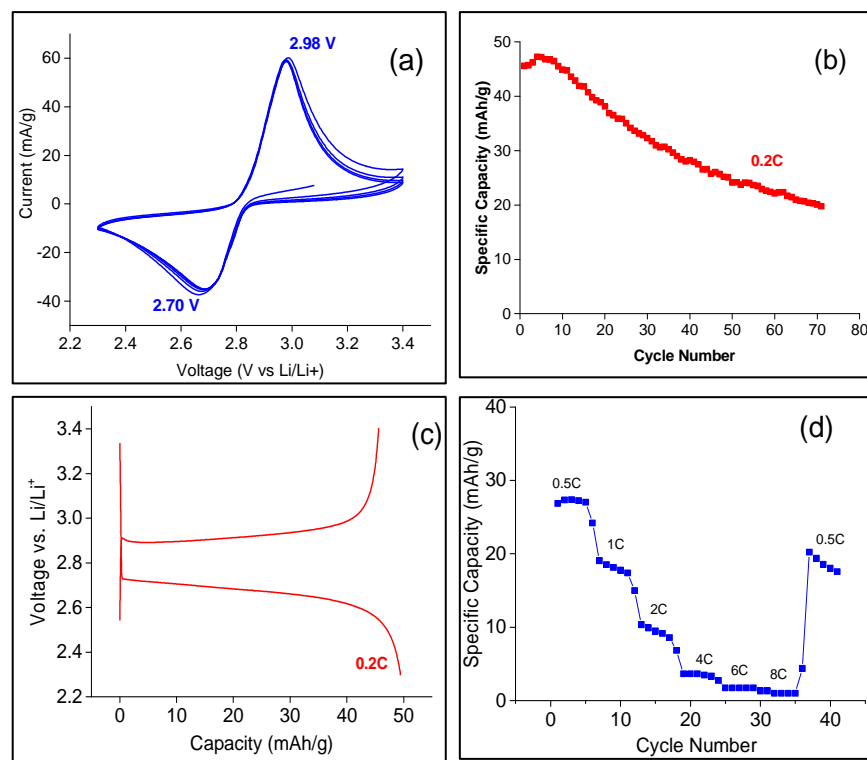


Figure 5.12 Electrochemical performance of LNM-SS in 2.3 - 3.3V (a) CV curves @ 0.2 mV.s⁻¹ (b) cycling performance at 30 mA.g⁻¹ (c) first charge/discharge curves (d) Rate performance.

The observed performance for LNM-SS in the 3.5 – 5V region is similar to the performance of the spinel LNM discussed in the chapter 4 (synthesized via hydroxide co-precipitation method and annealed at 800 °C for 10h). SEM analysis reveals micron

sized irregular particles for the LNM-SS while FTIR analyses show a combination of ordered and disordered phases existing in the material. From the charge – discharge curves, it is apparent that only 0.33 mols of Li^+ is being inserted into the structure. This would result in an average manganese valence of about +3.7. This is well above the average valence of +3.5 below which co-operative Jahn-Teller distortion usually sets in. This leaves open only the possibility of manganese dissolution being the major capacity fading mechanism and is always prevalent as long as there is Mn^{3+} present in the structure. The low observed capacity is arising due to some other structural effect probably arising from the presence of mixed phases.

The spinel LNM prepared by a single spinnerette electrospinning technique was evaluated in both the low voltage and high voltage ranges.

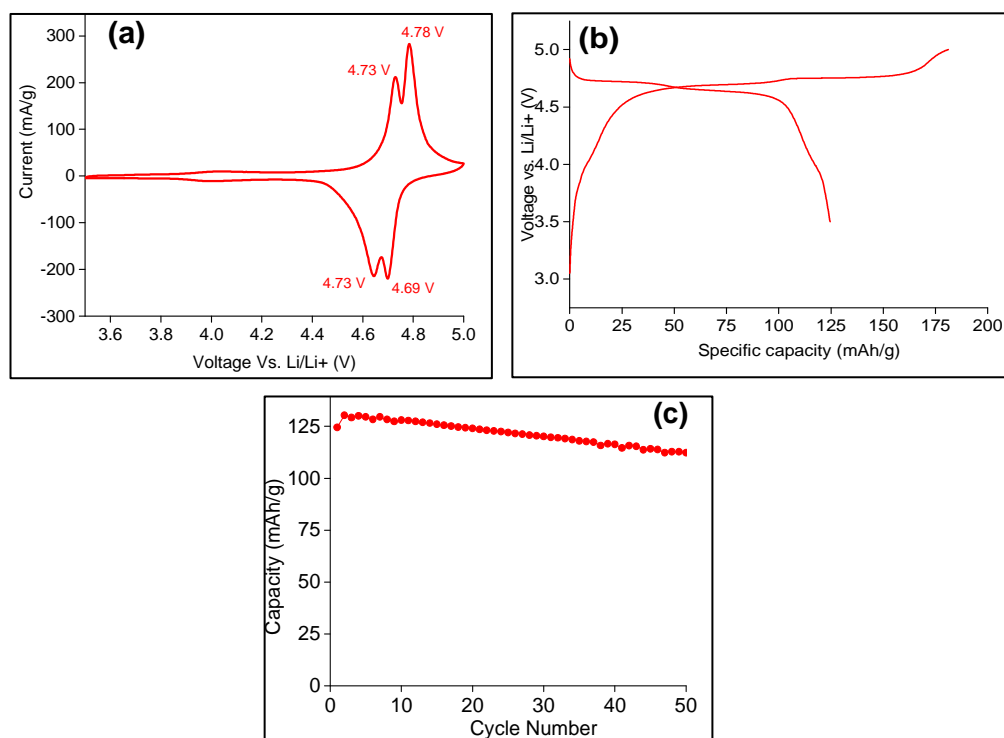


Figure 5.13 Electrochemical performance of LNM-ES in 3.5-5V (a) CV curves @ 0.2 mV.s^{-1} , (b) first charge\discharge curves (c) cycling performance @ 30 mA.g^{-1} .

CV traces (figure 5.13a) indicate a split in the peak positions. Two distinct peaks at 4.73 and 4.78 V corresponding to the oxidation of $\text{Ni}^{2+} \leftrightarrow \text{Ni}^{4+}$ and $\text{Ni}^{3+} \leftrightarrow \text{Ni}^{4+}$ reaction could be observed. Corresponding peaks at 4.64 and 4.70 V indicate the reduction of oxidised species. A small shoulder at 4V is observed which can be ascribed to the presence of Mn^{3+} in the structure. The charge – discharge curves are enumerated in figure 5.13b. The total capacity obtained in first charge is about 181 mAh.g^{-1} which is

higher than the theoretical capacity of 148 mAh.g^{-1} . This is probably expected since the redox (4.75V) potential lies outside the stability window of the EC: DEC solvent and the effect is accentuated by using a nanomaterial which has a high surface area thus presenting increased sites for electrolyte decomposition. The 1st discharge capacity is about 125 mAh.g^{-1} . About 11 % of this capacity can be attributed to the $\text{Mn}^{3+}/\text{Mn}^{4+}$ redox couple. The cycling performance (Fig 5.13c) reveals a gradual fading with about 90 % retained after 50 cycles indicating capacity retention is poorer than the solid state material.

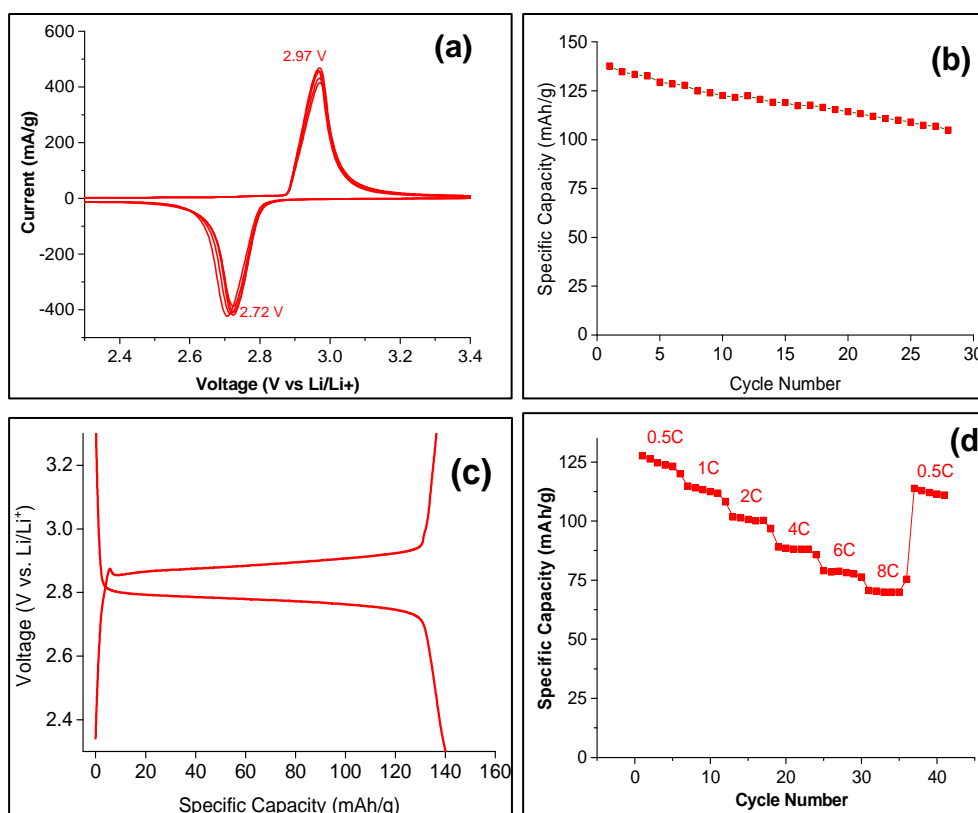


Figure 5.14 Electrochemical performance of LNM-ES in 2.3-3.3V (a) CV curves @ 0.2 mV.s^{-1} (b) cycling performance @ 30 mA.g^{-1} (c) first charge/discharge curve (d) Rate performance (Reproduced with permission from Elsevier)

The electrochemical performance of the LNM-ES materials in the 3V region is given in figure 5.14 (a-d). Cyclic voltammograms indicate that the current obtained is roughly about an order of magnitude higher for the LNM-ES (compared to LNM-SS) sample indicating a significantly better electrochemical response. The redox peaks at 2.72 and 2.97 V results in a separation of about 0.25V. The sample displays an initial capacity of approximately 140 mAh.g^{-1} at 0.2C rate. This capacity reduces to 105

mAh.g^{-1} after only 30 cycles suggesting the retention is not very significantly improved. The charge – discharge curves presented in figure 5.14c suggest a two phase topotactic reaction is occurring (as evidenced by the presence of a voltage plateau). A first cycle efficiency of 93.2 % is obtained and this value reaches about 100 % eventually indicating that there is no further loss of lithium or electrolyte decomposition occurring which will impact the long term performance of the cell. Rate performance testing (figure 5.14d) reveals that the LNM-ES samples can display capacities of nearly 70 mAh.g^{-1} at a rate of 8C (roughly 1 A.g^{-1}). Almost 90 % of the capacity is recoverable at 0.5C after testing at high rates indicating that the structural stability is preserved for the LNM-ES material even during high rate cycling.

To understand the reasons for the vastly different performances for LNM-SS and LNM-ES, it would again be necessary to delve into the morphological as well as structural differences. LNM-ES consists of nano-sized crystallites fused together to form an interconnected fibre. The thin nanofibers offer many significant advantages. Firstly, the contact area with the electrolyte is significantly improved resulting in high lithium diffusion rates from the active material to the electrolyte. Secondly, it is known that 1D nanofibrous materials can also act as ion conduction pathways thereby resulting in faster kinetics. Both these factors can explain the observed high rate performance for the LNM-ES. Both these factors are not available in LNM-SS possibly explaining the poor rate performance. Thirdly, the small crystallite size should enable the active material to withstand the stresses generated during Jahn-Teller distortion (especially at high rates). However from the observed performance, it is clear that there is significant fading for the active material when it is cycled at 0.2C rate. This is most likely arising out of manganese dissolution which is made worse by the high contact area between the active material and the electrolyte. It is also worth mentioning that the disordered phase itself has some Mn^{3+} as well which again would be susceptible to dissolution. This high contact area also poses problems for the LNM-ES when it is cycled in the 3.5 – 5V range where electrolyte decomposition is enhanced significantly. The benefits offered by LNM-ES in terms of electronic wiring, high contact surface area with electrolyte is not present for LNM-SS. However it still displays phenomenal cycling stability in the voltage range of 3.5 -5 V. This can be clearly attributed to the low particle size/surface area and minimal electrolyte decomposition associated with it.

To sum up, the performance of the LNM-ES sample in the voltage range of 2.3 – 3.3 V is vastly improved by nano-structuring. However the performance in the high voltage region is expected to be dominated by electrolyte decomposition in spite of the high capacity it delivers.

5.3.6 Cyclic voltammetry at different rates

The diffusion coefficients of the LNM-SS and LNM-ES samples were determined via cyclic voltammetry at different rates and the results are presented in figure 5.15. It is evident that the apparent diffusion co-efficient for the spinel LNM-ES is about an order higher than that of spinel LNM-SS. This is obviously arising from the much more increased contact between the electrolyte and active material and can explain the significant difference in rate performances between the two samples.

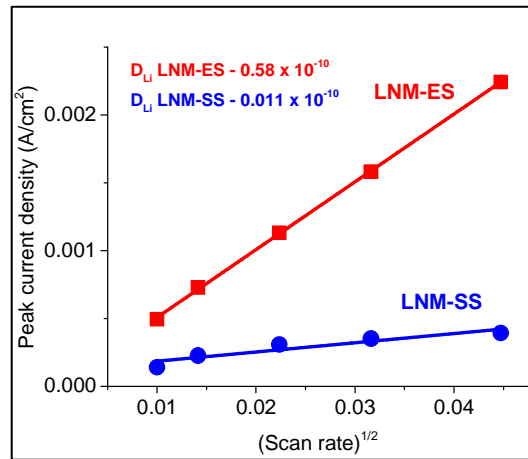


Figure 5.15 Peak current density vs scan rate for LNM-ES and LNM-SS, Anodic process (lithium insertion)

5.3.7 Electrochemical Impedance Spectroscopy

Impedance studies were performed to understand the kinetics of the reaction better. Figure 5.16 a & b present the Nyquist plots for the fresh cell and cells subjected to 20 cycles in the voltage range of 2.3 – 3.3V.

The data was fitted using the same equivalent circuit used earlier (section 4.2.6). It reveals that the charge transfer resistance (R_{ct}) for the LNM-ES sample is around 19.7 Ω for the fresh cell and barely increases to 20.7 Ω after 20 cycles. On the other hand, R_{ct} values for the LNM-SS after twenty cycles is about 7743 Ω . The R_{ct} value for the freshly assembled LNM-SS cell was even higher. The Warburg impedance for the LNM-ES sample is 29 $\Omega.s^{-(1/2)}$ compared to about 72 $\Omega.s^{-(1/2)}$ for the LNM-SS sample.

The lower charge transfer resistance coupled with the reduced Warburg impedance can explain the higher capacity and better rate performance for the LNM-ES sample.

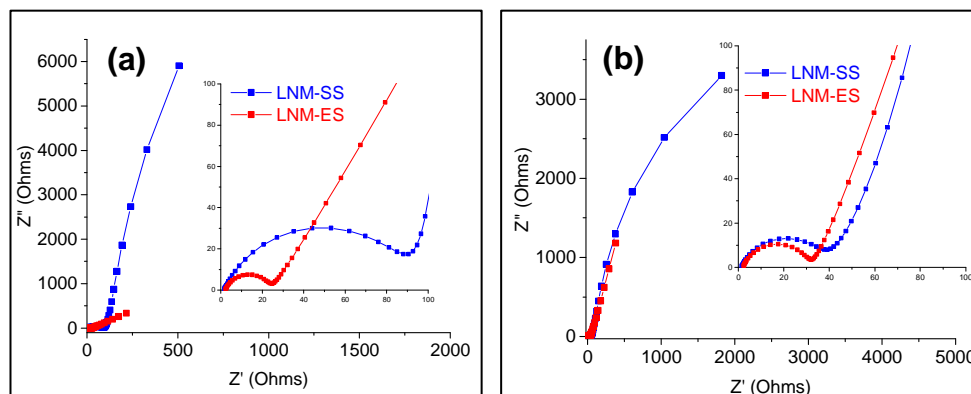


Figure 5.16 EIS analysis of LNM-ES and LNM-SS, (a) Fresh cells (b) after 20 cycles

5.4 Effect of spherical morphology on performance

The main aim behind the studies with carbonate co-precipitation was to determine if particle size was a reason for the observed performance. By preparing spherical particles with similar diameters and varying synthesis temperatures, samples with differing levels of crystallinity and content of phase groups were synthesized while fixing particle size. Hence whatever effects are observed in electrochemical performance are most likely arising due to the differences in the crystal structure arising due to space groups. It was observed that the overall trend remained similar to those of hydroxide co-precipitated samples. That is with increasing temperature of synthesis, performance in the 2.3 – 3.3V voltage range became worse while performance in the 3.5 – 5V voltage range became better. It can hence be concluded that performance seems to be affected more by the type of space group and its quantity rather than the particle size. Spherical morphology was found to have a positive effect on electrochemical performance. Particles with spherical morphology exhibited the most stable cycling performance in both the voltage ranges tested for spinel LNM. It is evident that the initial fading that occurs over 10 – 15 cycles for the spinel LNM synthesized via hydroxide co-precipitation is absent for the spherical LNM. Spherical morphology is known to accommodate stresses generated during repeated cycling compared to other irregular morphologies. This effect has also been well documented in literature for spinel LNM in the higher voltage range [3]. The spherical morphology also seems to result in relatively lesser electrolyte decomposition (as seen from 1st charge capacity) while cycling in the 3.5 – 5V range.

5.5 Effect of nano-structuring on performance

The second aim of this study was to investigate the effect of nanostructuring on performance for the spinel LNM. 3 key observations could be made here. Firstly, electrospun spinel LNM displayed improved performance in both the 3 and 5 V regions (in terms of obtaining higher capacity). Spinel LNM synthesized via a conventional method using the same precursors displayed poor performance in the 2.3 – 3.3V while displaying very good performance in the range of 3.5 – 5V. Secondly, in the voltage range of 2.3 – 3.3V, it was observed that there was capacity loss occurring for the electrospun LNM (10 % after 50 cycles) but the rate performance was significantly improved (70 mAh.g⁻¹ at 8C). By comparison, the spinels synthesized via hydroxide and carbonate co-precipitation displayed capacities of about 5 and 50 mAh.g⁻¹ respectively.

Overall, electrospun spinel LNM delivered higher capacities in both voltage ranges of testing unlike other materials which display better capacities but only in one of the voltage ranges. This suggests it would be possible to use it as a versatile electrode material in different energy storage devices.

5.6 Understanding of capacity fading mechanism

From the above discussion and the results in chapter 4, the following points emerge.

- i) The structure of spinel LNM varies considerably with synthesis temperatures resulting in a mixture of phase groups with increasing temperatures.
- ii) All spinel LNM samples (be it hydroxide co-precipitation/carbonate/conventionally synthesized samples) with a mixture of phase groups display poor capacities in the 2.3 – 3.3V voltage range.
- iii) Spherical LNM particles display much better cycling stability in the 1st 20 cycles when compared to spinel LNM synthesized via hydroxide method.
- iv) Lithium diffusion studies suggests that the particle size clearly affects the rate capability
- v) Nano-structuring to obtain 1D fibers of LNM results in the same material providing enhanced capacities in both the 2.3 – 3.3 and 3.5 – 5V ranges of testing which neither materials from hydroxide/carbonate co-precipitation/conventional synthesis deliver.

The crystal structures for the ordered and disordered spinel phases are given in figure 5.17. It is known that the disordered structure with $Fd\bar{3}m$ space group consists of Ni and Mn ions distributed randomly over the 16d octahedral sites while the lithium resides in the 8a tetrahedral sites. This arrangement is basically similar to the LiMn_2O_4 structure where only Mn ion is available. On the other hand, the ordered structure with $P4_332$ space group consists of Ni and Mn ions distributed over 4b and 12d octahedral sites respectively.

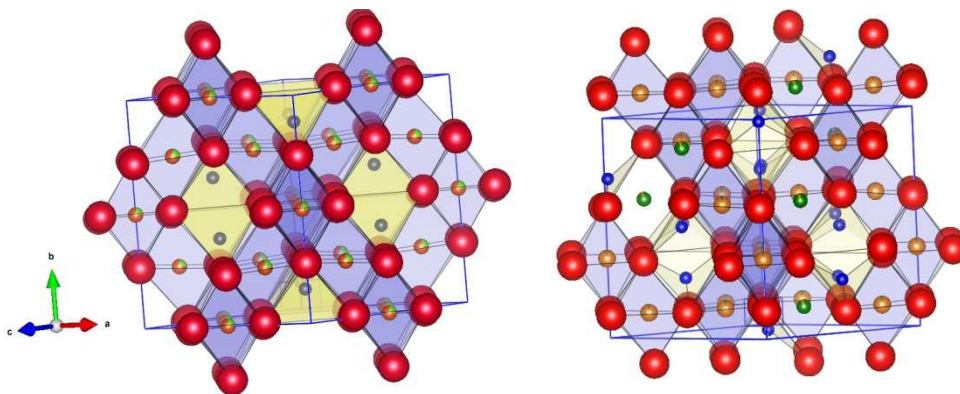


Figure 5.17 Crystal structures of different space groups of LNM (a) $Fd\bar{3}m$ space group (b) $P4_332$ space group, Red spheres – O, Orange spheres – Mn, Green spheres – Ni, blue spheres – Li.

There have been relatively few studies on the phase transformations occurring in the spinel LNM when it is cycled in the 2.3 – 3.3V range and the results have been quite conflicting. Amine et.al [4,5] claimed no transformation from a cubic spinel phase during cycling. They demonstrated this by chemically lithiating spinel LNM to form $\text{Li}_2\text{Ni}_{0.5}\text{Mn}_{1.5}\text{O}_4$ compounds and performing XRD on it. Park et.al [6] claimed that the ordered phase underwent reversible transformation while the disordered phase does not undergo reversible transformation to a tetragonal phase with the help of X-ray and electron diffraction studies. Recently, Manthiram and co-workers [7] had investigated the performance of both ordered and disordered spinel in the voltage range of 2 – 5 V vs. Li/Li^+ . They subjected the spinel LNM synthesized with different degrees of ordering to cycling in different voltage ranges from 2 – 5V and established that there is significant capacity fading for both the ordered and disordered forms when cycled in a wide voltage window (2 - 5V). The only common understanding though seems to be that the space groups seem to affect performance (albeit there remains discrepancies as to which one affects in what way).

With the above discussion in mind, we propose a new mechanism to account for the results obtained here. It is known that Mn^{3+} is a larger ion that is going to cause a distortion of the MnO_6 octahedra. Hence when lithium is inserted, there is going to be a change in the size of the MnO_6 octahedra as the manganese valence would change from +4 to +3. This is going to result in an expansion of the lattice. Now the ordered and disordered phases would have different lattice parameters (owing to the presence of Mn^{3+} in the structure). Hence it would be realistic to expect that these 2 phases would undergo lattice expansion to different extents. Macroscopically, this would lead to the formation of an interface that has stresses associated with it which could possibly inhibit movement of lithium ions. This is very similar to the mechanism proposed by Goodenough and co-workers [8,9] except that there is no phase transformation involved. This would explain why samples with only the disordered phase (LNM_500/LNMSPH_500/electrospun LNM), display good performance as they do not have the second phase which would cause the formation of a stressed interphase during lithium insertion. As the synthesis temperatures increased, it was mentioned that the structures converted from a purely disordered phase to a mixture of ordered and disordered phases. From the FTIR spectra, the amount of disordered phase increases from 600 °C to 800 °C. Similarly, the LNM synthesized via a conventional technique also displays a mixture of phases which would fit into this model and explain the poor observed performance. This would mean that the amount of such ‘stressed’ interphases would increase with increasing temperature of synthesis explaining the observed performances reasonably. This model would also explain why the spinel LNM synthesised at elevated temperatures display excellent cycling stability and capacity when cycled in the 3.5 – 5V range. The reason would be that no Mn^{3+} is formed in the structure as the main redox couple is $\text{Ni}^{2+}/\text{Ni}^{4+}$. Hence again there is no formation of such an interphase that can block the movement of lithium ions.

5.7 Conclusions

In this chapter, the effect of morphology and nano-structuring on electrochemical performance was elucidated. It was found that spherical morphology was beneficial with respect to cycling stability. This is possibly arising out of the ability of a spherical morphology to accommodate stresses better during cycling compared to other morphologies. However the rate performance was still not very good. Furthermore, the effect of particle size on electrochemical performance was eliminated and it was found

that a mixture of 2 different space groups results in a poorer performance. According to this study, spinel LNM with $Fd\bar{3}m$ space group offers better electrochemical performance in the 3V region. Presence of a mixture of $Fd\bar{3}m$ and $P4_332$ space groups resulted in a poor performance. A new model is proposed that can explain the observed differences in performance between various samples in the different voltage ranges. Nano-sizing the spinel to form 1D fibres resulted in an improved electrochemical performance (capacity obtained) in both the 3V and 5V regions. Hence this material was chosen as the base material to demonstrate full cell devices.

References

- [1] M. Kunduraci, G.G. Amatucci, *ECS Transactions*. 3 (2007) 165–170.
- [2] M. Kunduraci, J.. Al-Sharab, G.G. Amatucci, *Chem. Mater.* 18 (2006) 3585–3592.
- [3] L. Zhou, D. Zhao, X. Lou, *Angew. Chem. Int. Ed. Engl.* 51 (2012) 239–41.
- [4] K. Amine, H. Tukamoto, H. Yasuda, Y. Fujita, *J. Power Sources*. 504 (1997) 604–608.
- [5] K. Amine, K. Amine, H. Tukamoto, H. Tukamoto, H. Yasuda, H. Yasuda, et al., *J. Electrochem. Soc.* 143 (1996) 1607–1613.
- [6] S.-H. Park, S.-W. Oh, C.-S. Yoon, S.-T. Myung, Y.-K. Sun, *Electrochem. Solid-State Lett.* 8 (2005) A163.
- [7] E. Lee, K. Nam, E. Hu, A. Manthiram, *Chem. Mater.* 24 (2012) 3610.
- [8] S.-H. Kang, J.B. Goodenough, *J. Electrochem. Soc.* 147 (2000) 3621 – 3627.
- [9] S.H. Kang, J.B. Goodenough, L.K. Rabenberg, *Chem. Mater.* 13 (2001) 1758–1764.

Chapter 6

Demonstration of full cell devices

This chapter will present the results of attempts to employ electrospun spinel LNM (LNM-ES) in full cell devices to demonstrate its feasibility as potential alternative electrode materials for Li^+ ion based energy storage devices. Two potential configurations with LNM-ES as a working electrode will be demonstrated here. One would be a lithium ion battery while the other one would be a hybrid super capacitor.

6.1 Insertion electrode in hybrid supercapacitors

It was evident from the results of galvanostatic cycling performance that LNM-ES exhibited very good rate performance. This would make it ideal for operation in hybrid super capacitors where one of the working electrodes will operate based on intercalation of lithium ions while the other one will operate via a capacitive charge storage mechanism and high rate performance would be a necessary feature. The half-cell performance of the LNM-ES is given in figure 6.1 (a, b). CV traces indicate good reversibility for the $\text{Mn}^{3+}/\text{Mn}^{4+}$ redox couple. One of the important requirements for hybrid super capacitor electrodes is long term cycling stability. To verify if the LNM-ES electrode can offer reasonable capacity retention, the electrode was cycled at 2C rate ($1\text{C} = 150 \text{ mA.g}^{-1}$). It was evident that it could retain about 90 % of the initial capacity after 250 cycles suggesting reasonable cycling stability (figure 6.1b).

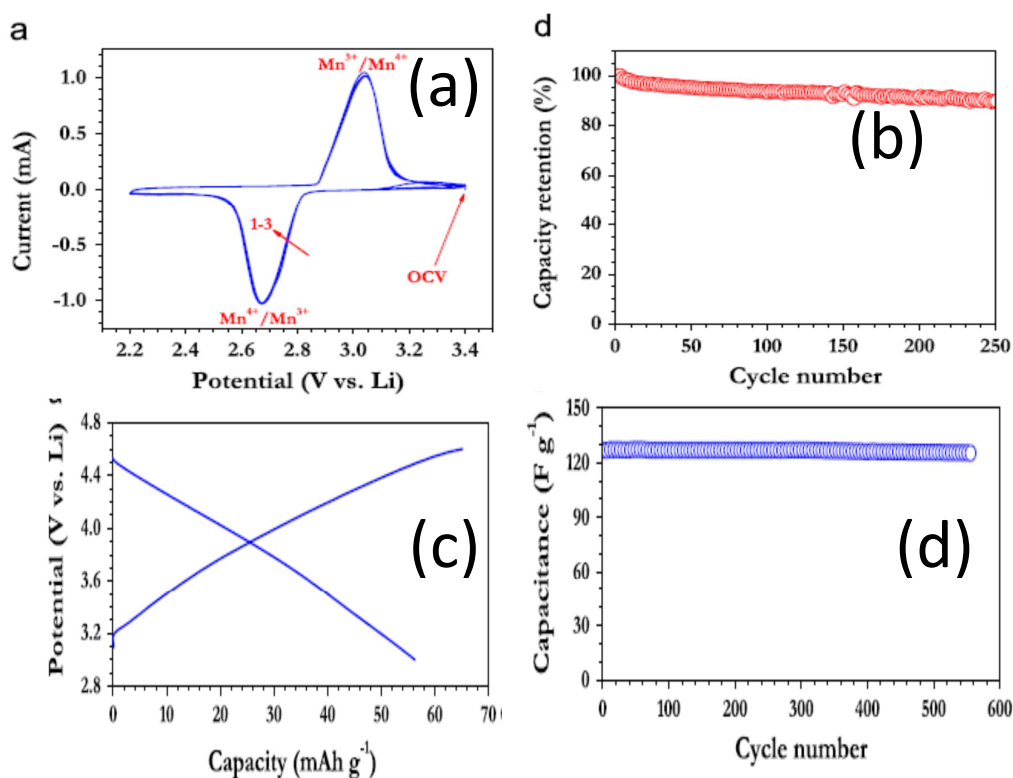


Figure 6.1 Half-cell performances for LNM-ES and AC (a) cyclic voltammogram at 0.1mV.s^{-1} for LNM-ES (b) capacity retention at 2C rate for LNM-ES (c) charge – discharge curve of AC vs Li/Li⁺ at 100 mA.g^{-1} (d) capacity retention at 100 mA.g^{-1} for AC. (Reproduced with permission from Elsevier)

The other working electrode chosen for this device was an activated carbon (AC) fabricated from coconut shell supplied by our collaborator. The reason for choosing activated carbon is obvious. It is known to display extended cycling stability for over 100,000 cycles with almost no fading. The half-cell performance of activated carbon was also studied to decide the optimum mass loading for the full cell configuration. The results are given in figure 6.1(c, d). The AC electrode displayed very good capacity retention with no fading after 500 cycles while displaying a capacity of approximately 56 mAh.g^{-1} . Masses of the electrode materials were calculated from the respective specific capacities obtained during galvanostatic cycling (119 mAh.g^{-1} for LNM-ES and 56 mAh.g^{-1} for AC) thus requiring a ratio of 1:2.125 to LNM-ES and AC.

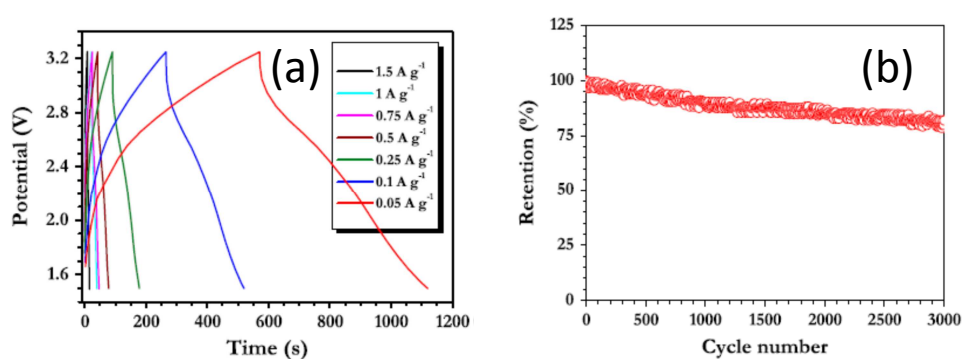


Figure 6.2 Performance of hybrid supercapacitor (a) charge-discharge profiles at different rates (b) Capacity retention at 1 A.g^{-1} rate, 1.5 – 3.25V (Reproduced with permission from Elsevier)

The performance of the LNM-ES/AC hybrid device is given in figure 6.2. The power and energy densities can be calculated using the following formulae, Power = (Voltage x current)/ total mass of electrode, Energy = Power x time. Voltage used will be the average of the maximum and minimum voltages attained during the charge and discharge cycles (1.5 and 3.25 V in this case). About 81 % of the initial capacity is retained at a rate of 1 A.g^{-1} after 3000 cycles. The configuration offers an energy density of approximately 19 Wh. Kg^{-1} at high power densities and this performance was found to be much better than other similar insertion anodes such as TiP_2O_7 and $\text{LiTi}_3(\text{PO}_4)_3$ [1]. This demonstrates the feasibility of employing the LNM-ES as an insertion anode in an organic hybrid supercapacitor device. The hybrid super capacitor based on LNM as the intercalation electrode (anode) represents the first attempt at using the $\text{Mn}^{3+}/\text{Mn}^{4+}$ redox couple as an insertion anode against an activated carbon electrode. The proposed working mechanism is as follows. During charging, lithium

ions from the electrolyte are inserted into the spinel LNM while simultaneously PF_6^- ions adsorb physically on the surface of the activated carbon electrode. Thus charge neutrality is maintained in the electrolyte this way. During discharge, the opposite of this process happens whereby the inserted lithium ions are extracted from the LNM and simultaneously PF_6^- ions are subjected to desorption from the activated carbon surface. This configuration displayed significantly better performance compared to other similar systems based on materials such as $\text{LiTi}_2(\text{PO}_4)_3$ and TiP_2O_7 . However the performance still does not rival the best material which is $\text{Li}_4\text{Ti}_5\text{O}_{12}$ [2]. Still a number of factors make the spinel LNM more attractive compared to a host of other intercalation anodes for hybrid super capacitors. Firstly, the source of lithium in a hybrid electrochemical super capacitor with a carbonaceous electrode is the lithium ions in the electrolyte. Thus materials which consume lithium ions to form SEI/lose lithium ions irreversibly after intercalating are not an ideal choice. For e.g, TiO_2 is susceptible to irreversible capacity loss where in a part of the inserted lithium ions cannot be extracted back from the structure. From this work it is clear that the first cycle efficiency is about 94 % suggesting that the problem of irreversible loss of lithium is not significant. This device is simply a proof of concept device that cannot be really compared with the best existing devices. There are still issues to be addressed including the fading of capacity which arises from the LNM-ES anode mainly. With optimization and further modifications, it should be possible to improve the performance of this system significantly.

6.2 Insertion electrode in lithium ion battery.

In order to demonstrate the potential of nanostructured spinel LNM-ES in a full cell lithium ion configuration employing its performance in the high voltage region, it was decided to form a full cell comprising of fully electrospun components viz. anode, cathode and separator. Such a configuration has already been reported for the native spinel [3]. The most ideal anode material for pairing with LNM would be graphite which allows one to extract the full benefits of the 4.7V offered by LNM. However it is known that graphite would accentuate the problem of electrolyte decomposition significantly [4,5]. Using a nanofibrous carbon would only result in amplifying this effect. When it came to anodes that do not have this problem, there were 2 options namely $\text{Li}_4\text{Ti}_5\text{O}_{12}$ (LTO) and TiO_2 . LTO has already been demonstrated to provide stable cycling capacity in full cell configuration with LNM. It should be noted though

that the operating voltage is not very different (1.5 V) from TiO_2 and it offers lower capacity (163 mAh.g^{-1}). The reported all-electrospun configuration for the lithium ion battery had employed electrospun LiMn_2O_4 , TiO_2 and a separator made of PVdF-HFP co-polymer. All the three components were fabricated via a single spinnerette electrospinning technique. The author's had reported an average voltage of about 2.2 V for the $\text{LiMn}_2\text{O}_4/\text{PVdF-HFP}/\text{TiO}_2$ full cell configuration. They had reported excellent cycling stability for this configuration demonstrating 700 cycles at 1C rate (150 mA.g^{-1}). By replacing the LiMn_2O_4 with $\text{LiNi}_{0.5}\text{Mn}_{1.5}\text{O}_4$, the theoretical operating voltage could be raised to approximately 2.95V which would result in an increase in energy density while maintaining the improved stability during cycling. This was one of the main reasons TiO_2 was employed as an anode in this study. It was already proven to be working in a full cell with LiMn_2O_4 . Hence by replacing only the cathode, it would be possible to obtain a similar cycling stability while improving the energy density.

The TiO_2 and PVdF-HFP were prepared according to the procedures described in [3,6]. The electrochemical performance of the materials was evaluated in a half cell assembly with a PVdF-HFP separator and lithium counter electrode in order to optimize the mass ratio. The data on the half-cell performance is summed up in figure 6.3.

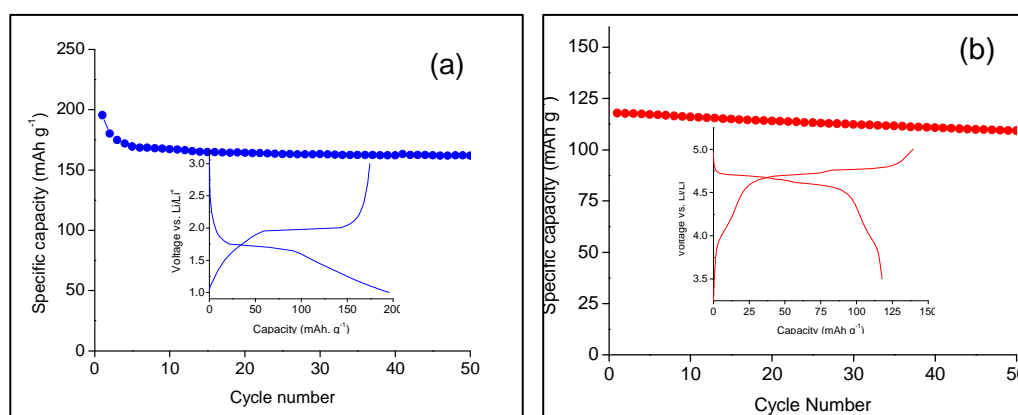


Figure 6.3 Half-cell performance of LNM-ES, TiO_2 (a) $\text{TiO}_2/\text{PVdF-HFP}/\text{Li}$ cell (b) $\text{LiNi}_{0.5}\text{Mn}_{1.5}\text{O}_4/\text{PVdF-HFP}/\text{Li}$ cell. Insets reveal 1st cycle charge-discharge curves for both cells. (Reproduced with the permission of The Royal Society of Chemistry)

The performance in half cell configuration reveals an initial discharge capacity of 195 mAh.g^{-1} for the anatase TiO_2 which stabilizes after 10 cycles to about 164 mAh.g^{-1} .

The retention is about. The LNM-ES sample displayed an initial capacity of 118 mAh.g⁻¹ retaining about 92.3 % after 50 cycles.

Based on the capacities observed in the half cells, the mass of anode employed was fixed to 1.65 times the cathode mass (typically for 5 mg of TiO₂, 8.25 mg of LNM-ES was taken for a full cell assembly). The performance of the full cell assembly is summed up in figure 6.4. The cyclic voltammogram plots (figure 6.4a) give the individual redox potentials of the Ti⁴⁺/Ti³⁺ couple and Ni²⁺/Ni⁴⁺ couple. Based on this, the voltage range for cycling was fixed to 2 to 3.1 V vs. Li/Li⁺. The full cell displayed an anodic potential of 2.96 V. The cathodic potential is slightly lower at 2.69 V. The average cell voltage obtained thus is approximately 2.83 V which is close to the 2.95 V predicted for this configuration.

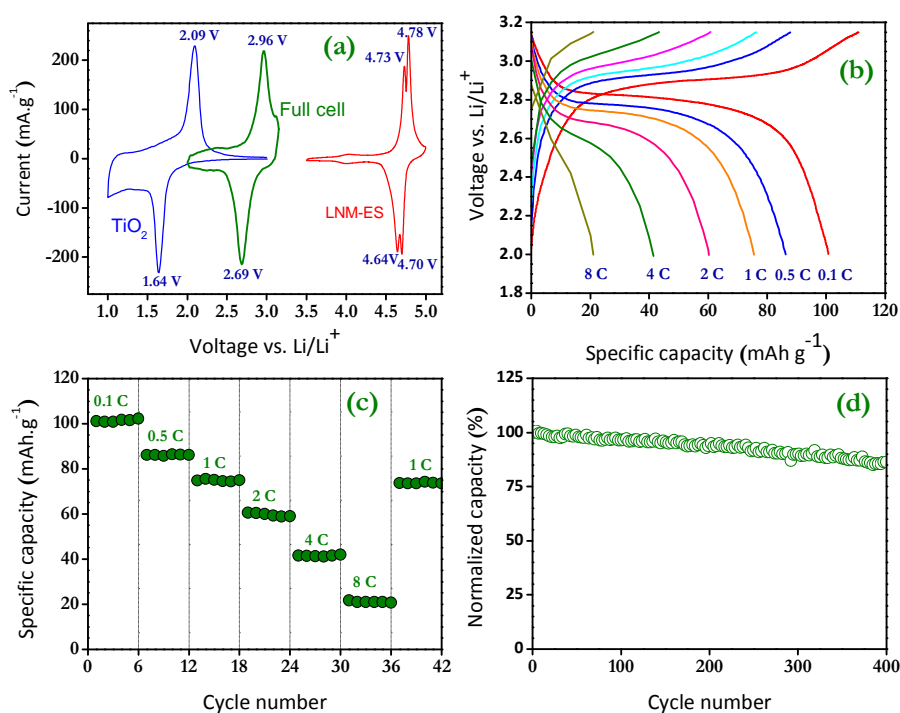


Figure 6.4 Performance of rechargeable battery, LiNi_{0.5}Mn_{1.5}O₄/PVdF-HFP/TiO₂ (a) Cyclic voltammograms showing half cells and full cell assembly (b) charge – discharge curves at different rates (c) rate performance (d) Normalized capacity vs cycle number at 1C rate(Reproduced with permission from The Royal Society of Chemistry).

The configuration presents a capacity of approximately 60 mAh.g⁻¹ based on active mass of the cathode at 2C (300 mA.g⁻¹) rate. However the capacity reduces as the rate increases to 4C and 8C. The capacity increases again on cycling to 1C rate indicating there is no significant structural damage occurring during high rate cycling. The

capacity retention is given in figure 6.4d as a % of initial capacity. 86.3 % of initial capacity is retained after 400 cycles at 1C rate suggesting reasonable cycling stability.

The full cell demonstrates that in spite of the gradual fading observed in the half cell cycling, the LNM-ES material could be successfully employed in a full cell configuration with anatase TiO_2 anode. This is the best known performance reported for this configuration. Brutti et.al. [7] were the first to study a similar configuration and report its performance. They had employed pre-treatments for both the anode and cathode before assembling them into a full cell. The cathode was modified using a ZnO coating while the anode comprising of TiO_2 was pre-treated with lithium to form an SEI. Although they were able to successfully mitigate electrolyte decomposition, they were unable to prevent it completely. Their full cell performance demonstrated retention of 83% after 50 cycles at C/3 cycling rate. In comparison we demonstrate here similar capacity retention over 400 cycles at 1C rate without any modifications to the active material. The much more improved performance could be attributed to the beneficial effect of nanostructuring.

However the best reported full cell performance so far for the spinel LNM is for an LNM-LTO combination in an anode limited design [8]. This cell delivered capacity retention of approximately 98% after 1000 cycles. In comparison, the performance of the configuration reported here is not good. However a few things need to be considered. The performance for the configuration reported in this work is relatively worse because of the significant electrolyte decomposition occurring. On the other hand Wu et.al.had employed solid state synthesised materials where the electrolyte loss per cycle would be significantly lesser. Another important thing to note would be the capacity of the LTO anode (163 mAh.g^{-1}) is roughly about half that of the TiO_2 anode (332 mAh.g^{-1}). Hence with further optimization and suitable electrolyte, the configuration demonstrated here should be able to provide a viable alternative to the LNM-LTO system.

6.3 Conclusions

In conclusion two full cell devices were demonstrated by employing electrospun LNM nanofibers as the working electrode. One of the devices was a hybrid supercapacitor where the $\text{Mn}^{3+}/\text{Mn}^{4+}$ redox couple (activated in the 2.3 – 3.3V range) of the electrospun LNM was employed to store charge. Reasonable performance was

demonstrated for this system although it still cannot compete with established commercial systems as of yet. The second device was a rechargeable lithium battery where the $\text{Ni}^{2+}/\text{Ni}^{4+}$ redox couple was employed to store charge. The cell delivered the best known performance reported for this configuration. However electrolyte decomposition issues prevent realization of the full capacity of this material.

References

- [1] N. Arun, A. Jain, V. Aravindan, S. Jayaraman, W. Chui Ling, M.P. Srinivasan, et al., *Nano Energy*. 12 (2015) 69–75.
- [2] V. Aravindan, J. Gnanaraj, Y.-S. Lee, S. Madhavi, *Chem. Rev.* 114 (2014) 11619 – 11635.
- [3] V. Aravindan, J. Sundaramurthy, P.S. Kumar, N. Shubha, W.C. Ling, S. Ramakrishna, et al., *Nanoscale*. 5 (2013) 10636 – 10645.
- [4] B. Michalak, B.B. Berkes, H. Sommer, T. Bergfeldt, T. Brezesinski, J. Janek, *Anal. Chem.* (2016)
- [5] D. Lu, M. Xu, L. Zhou, A. Garsuch, B.L. Lucht, *J. Electrochem. Soc.* 160 (2013) A3138–A3143.
- [6] X. Zhang, V. Aravindan, P.S. Kumar, H. Liu, J. Sundaramurthy, S. Ramakrishna, et al., *Nanoscale*. 5 (2013) 5973–80.
- [7] S. Brutti, V. Gentili, P. Reale, L. Carbone, S. Panero, *J. Power Sources*. 196 (2011) 9792–9799.
- [8] H.M. Wu, I. Belharouak, H. Deng, a. Abouimrane, Y.-K. Sun, K. Amine, *J. Electrochem. Soc.* 156 (2009) A1047.

Chapter 7

Discussion and future work

This chapter provides the relation between the various studies carried out and evaluates the performance of the devices demonstrated against the targets specified in chapter 1. Possible reasons for poor performance and suggestions for improvements of the systems are made. Issues that need to be considered while attempting scaling up and commercialization are considered. Strategies for future work are also outlined.

7.1 Introduction

This thesis has explored the issue of structural degradation in manganese based oxide materials with a spinel structure and investigated the effect of morphology on performance. First the effect of elemental substitution on electrochemical performance was analysed for 2 spinels in a systematic manner. Nickel substitution in LiMn_2O_4 and titanium substitution in $\text{Li}_4\text{Mn}_5\text{O}_{12}$ were investigated. Hydroxide co-precipitation method was employed to perform these substitutions. It was found that both substitutions resulted in improved capacity retention due to avoidance of structural transformation to detrimental phases when cycled in the voltage range of 2.3 – 3.3V. This was verified by ex-situ XRD analysis of the cycled electrodes. It was determined that spinel LNM samples synthesized at low temperatures (500 °C) displayed the highest capacity and rate performance in the voltage range of 2.3 – 3.3 V while samples synthesized at high temperatures (700 °C/800 °C) displayed the best performance in the voltage range of 3.5 – 5V. While spinel LMO calcined at low temperatures did not undergo conversion to a tetragonal spinel phase, spinel LMO calcined at high temperatures revealed the presence of tetragonal spinel phase after cycling. It was found that nickel substitution prevented phase transformation to a tetragonal phase during cycling in irrespective of the synthesis temperatures. Lithium diffusion studies using cyclic voltammetry measurements indicated decreasing lithium diffusion co-efficients. However this valued determined from CV studies was an apparent value that would change depending on the surface area of the material. It could explain the improved rate performance but not the higher capacity. Impedance analysis revealed lower charge transfer resistance and warburg impedance for samples synthesized at lower temperatures. While the low charge transfer resistance might be a virtue of the surface area, the Warburg impedance is intrinsic to the material. This can hence explain the higher capacities and rate capability for the spinel LNM compared to spinel LMO. Titanium substitution into spinel $\text{Li}_4\text{Mn}_5\text{O}_{12}$ was successfully performed via hydroxide co-precipitation method. Synthesis conditions were optimized at 500 °C for 2 days under O_2 gas flow. All the Ti containing spinels displayed marginally better cycling performance compared to the un-substituted spinel. Ex-situ XRD analysis revealed the suppression of phase transformation to the tetragonal $\text{Li}_{0.89}\text{Mn}_2\text{O}_{3.84}$ phase. Lithium diffusion studies from cyclic voltammetry did not reveal any significant differences between the samples containing different amounts of titanium.

Compared to spinel LNM, Ti substitution in spinel $\text{Li}_4\text{Mn}_5\text{O}_{12}$ proved more difficult to accomplish and lengthy annealing times were required making it a rather unattractive. Hence further studies were focused on optimizing the performance of the spinel LNM and understanding the reasons for the performance obtained.

By varying the morphology and nano-structuring the spinel LNM, the performance was further optimized. The particle size and morphology were fixed at different synthesis temperatures for the spinel LNM. This was possible by using carbonate co-precipitation method which gave spherical particles in the size range of 3- 10 μm . It was observed via SEM analysis that the particle size remains unchanged during firing at different temperatures. Electrochemical performance of these samples was investigated and it was found that the trend of improved performance with lower synthesis temperature in the 2.3 – 3.3V range could be attributed to the differences in the space group of the spinel LNM samples synthesized at different temperatures. Spinel LNM with $Fd\bar{3}m$ space group was found to be amenable to lithium insertion while spinel LNM containing a mixture of $Fd\bar{3}m$ with $P4_332$ space groups was found to be not quite amenable to lithium insertion into vacant octahedral sites. It was also found that spherical morphology offers very good capacity retention for the spinel LNM in both voltage ranges although the rate performance was not very good. By employing electrospinning to generate 1D nanofibers of the spinel LNM, it was demonstrated that spinel LNM with $Fd\bar{3}m$ space group delivered excellent electrochemical performance in both the voltage ranges investigated. Based on the investigations, two full cell devices based on the electrospun spinel LNM were demonstrated. The first device was a lithium ion battery consisting of the electrospun LNM as cathode, electrospun TiO_2 as anode and electrospun PVdF-HFP copolymer as the separator. This device delivered the highest capacity retention (86% after 400 cycles) known for this configuration till date. Accompanying electrolyte decomposition issues were however accentuated by the presence of nanostructured active material. It is hoped that with the development of more stable electrolytes, this system can realize its maximum potential. The second device demonstrated in this work was a lithium ion hybrid super capacitor where the electrospun spinel LNM was employed as an insertion anode. This system also delivered competitive performance rivalling other insertion electrodes such as $\text{LiTi}_2(\text{PO}_4)_3$ and TiP_2O_7 although it still falls short of the best performing hybrid super capacitors.

7.2 Evaluation of performance target achievement

The aim of this work was to demonstrate a full cell device capable of delivering a performance similar to currently available commercial energy storage systems for the grid. As was presented in chapter 1, the currently available commercial grid scale storage system is the sodium-sulphur system. In terms of performance target, the aim was to prepare a device that could demonstrate at least 4000 cycles of charge & discharge while displaying good capacity retention retention (80%) and cycling efficiency (100%). Two devices have been demonstrated in this study but both of them could not meet the design targets specified.

The hybrid super capacitor seems to deliver a reasonable performance of 3000 cycles with almost 100 % cycling efficiency and 81 % capacity retention. In terms of energy density, the hybrid super capacitor delivers around 19 Wh.Kg⁻¹ which would be well short of the value for a sodium-sulphur system [1]. However the power density and cycling efficiency (100%) of the super capacitor would be higher than the sodium sulphur system (the sodium sulphur system uses some the stored energy to keep the system at the required operating temperatures during each cycle). However it should be noted that plenty of other factors could affect the performance of this device such as electrolyte decomposition and manganese dissolution which have not been considered in this work as this was solely focused on structural degradation.

Similarly for the all electrospun rechargeable battery system that was demonstrated, the cycle life (400 cycles) comes nowhere near to that of a sodium-sulphur system. In terms of energy density, the gravimetric energy density is about 285 Wh.Kg⁻¹ based on cathode active mass. This is comparable with the sodium sulphur systems which display similar energy densities. However the biggest obstacle in realizing full potential for this device currently is the electrolyte. Fabricated from a nano-material, it should be apparent that there would be very severe electrolyte decomposition occurring. This electrolyte decomposition reduces the cycling efficiency achievable (92-93%). The remaining 7 – 8% can be considered to be wasted just like the heat used to keep the system at a specified operating temperature for the sodium-sulphur system. Hence unless this can be avoided, this system can never prove to be an attractive option. However research on electrolytes is already progressing towards more promising combinations and it should be possible to overcome this limitation. The second major improvement in this system could be fabrication of anodes that operate

at lower voltages such as graphite for example. Coupling the electrospun LNM in a full cell with graphite would provide a voltage of nearly 4.6V which would increase the energy density by roughly 3 times the current value. This would then make the system very attractive even for applications such as hybrid electric vehicles. But this would require significant advances in understanding electrolyte decomposition behaviour on the anode side for graphite when coupled with an LNM cathode.

7.3 Issues to be addressed for commercialization

The earlier section provided comparisons strictly on a performance basis alone and suggestions for improvements of the performance. However there are other factors that are more important and need to be considered in order to determine if this material can prove to be a viable alternative. The first major issue is that scaling up production of this material in an economical manner. Electrospinning as already discussed in the literature review section is commercially used for producing plenty of tissue replacements. However extending this to the field of battery materials requires significantly more research with respect to scaling up. While it might be possible to scale up the production of precursor fibres, doing so in a cost effective manner would be challenging. It would require establishing a highly reproducible process that can operate round the clock to produce precursor fibres and convert them to oxide materials that could be subsequently be fabricated into electrodes for cell assembly. The key thing would be to ensure strict process control and raw material input quality all of which can affect the quality of the fibres generated.

The second major factor would be the ability to deal with nanomaterials. Handling and control of nanomaterials is usually complicated and associated with various health hazards. Hence the risks need to be evaluated comprehensively before one can think about scaling up the process.

Thirdly, from a view point of cell assembly, it is usually preferred to have as much material loading as possible in a given volume of the cell in order to maximize the energy that can be obtained. In the battery community there is a widespread belief that nanomaterials are not ideal as their packing densities would be low and in turn this would affect the volumetric energy density ultimately making them unattractive. In this work however, it is demonstrated on a cell level that it is possible to obtain a mass loading that is similar to or better than industrially accepted levels. Hence the notion that nanomaterials provide lower volumetric energy densities might not be a

significant impediment to commercialization provided a viable method to scale up this mass loading can be established.

7.4 Future work

Although in reality these two devices are yet to match the performance of the commercially available systems for grid scale energy storage, this work presents an insight into harnessing the 3V region of the spinel oxide for storing energy with reasonable performances which need improvement. This work hence serves to reignite interest in exploring cheaper options for energy storage. A number of questions can be posed which would provide interesting scope for further research. They are summed up in the sections below.

7.4.1 Quantification of manganese dissolution for spinel LNM.

Capacity fading due to structural degradation was addressed mainly in this work. However there are other mechanisms for capacity fading which are also active simultaneously. In spite of delivering reasonable performance, the electrospun LNM displayed fading especially in the 2.3 – 3.3 V range. Manganese dissolution would be a major capacity fading mechanism and the effect would be accentuated by the presence of nanostructures. It would be interesting to quantify the manganese dissolution that is occurring in this material when it is used in the voltage range of 2.3 – 3.3V. ICP-OES analysis would be a very effective technique to monitor the manganese content in electrolytes. Soaking tests at various temperatures could help determine the manganese dissolved from the active material through simple chemical attack of active material. Similarly coin/pouch cells could be employed to determine the amount of manganese dissolution occurring due to electrochemical attack of the active material by the electrolyte. It is important to quantify manganese dissolution as it is one of the greatest challenges confronting manganese based oxide materials currently.

7.4.2 Surface modification with carbon/lithium ion conducting metal oxide coatings.

Along with efforts to quantify manganese dissolution, approaches to tackle it are also necessary. Carbon coatings and or metal oxide coatings (such as $\text{Li}_2\text{B}_4\text{O}_7$) could be considered for this purpose. The use of electrospinning method can actually facilitate the formation of these coatings on the active material using the co-axial spinning

method wherein precursors for the coatings can be deposited in the form of a shell covering the polymeric fibres. In one step, an active material fibre consisting of a protective shell of carbon could be synthesized. It would also be interesting to study the effect of such coatings on lithium ion diffusivity and rate performance.

7.4.3 Elevated temperature studies of electrochemical performance

It is essential to understand how temperature affects the cell performance for the systems demonstrated in this work. It is known that temperature can in general accelerate degradation processes such as dissolution and electrolyte decomposition. The presence of a nanostructure would only compound the issue. Hence it would be essential to know the performance of the systems demonstrated in this work at elevated temperatures and identify the reasons for the same. This would enable a more realistic assessment of performance for the demonstrated devices.

7.4.4 Understanding structural changes using in-situ techniques

As was evident from the results presented in this work, the spinel LNM calcined at high temperatures displays poor performance in the voltage range of 2.3 – 3.3V (but excellent performance in the 3.5 – 5V). More work is needed to understand why this is happening. It would be interesting to verify if the interphase theory postulated by Goodenough can explain the results observed here. Are there changes that occur only at the surface but somehow end up completely stopping further insertion of lithium into the structure? For example analysing cycled electrodes with XPS combined with FIB can also help in understanding if the lithium insertion is limited to the surface alone. In-situ raman spectroscopy can help identify if the mixture of space groups undergoes any transition during cycling.

7.5 Scientific contributions.

- Deeper understanding of the spinel LMO and LNM systems via a more systematic study revealing hitherto unreported behaviour and the reasons for such a behaviour.
- A novel method to isolate and eliminate the effect of particle size on electrochemical performance while analysing the effect of other factors.
- Proposing a new mechanism to explain the effect of space group on the electrochemical performance of the spinel in the 2.3 – 3.3V range.

- Investigation of the effect of nanostructuring of spinel LNM with an $Fd\bar{3}m$ space group on electrochemical performance.

7.6 Technological contributions

1D nanofibers of high voltage spinel LNM synthesised via a single spinnerete electrospinning method were demonstrated as

- Suitable cathode materials in a full cell lithium ion battery together with electrospun TiO_2 and electrospun separators made of PVdF-HFP co-polymer.
- Insertion anode in a full cell lithium ion hybrid super capacitor

References

- [1] K.C. Divya, J. Østergaard, *Electr. Power Syst. Res.* **2009**, 79, 511–520.